

UNIVERSITÀ DEGLI STUDI DI NAPOLI

“FEDERICO II”



DIPARTIMENTO DI INGEGNERIA CHIMICA, DEI MATERIALI E
DELLA PRODUZIONE INDUSTRIALE

DOTTORATO IN
INGEGNERIA DEI PRODOTTI E DEI PROCESSI INDUSTRIALI
XXXIII CICLO

DEVELOPMENT OF ELASTOMERIC COMPOSITE MATERIALS
FOR THE REALIZATION OF PIEZORESISTIVE SENSORS

TUTOR

Prof.ssa Veronica Ambrogi

CANDIDATO

Dott. Gennaro Rollo

CO-TUTOR

Dott. Pierfrancesco Cerruti

Dott. Marino Lavorgna

A.A. 2020/2021

Index

Abstract.....	3
Abstract.....	6
Chapter 1 Fundamentals on piezoresistive materials and 3D printing technology	9
1.1. Piezoresistivity.....	9
1.2. Piezoresistive materials applications.....	16
1.2.1. Strain gauges.....	16
1.2.2. Force or pressure sensors.....	17
1.3. Piezoresistive composite materials	20
1.4. 3D printing.....	28
1.4.1. Selective laser sintering (SLS)	30
1.5. Aim of the PhD project.....	31
References	32
Chapter 2 Selective laser sintering fabricated thermoplastic polyurethane/graphene high strain sensitivity	46
2.1. Introduction.....	47
2.2. Materials and methods	49
2.2.1. Preparation of TPU/GE nanocomposites powder.....	49
2.2.2. Porous structures design by TMPS.....	50
2.2.3. Nanocomposite porous structure realization by SLS	51
2.2.4. Scanning electron microscopy (SEM).....	51
2.2.5. Transmission electron microscopy (TEM).....	52
2.2.6. Thermal properties.....	52
2.2.7. Raman spectra analysis.....	52
2.2.8. Mechanical and piezoresistive measurements	52
2.2.9. Thermal conductivity measurement	53
2.3. Results and Discussion.....	53
2.3.1. Design and realization of the TPU/GE porous structures.....	53
2.3.2. Chemical-physical and morphological characterization of the SLS manufactured foams	55
2.3.2.1. Thermal properties	58

2.3.3.	Mechanical and piezoresistive characterization	59
2.3.4.	Thermal conductivity	64
2.4.	Conclusions.....	65
References	68	
Chapter 3 On the Synergistic Effect of Multi-Walled Carbon Nanotubes and Graphene Nanoplatelets to SLS 3D-Printed Elastomeric Structures	74	
3.1. Introduction.....	75	
3.2. Materials and Methods.....	78	
3.2.1.	Preparation of Nanocomposites Powder.....	78
3.2.2.	Porous Structures Design and Manufacturing by SLS Technology	79
3.2.3.	Electron Microscopy.....	81
3.2.4.	Thermal Characterization	81
3.2.5.	Piezoresistive Measurements.....	82
3.2.6.	Electromagnetic Shielding.....	82
3.2.6.1.	Low-Frequency Range	82
3.2.6.2.	Microwave Range	82
3.2.6.3.	THz Range.....	83
3.3. Results and Discussion.....	83	
3.3.1.	Morphological Characterization of the Porous Structures	83
3.3.2.	Thermal Properties	84
3.3.3.	Mechanical and Piezoresistive Characterization	86
3.3.4.	EM Characterization.....	94
3.4. Conclusions.....	97	
References	99	
Conclusions and future perspectives	107	
Papers, conference contributions, participations to formation and dissemination events, and research periods abroad	111	

Abstract

I materiali piezoresistivi, in grado di rilevare la deformazione geometrica attraverso variazioni della resistenza elettrica, hanno suscitato negli ultimi quarant'anni un interesse crescente in ambito scientifico e industriale, soprattutto con l'avvento dei materiali conduttivi nanostrutturati a base di carbonio. Questi filler leggeri, altamente conduttivi e di facile ottenimento hanno ampliato lo spettro dei materiali fino a quel momento utilizzati, aprendo la possibilità di un maggiore sviluppo di materiali multifunzionali. In particolare, le cariche carboniose, omogeneamente disperse all'interno di una matrice polimerica, hanno rappresentato da subito una valida alternativa ai metalli utilizzati nel campo dei sistemi piezoresistivi. Nell'ambito dei nanocompositi polimerici e dei materiali piezoresistivi, una sfida significativa per la comunità scientifica è rappresentata dal raggiungimento di un efficace percorso di percolazione che consenta il passaggio di una corrente elettrica alla minima percentuale di filler (soglia di percolazione), importante per correlare l'applicazione di forze esterne alle variazioni di resistenza elettrica. In generale, i materiali piezoresistivi, per lo più compositi a base polimerica, vengono progettati disperdendo in modo omogeneo il filler carbonioso nella matrice polimerica. Tuttavia, è ben noto che un semplice approccio per ridurre il contenuto di filler e realizzare un composito conduttivo può essere ottenuto sfruttando la segregazione del filler nella matrice polimerica: quando la carica non è dispersa in modo casuale, ma segregata all'interno della matrice per formare una rete tridimensionale, la conducibilità elettrica può essere ottenuta con un contenuto significativamente inferiore della carica carboniosa.

Tra le varie tecniche per la realizzazione di sistemi piezoresistivi, nell'ultimo decennio le tecnologie di Additive Manufacturing, o 3D printing, hanno suscitato il maggior interesse. I processi di stampa 3D portano ad una notevole riduzione di costi e tempi rispetto alle tradizionali tecnologie di lavorazione della fase polimerica. Inoltre, per quanto riguarda la prototipazione, consentono una pressoché totale libertà di creare forme e geometrie anche complesse in modo

automatizzato e assolutamente riproducibile. In particolare, la Selective Laser Sintering (SLS) è una delle tecnologie più interessanti, in grado di permettere di costruire agevolmente la rete segregata di filler, partendo da polvere polimerica adeguatamente preparata. La tecnologia sfrutta la sinterizzazione di particelle polimeriche mediante laser nella classica modalità layer-by-layer. Sono molti i polimeri che possono essere utilizzati, dagli elastomeri ai termoindurenti, oltre ai filler conduttivi.

In questo progetto di dottorato di ricerca è stata studiata la possibilità di ottenere materiali piezoresistivi stampati con 3D SLS utilizzando poliuretano termoplastico (TPU) come matrice polimerica e nanoparticelle di grafene (GE) e nanotubi di carbonio multi walled (MWCNT) come filler conduttivo. L'obiettivo principale della ricerca di dottorato è stato quello di indagare le potenzialità del SLS per creare materiali conduttivi porosi con distribuzione segregata del filler conduttivo, valutando l'effetto di diverse geometrie e porosità (dal 20% all'80%) e diversa forma del filler conduttivo (cioè filler 1D e filler 2D). Anche in questo caso lo scopo è stato quello di valutare, sulla base della completa caratterizzazione dei materiali, qual è l'effetto della tecnologia utilizzata, trovando una possibile correlazione con le geometrie stampate. Pertanto, nella prima fase del progetto, sono stati stampati sistemi porosi utilizzando TPU modificato con l'1% in peso di GE e partendo dalle geometrie Diamond (D), Gyroid (G) e Schwarz (S) per la costruzione della porosità regolare. Le strutture porose tridimensionali risultanti hanno mostrato un'efficace rete conduttiva dovuta alla segregazione delle nanoparticelle di grafene precedentemente assemblate sulla superficie della polvere di TPU tra le particelle elastomeriche sinterizzate. I risultati confermano che la presenza di GE migliora la stabilità termica della matrice TPU, aumentando anche la sua temperatura di transizione vetrosa. Inoltre, le strutture porose realizzate con la geometria S hanno mostrato valori di modulo elastico più elevati rispetto alle strutture basate su D e G. Dopo i test di compressione ciclica, tutte le strutture porose hanno evidenziato un robusto comportamento piezoresistivo negativo, indipendentemente dalla loro

porosità e geometria, con un'eccezionale sensibilità alla deformazione. Valori di Gauge Factor (GF) di -12,4 all'8% di deformazione sono stati ottenuti per strutture S con porosità del 40 e 60%, mentre valori di GF fino a -60 si ottengono per deformazioni inferiori al 5%. La conducibilità termica delle strutture TPU/GE diminuisce significativamente con l'aumentare della porosità, mentre l'effetto dell'architettura della struttura è meno rilevante.

La seconda parte del progetto si è concentrata sulla caratterizzazione di prodotti TPU stampati in 3D con MWCNT e una miscela dei due filler, sempre all'1% in peso sul totale, ma con una proporzione di 70/30 MWCNT/GE, incorporati in sistemi porosi con geometrie D e G, in al fine di indagare un possibile effetto sinergico delle due cariche conduttive. I risultati hanno mostrato che le strutture porose a base di TPU con 1wt% di MWCNT/GE mostrano eccellente conduttività elettrica e resistenza meccanica. In particolare, tutte le strutture porose mostrano un robusto comportamento piezoresistivo negativo, come dimostrano i valori di GF che raggiungono valori di circa -13 all'8% di deformazione. Inoltre, le strutture porose G20 (porosità del 20%) mostrano coefficienti di assorbimento alle microonde che vanno da 0,70 a 0,91 nella regione 12-18 GHz e vicini a 1 per frequenze nella regione dei THz (300 GHz - 1 THz). I risultati mostrano che la presenza simultanea di MWCNT e GE porta un miglioramento significativo nelle proprietà funzionali specifiche delle strutture porose, che vengono proposte come potenziali attuatori piezoresistivi con rilevanti proprietà di schermatura delle interferenze elettromagnetiche (EMI).

Abstract

Piezoresistive materials, able to sense geometrical deformation through variations of the electrical resistance, attracted an increasing interest in the scientific and industrial compartments during the last forty years, which increased significantly with the advent of nanostructured carbon-based conductive materials. These light, highly conductive and easy-to-obtain fillers have broadened the spectrum of materials that had been used up to that time, opening up the possibility of greater development of multifunctional materials. In particular, the carbonaceous fillers, homogeneously dispersed within a polymer matrix, immediately represented a valid alternative to the metals used in the field of piezoresistive systems. In the context of polymer nanocomposites and piezoresistive materials, a significant challenge for the scientific community is represented by the achievement of an effective percolation pathway, which allows the passage of an electric current at the lowest percentage of filler (percolation threshold), and provides a direct correlation of the external forces with the electrical resistance variations. Generally, the piezoresistive materials based on the exploitation of the polymer-based composites are designed by homogeneously dispersing the carbonaceous filler in the polymeric matrix. However, it is well known that a simple approach to reduce the content of filler and realize a conductive composite can be obtained by exploiting the concept of segregation of filler in the polymeric matrix. When the filler is not randomly dispersed, but segregated to build up a three-dimensional network, the electrical conductivity can be obtained with a significantly lower content of the carbonaceous filler.

Amongst the several techniques for the realization of piezoresistive systems, in the last decade, the Additive Manufacturing (3D printing) technologies have aroused the greatest interest. The 3D printing processes lead to a considerable reduction in costs and times as compared with the traditional technologies of processing of polymers. Furthermore, as regards prototyping, they allow an

almost total freedom to create even complex shapes and geometries in an automated and effective way. In particular, Selective Laser Sintering (SLS) is one of the most interesting technology, able to build up easily the segregated filler network, starting from polymeric powder adequately prepared. It is focused on the sintering of polymeric particles by a laser in the classic layer-by-layer mode. Many polymers can be used, from elastomeric to thermosetting, as well as conductive fillers.

In this PhD research project, it was investigated the possibility of obtaining piezoresistive materials printed with 3D SLS using thermoplastic polyurethane (TPU) as a polymer matrix and graphene nanoparticles (GE) and multiwalled carbon nanotubes (MWCNTs) as conductive filler. The main objective of the doctoral research was to investigate the potential of SLS to create porous conductive materials with segregated distribution of the conductive filler, by evaluating the effect of different geometries and porosities (from 20% to 80%) and different shape of the conductive filler (i.e. 1D filler and 2D filler). Again, the aim was to evaluate, based on the complete characterization of the materials, what is the effect of the technology used, finding a possible correlation with the printed geometries. Thus, in the first part of the project, porous systems were printed using TPU modified with 1wt% of GE and starting from Diamond (D), Gyroid (G) and Schwarz (S) geometries for the building up of systems with regular porosity. The resulting three-dimensional porous structures show an effective conductive network due to the segregation of the graphene nanoplatelets previously assembled on the TPU powder surface in between the sintered elastomeric particles. The results confirm that GE nanoplatelets improve the thermal stability of the TPU matrix, while also increasing its glass transition temperature. Furthermore, porous structures made from S geometry show higher elastic modulus values in comparison with D and G based structures. After cyclic compression tests, all porous structures show robust negative piezoresistive behavior, regardless of their porosity and geometry, with exceptional sensitivity to deformation. Gauge Factor (GF) values of 12.4 at 8% deformation are obtained

for S structures with 40 and 60% porosity, while GF values up to 60 are obtained for deformations lower than 5%. The thermal conductivity of TPU/GE structures significantly decreases with increasing porosity, while the effect of the structure architecture is less relevant.

The second part of the project focused on the characterization of 3D printed TPU products with MWCNTs and a mixture of the two fillers, again at 1wt% but with a proportion of 70/30 wt/wt MWCNTs/GE with geometries D and G, in order to investigate a possible synergistic effect of the two conductive fillers. The results showed that the porous structures based on TPU with 1wt% MWCNTs/GE exhibit excellent electrical conductivity and mechanical strength. In particular, all the porous structures show a robust negative piezoresistive behavior, as demonstrated by the GF values that reach values of about -13 at 8% deformation. Moreover, the G20 porous structures (20% porosity) show microwave absorption coefficients ranging from 0.70 to 0.91 in the 12-18 GHz region and close 1 in the THz (300 GHz - 1 THz) frequency region. The results show that the simultaneous presence of MWCNT and GE brings a significant improvement in the specific functional properties of porous structures, which are proposed as potential piezoresistive actuators with relevant electromagnetic interference (EMI) shielding properties.

Chapter 1 | Fundamentals on piezoresistive materials and 3D printing technology

Introduction

1.1. Piezoresistivity

The term *piezoresistive* includes two words of different linguistic origin: “piezo”, from the Greek “piezein” (πιεζω, infinitive πιεζεῖν) which means «to press, to compress», and “resistive” (resistere) which means, «to stop», from Latin. The effect consists in a change of electrical resistance R of an electric conductor according to the following equation:

$$R = \frac{\rho \cdot l}{A} \quad (1.1)$$

where ρ is the material resistivity [$\Omega \cdot cm$], l the conductor length, and A the transverse section area, because of a change in its geometrical parameters originated by an external stimulus.

Historically, the piezoresistive effect was observed for first time by Lord Kelvin (Sir William Thomson, Belfast, 1824–1907) around the 1856 [1], but only one hundred years after, at end of the World War II, a device was used for robotics tactile sensors (Figure 1.1) [2].

It’s important to clarify the definition of piezoelectricity, also. In fact, Piezoelectricity, also called the piezoelectric effect, is the ability of certain materials to generate an AC (alternating current) voltage when subjected to mechanical stress or vibration, or to vibrate when subjected to an AC voltage, or both. The most common piezoelectric material is quartz. Certain ceramics, Rochelle salts, and various polymers also exhibit this effect[3]. An important clarification is needed to distinguish the difference between piezoelectric and piezoresistive materials: the first ones spontaneously generate an electric

potential difference when subjected to a mechanical force, while the second ones need an external voltage to be supplied, and are not inherently able to generate an electric signal when strained or compressed. When a voltage is applied to the ends of a conductive bar, the current also changes according to the Ohm's law states, and it is possible to correlate it with the geometry change, which occurs due to a deformation consequent to the exerted forces [4]. Piezoelectric materials are defined as “active sensors” because they spontaneously generate an electric signal when stimulated; a “passive sensor”, contrarily, needs specific supply circuits depending on the technology of the transducer [5].

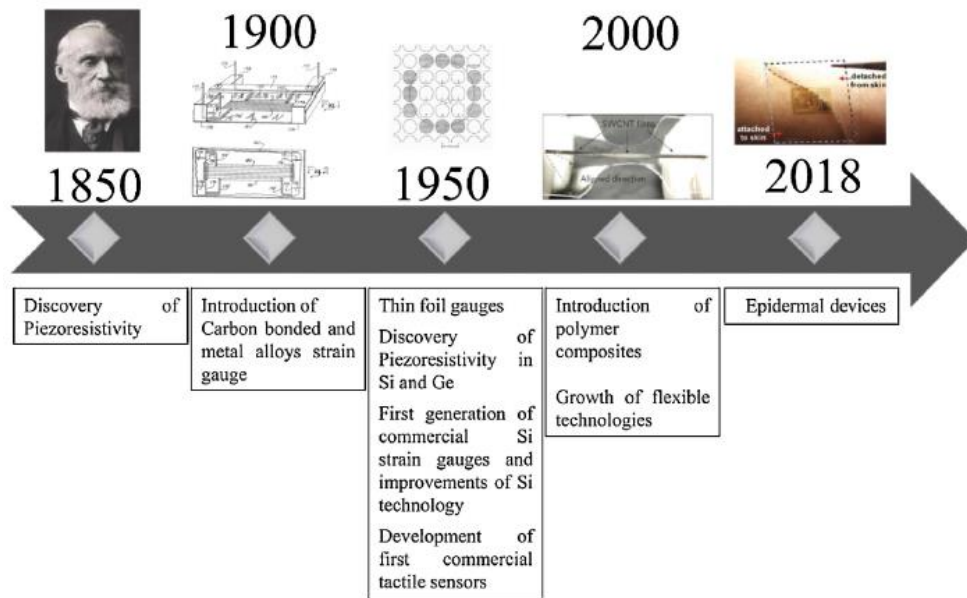


Figure 1.1. Timeline of the piezoresistive sensor technology development[6].

Initially, studies on piezoresistive materials were focused on semiconductors [7], but in the last twenty years composite systems, made of conducting particles dispersed in an insulating matrix, are increasingly being investigated [8]. Starting from 1956 (see the trend in Figure 1.2) the scientific interest in term of number of scientific publications involving piezoresistivity dramatically increased.

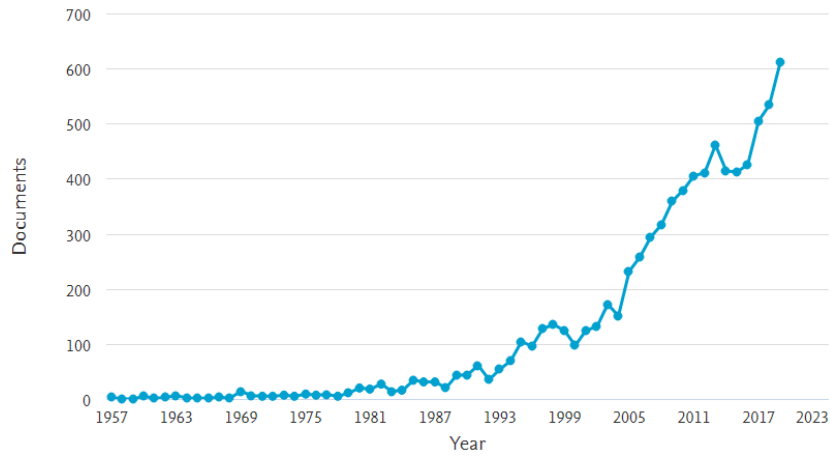


Figure 1.2. Trend of the papers retrieved using the keyword "piezoresistive" from 1957 to 2020 (source Scopus).

The research areas in which piezoresistive materials are investigated are numerous and diversified; Figure 1.3 shows the areas with the greatest impact in terms of scientific publications.

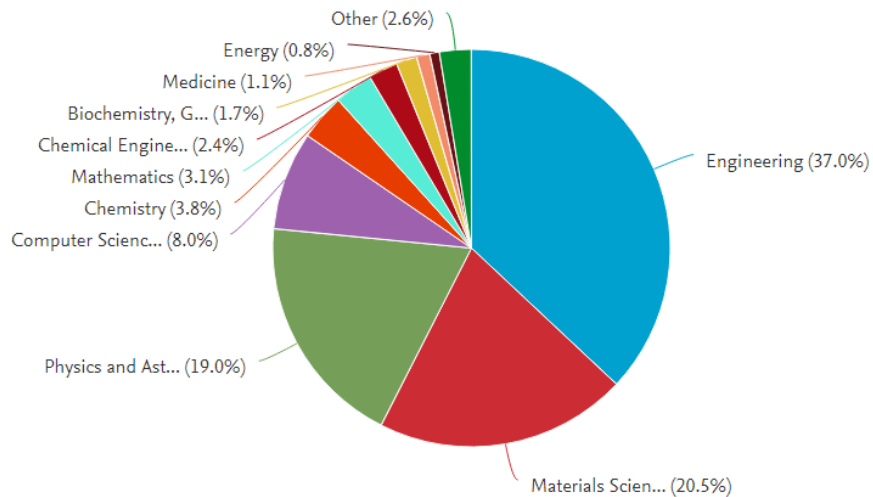


Figure 1.3. Main research areas in which piezoresistive materials are applied (from Scopus).

The reasons for such large research efforts can be found in the recent use of insulating polymeric matrices, which have made it possible to overcome the limits in terms of mechanical properties of the early piezoresistive materials[9]. Piezoresistors can also be fabricated using metals, which are mostly employed in the fabrication of strain gauges, exploiting the resistance variation induced by small changes in the geometry of the sensor. Some metals, such as platinum and nickel, present a higher resistivity variation with respect to the resistance change induced by geometrical change. However, the major drawbacks of these semiconducting and metallic piezoresistors are their fragility and rigidity, in addition with the temperature sensitivity and high cost. These disadvantages can be partly overcome by embedding the piezoresistors in flexible polymers [10], [11]. On the other hand, conductive system made of polymers and incorporated particles (i.e. fillers) led to a tool employed for the description of electric conduction in polymer composites (i.e. polymers and dispersed conductive particles) called the *percolation theory*. The objective of percolation theory is to define how a set of randomly positioned sites can be interconnected to each other. To clarify this theory, let's consider a low-concentration filler isolated and dispersed within the matrix (Figure 1.4a). Being the matrix insulating, the system results in a high electric resistance. By gradually increasing the concentration of the filler, a conductive path is established, and thus a drastic reduction in electric resistance comes about, being this point defined as “percolation threshold” (PH) [12] (Figure 1.4b).

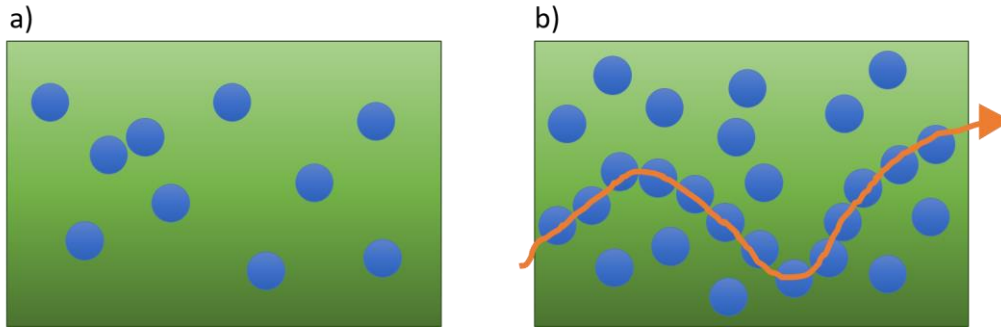


Figure 1.4. a) Conductive particles dispersed in an insulating matrix. b) The electrical conduction path at the percolation threshold.

The conductivity of an insulating mixture above the percolation threshold can be expressed by using the equation:

$$\sigma = \sigma_0 (X - X_C)^B \quad (1.2)$$

where X is the volume fraction of the filler, X_C is the volume fraction of the filler when the percolation threshold is reached, and B is the power of the conductivity increase after reaching the threshold, with the latter that is dependent on the properties of the filler (e.g. geometry) [13]. The class and shape of the filler can affect the conduction mechanism inside the composite: percolation or quantum tunneling (the phenomenon where a wavefunction can propagate through a potential barrier), or also a combination of both, and the applied load could cause a decrease or an increase of the conductivity. Indeed, when there is no physical contact but the distance between the conductive particles is 10 nm or less, the tunneling conduction mechanism occurs [14].

Starting from 1966, when Gurland [15] observed for first time experimentally the dependence of conductivity on the surface area or the conducting area, many theoretical approaches and processing techniques were proposed. To achieve the required properties, conductive fillers in an insulating matrix generally should exhibit homogeneously random dispersion or orderly

oriented dispersion [16], in order to increase the possibilities of filler alignment inside the matrix. After many trials, according to the mechanism of alignment, these methods can be divided into three categories:

1. *Self-alignment*: filler alignment is achieved by solution casting, resulting from their large size and the low viscosity of the mixture system. Moreover, the interfacial bond between polymer matrix and conductive filler is also an important factor to affect the formation of aligned composites [17].

Vacuum-assisted self-assembly is an efficient technique to form dense composites with filler-aligned in layer. Fillers are dispersed in the polymer solution, and then the mixed solution is subjected to a vacuum filtration system. Finally, the aligned fillers structure is formed after the solution filtration parallel to the filter surface [18].

Layer-by-layer assembly is a chemical technique to align filler into the polymer matrix. In general, functional groups of the filler surface can combine with oppositely charged materials, that is adjacent fillers or polymer, with wash steps in between, resulting in a layer-network in the matrix[19].

2. *Electric/magnetic field aided alignment*: Electric and magnetic field aided alignments are effective methods. The applied external electric and magnetic field can realign micro and nano particles along the direction of the field, resulting in a pearl-chain-like aggregate. As an example, filler electric sensitive particles, like graphene, are simply oriented using an external electric field. Also magnetic orientation is an attractive choice, but in this case magnetic functional modification for the filler is necessary, which can greatly enhance the magnetic susceptibility. Generally, integration of graphite nanoplatelets (GNP) with magnetic particles, for example, Iron Oxide (Fe_3O_4), is a popular way to form magnetic hybrids [20].

3. *Mechanical stress aided alignment*: In this way, the filler particles are forced to align in the polymer by the mechanical stress generated in the sample preparation process. This stress generally includes pressure stress (usually thermal compression process [21]), shear stress (realized by injection and extrusion, including the spinning and melt extrusion technologies [22]), and tensile stress, that can induce the orientation of molecular chains along the stretching direction [23].

Recently 3D printing, in particular Selective Laser Sintering (SLS), has been regarded as an efficient method to obtain the alignment of the filler, thanks to the sintering between powder polymeric particles that induce segregation of the conductive materials between the particles of the insulating matrix [24].

The change in resistance can occur due to a tensile or compressive strain. The effect called *negative pressure coefficient of resistance* (NPCR) consists in a general decrease of the electrical resistance, occurring with low aspect ratio particles, such as metal powders and carbon black [25]. In contrast, the *positive pressure coefficient of resistance* (PPCR) effect occurs when the resistance increases with the compressive strain, mainly with high aspect ratio particles, i.e., carbon nanotubes (CNTs), graphite nanosheets and high structure carbon black agglomerates [14-15]. A similar process could take place under the application of a compressive force: without any load, the particles are distant enough to guarantee an insulating behaviour, while when the composite is deformed, the particles come closer, touching each other, thus creating conductive paths that decrease the electrical resistance of the sample [28]. The behaviour of these latter materials is described by the percolation theory, where the insulator-conductor transition suddenly occurs in correspondence of a small variation of the conductive filler fraction defined as percolation threshold (PH) [29].

The piezoresistivity of a material is defined as the dependence of electrical resistivity on strain, and is quantified by the Gauge Factor (GF) [30].

$$GF = \frac{\Delta R/R_0}{\varepsilon} \quad (1.3)$$

where $\Delta R = R - R_0$, and R_0 and R are the resistances at zero strain and at strain ε , respectively.

The main applications of the piezoresistivity principle will be shown below in the next paragraph.

1.2. Piezoresistive materials applications

1.2.1. Strain gauges

A strain gauge transforms uniaxial mechanical strain (deformation, indicated with ε) into a change of its electric resistance (Figure 1.5). It allows the (indirect) measurement of non-electrical quantities such as deformation, bending, force, acceleration, etc. Strain gauges are widely used for the measurement of force, strain, and torque in components that undergo mechanical stress. Different polymeric matrix for strain gauges (indicated in the following) are used in various fields of application as, for example, in structural health monitoring, electrical measurement and finger-mounted devices [31].

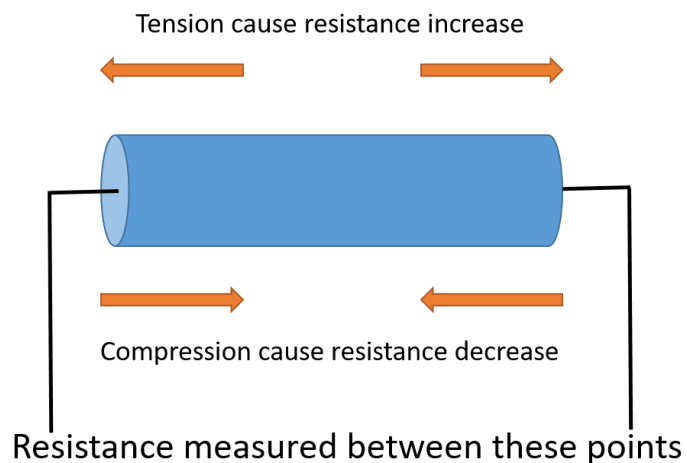


Figure 1.5. Strain gauges with resistance variation working principles.

1.2.2. Force or pressure sensors

According to Newton's second law, under the application of a force $F = m dv/dt$, a body of mass m moves with an acceleration dv/dt . Forces change the quiescent or motile state of a body to which they are applied. This simple concept finds application in the development and sensorization of humanoids, motor control, microelectronic packaging, touch panel and other [32]. For the measurement of the physical forces that make contact with an object, the contact sensors are of fundamental importance. Recently, most of the commercial sensors dedicated to human touch mimesis are implemented with Force Sensing Resistors (FSR), which are unusually employed in high-accuracy applications [33]. The FSR are cheaper than capacitive and piezoelectric sensors, and are very thin. Typically, a FSR is a polymer thick film (PTF) device that exhibits a decrease in resistance with an increase in the force applied to the active surface [34]. A schematic representation of a typical FSR sensor is shown in Figure 1.6.

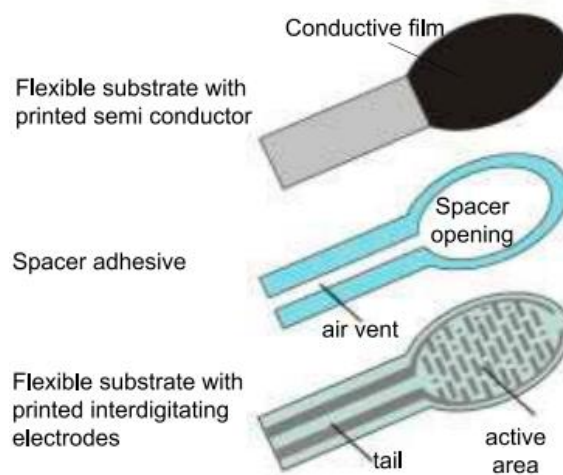


Figure 1.6. FSR construction [35].

In most of the integrated piezoresistive sensors, the force is applied at the end or in the central region, deflects the beam and induces a compression or an expansion of the gauges depending on the beam geometry and constraints. The

major weakness of the classic (semiconductor and metallic) force sensors are the mechanical fragility and scarce thermal stability[36]. In order to overcome these disadvantages, the use of flexible substrates has been investigated. Two strategies are adopted: integration of rigid transducers inside the matrix, and/or inclusion of the microparticles in order to decrease the stiffness of the sensors. Usually, in the first case, the integration is achieved using silicon, in which an intermediate oxide layer is used to stop the etching of the bulk Si substrate; in the second case, the silicon is etched away as far as the intermediate oxide stop layer, to form the cantilever [37].

Strain gauges for pressure measurements convert pressure variations (force per unit area) into resistance variations. Semiconductor strain gauges are also used for measurements of the order of a few hundred $kg\ m^{-2}$. The transducers are usually located on the opposite side to where the pressure is applied [38]. In Figure 1.7 are reported schematically the three common transduction methods.

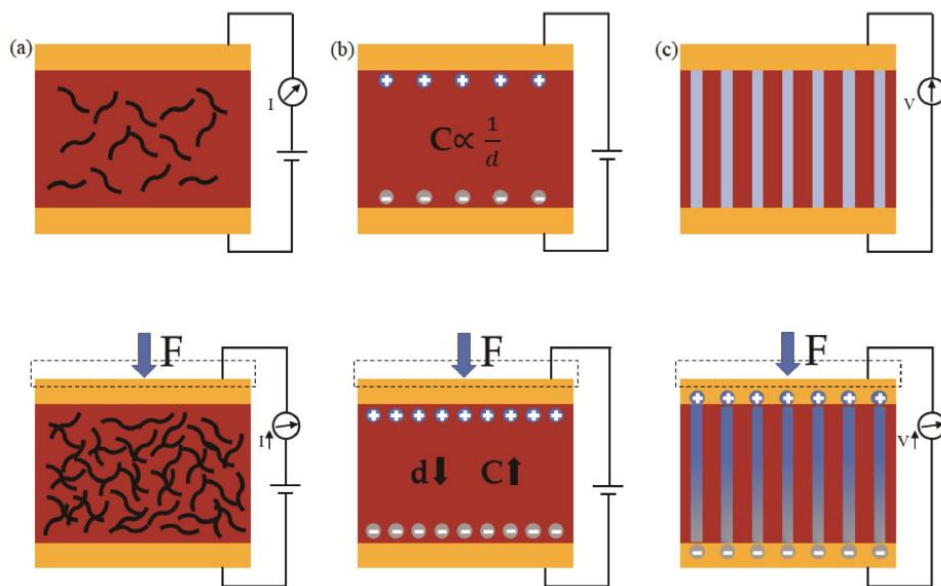


Figure 1.7. Schematic illustrations of three common transduction methods: (a) piezoresistivity, (b) capacitance, and (c) piezoelectricity [39].

Piezoresistive pressure sensors are some of the most reported and developed micromachine devices [40]. Capacitive sensor converts a change in position, or properties of the dielectric material, into an electrical signal. They are realized by varying any of the three parameters of a capacitor: distance between the plates (d), area of capacitive plates (A), and dielectric constant (ϵ_r). A number of different kinds of capacitance-based sensors are used in level measurement [41], but relatively to force sensors advantages of piezoresistive sensing compared to capacitive sensing include ease of differential pressure sensing configurations and freedom from the film stress related errors and failures of surface micromachining [42]. Piezoelectric pressure sensors are mainly composed of piezoelectric sensitive materials, which can convert mechanical energy and electric energy into each other. When the material is deformed by an external pressure, positive and negative charges separation occurs within the functional material. On the two opposite surfaces of the material, there will appear positive and negative charges arranged in opposite directions, and a potential difference will be formed inside. These potential differences are examined to determine the effect of external forces [43].

Generally, the piezoresistive sensors, as a kind of typical pressure sensor, are promising due to specific attractive advantages including uncomplicated signal collection, simple and economical manufacture, and practical characteristics [41-42]. Silicone is used for pressure sensors, because it combines well-established electronic properties with excellent mechanical properties. For that reason, it is used for the production of pressure sensors, where the piezoresistive material (especially metals) is supported by a thick silicone rim [46]. Besides silicone, a wide variety of materials have been developed including elastomer polymers, embedding carbon nanotubes (CNTs), graphene (containing reduced grapheneoxide), metal organic frameworks, and conductive nanowires, as seen in next paragraph[47].

In addition to the materials used, both as a matrix and as a conductive filler, a key role for the application of these systems is represented by the structure

geometry. Most of the structures for sensors are either 3D conductive network formed by roughening the surface of sensing materials [48], or 3D microporous materials [49]. A large variety of ingenious structures have also been developed for improving the sensitivity of pressure sensor, such as interlocking microstructures [50], pyramid arrays [51], microgrooves [48], and microdome arrays [52].

1.3. Piezoresistive composite materials

The structure of a piezoresistive sensor usually include a sensitive component (which plays a decisive role in the sensor), electrodes and electrical wires. In case of the flexible strain sensors, the working principle is to transform the deformation into a change in resistance, including contact resistance, tunneling effect and the own resistance of a conductor, and the change in resistance is represented by the change in current at a constant voltage. The performance of a strain sensor is evaluated based on gauge factor, durability, response time and the linearity between strain, static and dynamic stability, strain range and relative change in resistance. Recently, polymer composites and conductive fillers have been comprehensively used to fabricate flexible strain sensors. Among them, carbon-based nanomaterials, including carbon nanotubes (CNTs) [53], graphene [54], carbon-based nanofibers [55], and carbon black nanoparticles (CBNPs) [56].

Graphene, a monoatomic thin sp^2 bonded honeycomb carbon film (Figure 1.8a), thanks to features like the extreme stiffness (with Young's modulus of 1 TPa) [57], super flexibility, stretchability up to 20% [58], and excellent electrical conductivity compared to any other nanomaterials [59], is a promising material for application in micro electro mechanical systems (MEMS), composites, etc [60]. The resistivity of graphene varies linearly with strain [61], and this piezoresistive effect can be used to connect the mechanical and the electrical domains, through the development of various strain sensors [62]. The functionalization of graphene, to reduce the cohesive force between the graphene

molecules in different forms, causes significant changes in its physicochemical properties, thus increasing its end applications [63]. Graphene high electron mobility ($200,000 \text{ cm}^2 \text{ V}^{-1} \text{ s}^{-1}$ at electron density $\sim 2 \cdot 10^{11} \text{ cm}^{-2}$), high electrical conductivity ($\sim 1.0 \cdot 10^8 \text{ S/m}$), highest current density ($\sim 1.6 \cdot 10^9 \text{ A/cm}^2$), high melting point (4510 K), high thermal conductivity ($2000\text{--}4000 \text{ W m}^{-1} \text{ K}^{-1}$, 5000 W/m K), contribute to its application in electrochemical sensors, strain sensors and electrical sensors [64].

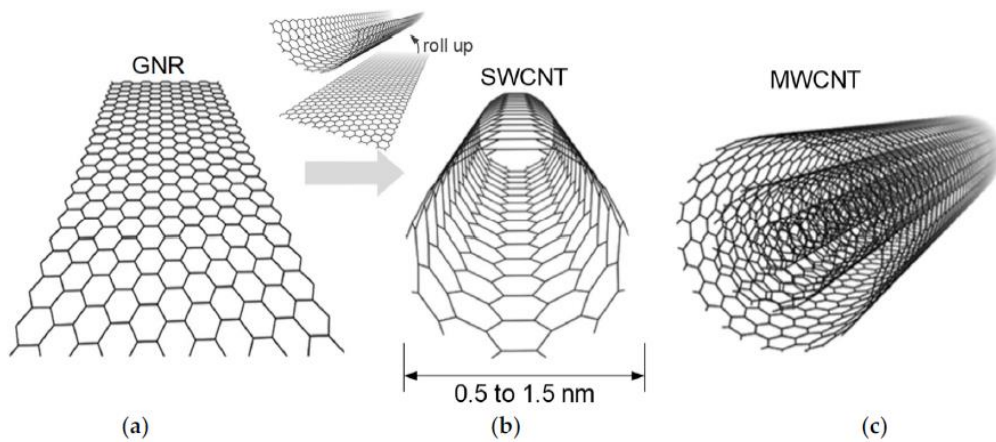


Figure 1.8. Schematics of (a) monolayer graphene nanoribbon (GNR), (b) single-walled carbon nanotube (SWCNT), and (c) multi-walled carbon nanotube (MWCNT) [65].

The use of CNTs for piezoresistive strain sensors has acquired significant attention due to their unique electromechanical properties. Electronically, depending on the graphene lattice orientation, single-walled carbon nanotubes can act as metallic, semiconducting, or small-gap semiconducting, but also their electromechanical properties are very interesting [66], and could be useful in applications for piezoresistive strain sensors such as strain gauges.

Mechanical, electrical, thermal, and optical conductivity are influenced from the structure of carbon nanotubes. For example, the band gap of semiconducting single-walled carbon nanotubes is dependent on the diameter. An increase in diameter leads to a decrease in the band gap [67]. There are two main types of

CNTs, which differentiate according to their structure: single-walled carbon nanotubes (Figure 1.8b), as a seamless cylinder achieved by rolling up a section of a graphene sheet, and multi-walled carbon nanotubes (Figure 1.8c), which are made of multiple rolled layers of graphene sheets with inner diameters as small as those of the single-walled carbon nanotubes, which can be up to tens of nanometers [68]. Carbon nanotubes can act as good conductors because of their one dimensional structures, which allow electronic transport to occur ballistically [69]. Multiwalled carbon nanotubes have been found to have an intrinsic resistance of 0.2–0.4 k Ω s/ μ m [70], which is subjected to modification under strain, resulting in promising applications in piezoresistive devices.

Various polymers are combined with these carbon-based nanomaterials to obtain flexible and stable strain sensors. However, their fabrication processes are complex, it is dramatically difficult to uniformly diffuse these nanomaterials and control the assembly structures in polymers [71]. Recently, various assembly methods have been successfully developed to improve strain sensing performance; these assembly methods include ordered structures including films [72], and uniform mixing [73], yarns [74], foams [75], and fabrics [76], fibers [77], nanofiber membranes [78], and the properties of these strain sensors vary with the assembly method. Flexibility, conductivity, and mechanical properties of polymers must be considered for practical applications. For example Kordas and Pitkänen recently worked on piezoresistive carbon foams in sensing applications, obtaining interesting results [79]. In particular, they compared soft piezoresistive foams of pyrolyzed Melamine foams and their hierarchical structures with carbon nanotubes (CNTs) and nanofibers (CNFs), which displayed high gauge factors in a large strain window. In Figure 1.9 is reported the morphological structure observed with SEM.

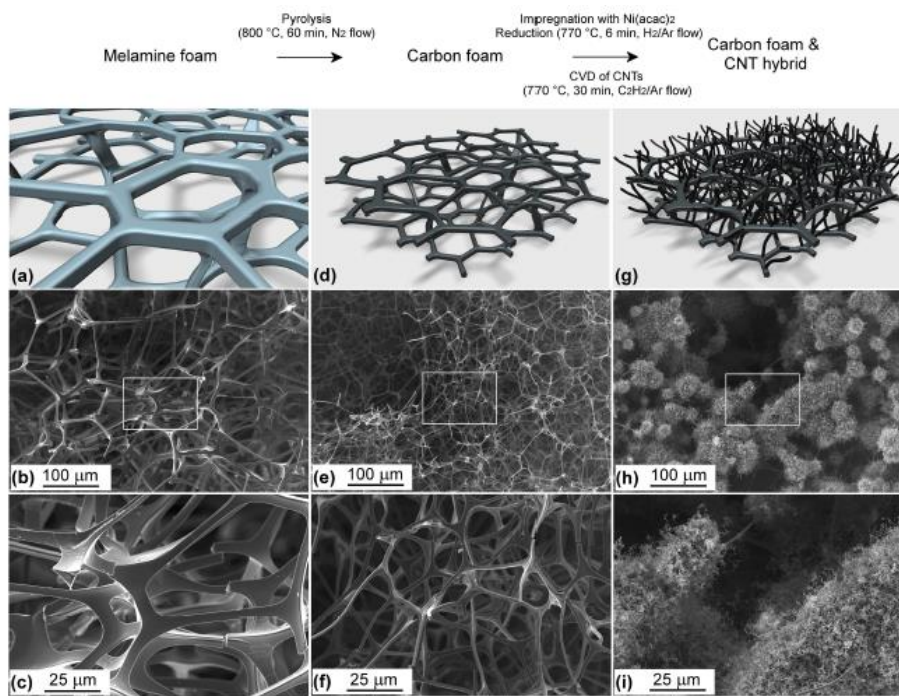


Figure 1.9. a,d,g) Schematic drawings of the original open pore structure melamine foam, carbon foam and hierarchical carbon foam and carbon nanotube hybrid, respectively. b,e,h) Low magnification scanning electron micrographs of the corresponding structures. c,f,i) Magnified images of the samples corresponding white rectangular selected areas in images (b,e,g) [79].

Resistance and stress measurements vs. mechanical strain show that both the carbon foam and its hierarchical structures with CNTs/CNFs have highly non-linear behavior (Figure 1.10). The Young's moduli of the materials increase with increasing compression between 1–65 kPa and 0.1–92 kPa for the foam and hierarchical structure, respectively.

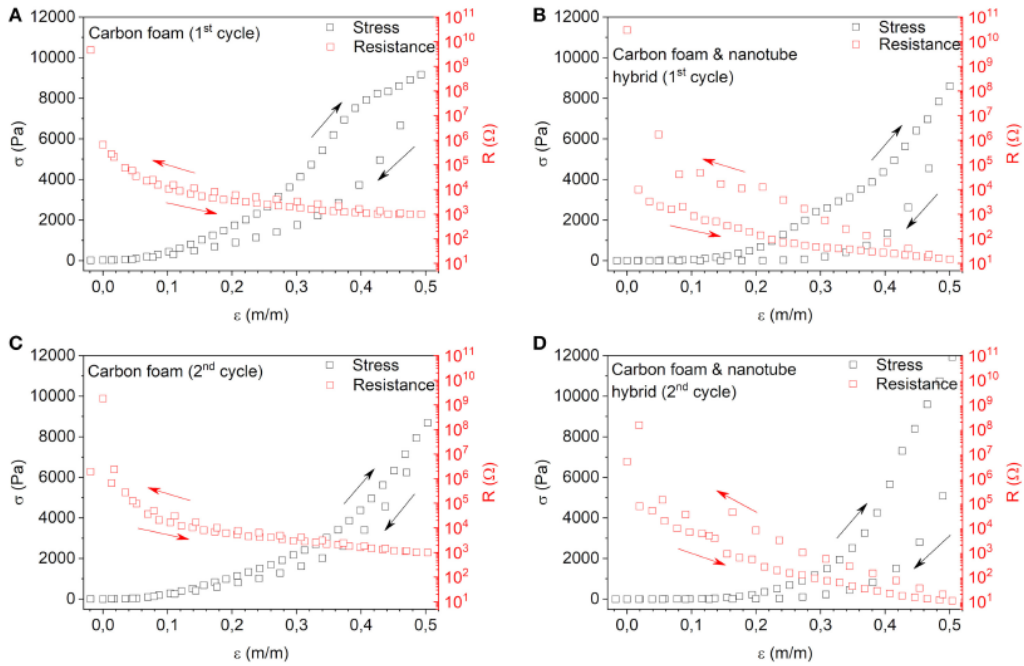


Figure 1.10. Electrical resistance and mechanical stress as a function of strain for (A) carbon foam and (B) hierarchical carbon foam and carbon nanotube hybrid structures measured in the first deformation cycle up to $\sim 50\%$ strain and back to the starting position. C, D) display the measured data obtained in the second deformation cycle for the corresponding specimens. The first resistance data point in each plot below 0% strain indicates insufficient contact with the electrodes in the experimental jig [79].

Both kinds of foams show giant piezoresistive gauge factors ($GF < -1000$) and withstand very large compressive deformations ($\epsilon \sim 0.5$) that are reversible after the first compression cycle thus enabling versatile strain gauge applications for displacement, deformation, and pressure sensing [79].

Although the sensitivities of composite strain sensors are lower than those of strain sensors fabricated directly from pure carbon nanomaterials, these polymer substrates can improve the linear response, strain range, and stability [80]. The stable interactions between carbon nanomaterials and polymers are essential for the sensing performance.

The great benefits of the low dimensional carbon nanostructures are the easy formation of entangled thin films, and the simple transfer onto elastomers enabling excellent strain sensor devices [81]. In fact, percolation and tunneling play crucial roles in the overall piezoresistive behavior of composites with conductive fillers (e.g., carbon or metal nanomaterials) embedded in polymer

matrices [82]. In this respect, several fillers, such as CNTs, carbon filaments, graphene and MXenes, dispersed in a number of polymer matrices, e.g., poly(dimethylsiloxane) [27], poly(styrene-butadiene-styrene) [83], poly(methyl methacrylate) [80], polysulfone [84], polyimide [85], epoxy [86], have proved to be as useful strain gauge materials. Carbon fillers are the most commonly used fillers in polymer-based composites, as the allotropic structures of carbon, such as carbon nanotubes and graphene, have recently been investigated for piezoresistive-sensing applications. Conductive rubber and carbon-fiber strain gauges are also widely used in the fabrication of tactile sensors. Conductive rubbers are usually fabricated by incorporating conductive particles of different types and dimensions into a silicone-based matrix.

New degrees of freedom (e.g., porosity, pore structure) are offered by foams of intrinsically conductive materials as well as their polymer composites, which enrich even further the palette of piezoresistive materials providing superior control over the mechanical and electromechanical properties [87]. In this regard, polyurethane foams have been investigated, coupling them with conductive wires for the electric connections [88].

An interesting example of piezoresistive foam with graphene was studied by Patole et al. [89], who characterized three-dimensional (3D) graphene foam (GF)-polydimethylsiloxane (PDMS) nanocomposites processed by a two-step approach. A polyurethane (PU) foam with graphene embedded (and aligned) in the pore walls was pyrolyzed and then impregnated with PDMS to form a GF-PDMS nanocomposite. The interconnected graphene network imparted excellent electrical conductivity (up to 2.85 S m^{-1} , the conductivity of PDMS is $0.25 \times 10^{-13} \text{ S m}^{-1}$) to the composite, and enabled ultrasensitive piezoresistive behavior. In fact, they obtained an initial gauge factor of 178, which is significantly higher than those reported in the literature. Cyclic compression-release tests conducted at different strain amplitudes demonstrated that both the mechanical and piezoresistive are fully reversible up to a maximum strain amplitude of 30% (Figure 1.11).

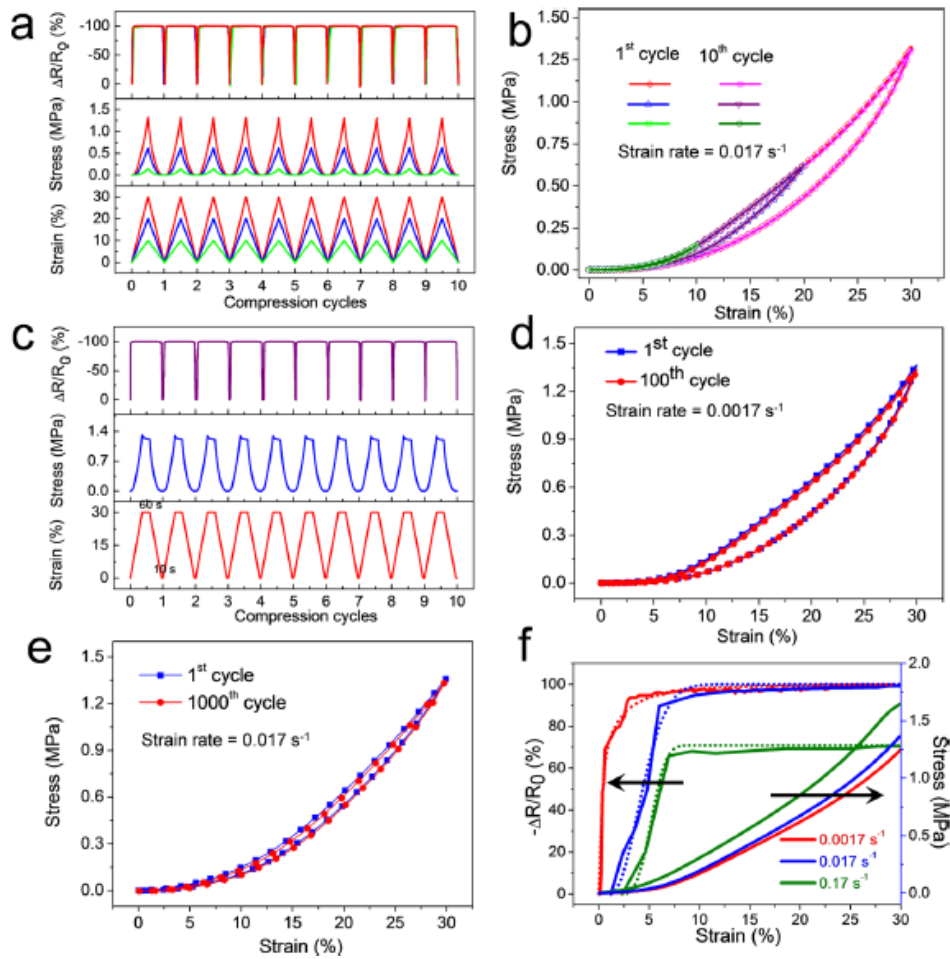


Figure 1.11. Cyclic strain sensing performance of GF-PDMS nanocomposites (0.7 wt % GC). (a) Stress, strain, and $\Delta R/R_0$ results for 10 compression cycles with 10%, 20%, and 30% strain amplitude. (b) Stress-strain curves for the first and last cycle. (c) Stress, strain, and $\Delta R/R_0$ for cyclic compression test with 60 s holding time at 30% strain and 10 s holding time at zero strain. (d) Stress-strain curves for the 1st and 100th cycle during a 100-cycle fatigue test with 30% strain amplitude and 0.0017 s^{-1} strain rate. (e) Stress-strain curves for the 1st, and 1000th cycle during a 1000-cycle fatigue test with 30% strain amplitude and 0.017 s^{-1} strain rate. (f) Compressive stress and $-\Delta R/R_0$ responses plotted as functions of the compressive strain for three different strain rates; exponential fitting curves are included for the $\Delta R/R_0$ data[89].

In functional carbon nanotube composites, it is possible to disperse a small amount of CNTs in insulating polymers. This new type of electrically conductive CNT/polymer nanocomposite can be applied to various fields, such as piezoresistive or resistance-type strain sensors of high sensitivity, electromagnetic interference materials, etc. [90].

Inks and fillers used can have the processability issues that composite materials encounter with the traditional techniques. It is possible to address these issues implementing additive manufacturing processes [91]. Additive manufacturing uses data computer-aided-design (CAD) software or 3D object scanners to direct hardware to deposit material, layer upon layer, in precise geometric shapes. As its name implies, additive manufacturing adds material to create an object. By contrast, when an object is created by traditional means, it is often necessary to remove material through milling, machining, carving, shaping or other means. In composite systems manufactured by additive technologies, the fillers can be chosen among metallic filler, carbon-based, or other conductive organic materials [92]. The performances of the printed conductive composite are determined also from the morphology, distribution, geometry, and adhesion of the filler particle in the composite matrix [93]. The concentration of the filler material should be around the percolation threshold (PH) to obtain a good variation of electrical resistance during stress application in strain sensors [94]. As concerns the mechanical standpoint, large concentrations of filler material lead to augmented stiffness and bare lower strain at break values. Lower concentrations than PH will lead to an exponential increase in tunneling resistance [95]. As an example, when a CNT network is dispersed in an elastic substrate, it exhibits two type of electrical resistance: an intrinsic resistance, and a dominating inner tube resistance; both of these give rise to the strain sensing phenomenon [96]. Dielectric inks with varied dielectric strengths and optical transmittance are now commercially available. Materials such as polydimethylsiloxane (PDMS) [97], poly(4-vinylphenol), poly(methyl methacrylate) (PMMA) [98], polyvinyl alcohol (PVA), polyaniline (PANI)[49], polystyrene terephthalate, polyimide (PI) [100], and thermoplastic polyurethane (TPU) [101] are commonly used for additive manufacturing of dielectrics. In the following further details on the carbon-based composites used for piezoresistive sensors are given.

Therefore, starting from the literature and the examples reported, with the intention of making an advancement of the state of the art, we have focused on 3D printed porous systems with carbonaceous fillers and which will be illustrated below in their main properties.

1.4. 3D printing

3D printing is an additive manufacturing process of joining materials to make objects from 3D model data, usually layer by layer, to produce components with complex geometries according to computer designs. 3D printing offers many advantages in the fabrication of composites, including high precision, customized geometry, and cost effectiveness. It is possible to refer to 3D printing also as additive manufacturing (AM), solid-freeform (SFF), or rapid prototyping (RP) [102]. Starting from a meshed 3D computer model that can be created by acquired image data or using a Computer-Aided Design (CAD) software, it is possible to create objects by adding materials to reduce waste while reaching satisfactory geometric accuracy [103]. Starting from 1988, when 3D printing was born, the interest around this technique has grown to explode, in terms of scientific publications and research fields, from the 2010 onwards (Figure 1.12).

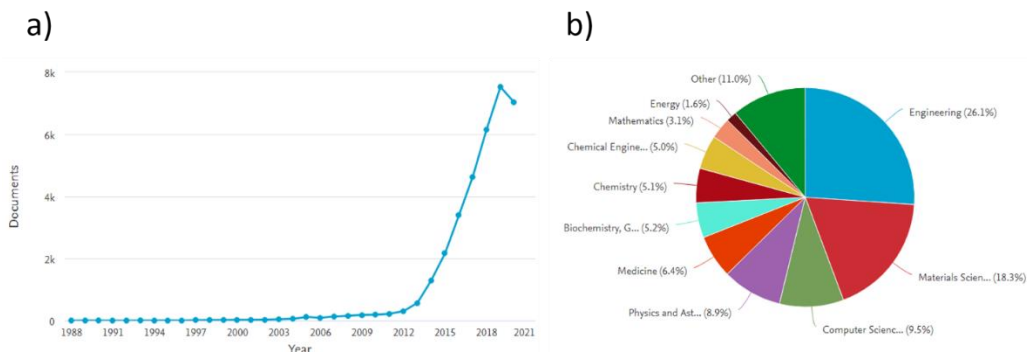


Figure 1.12. Scopus trend about 3D printing paper publication a), and research areas b), from 1988 to 2020.

The possible applications range from art fields for artifact replication or education [104], aerospace industries for creating complex lightweight structures

[105], architectural industries for structural models [106], and medical fields for printing tissues and organs [107]. Nowadays, 3D printed polymer products are also used as conceptual prototypes or functional components. A recent evolution of 3D printing with polymers consist in 3D printing of polymer composites, combining the matrix and particle, fiber or nanomaterial reinforcements, to achieve a system with high mechanical performance and excellent functionality, not attainable by any of the constituent alone [108]. A large number of thermoplastic polymer materials could be processed by 3D printing technology, such as polyamide (PA) [109], acrylonitrile butadiene styrene (ABS) [110], polycarbonate (PC) [111], polyurethane (PU) [112] and polylactic acid (PLA) [113], as well as thermosetting polymer materials like epoxy resins [114]. Epoxy resins are reactive materials that require thermal or UV-assisted curing to complete the polymerization process, passing from an initial liquid, whose viscosity rises as the curing proceeds [115].

An interesting feature of 3D printing, which combines process flexibility and high performance products, is the possibility of fabricating complex composite structures precisely, and without the typical waste associated to the traditional manufacturing techniques. The size and geometry of composites can be controlled with the help of CAD [116].

Various printing techniques have been employed to fabricate 3D printing polymer composites. The selection of fabrication technique depends on the starting materials, requirements of processing speed and resolution, costs and performance requirements of final products.

In the context of polymer nanocomposites and piezoresistive materials, a significant challenge for the scientific community is represented the by the achievement of an effective percolation pathway which allows the passage of an electric current at the minimum percentage of filler (percolation threshold). In particular, the Selective Laser Sintering (SLS) is one of the most interesting technology, able to build up easily the segregated filler network, starting from polymeric powder adequately prepared. It is focused on the sintering of

polymeric particles by a laser in the classic layer-by-layer mode. There are many polymers that can be used, from elastomeric to thermosetting, as well as conductive fillers. In this project we printed piezoresistive porous structures using Selective Laser Sintering (SLS), that's described below.

1.4.1. Selective laser sintering (SLS)

Selective laser sintering technique is similar to previously mentioned 3DP technique, as they are both based on powder processing. In SLS, a laser beam with a controlled path scans the powders to sinter them by heating, as shown in Figure 1.13.

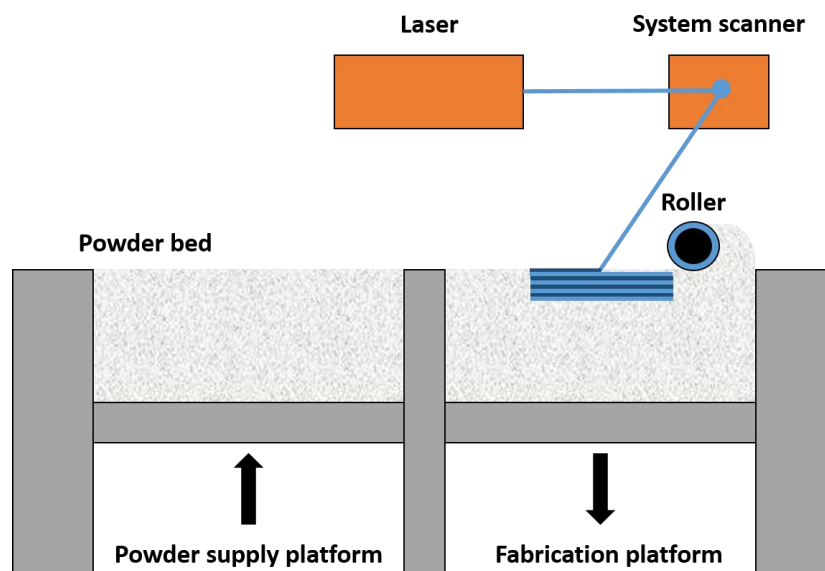


Figure 1.13. Schematic representation of SLS.

Under high power lasers, layer by layer, powders are fused together through molecular diffusion. Finally, unbounded powder should be removed[117]. Theoretically, any thermoplastic polymer in powder form could be processed by SLS technique. The powder particle size, laser power, scan spacing and scan speed determining the resolution of the printed part[118]. The choice of materials

used in SLS process is limited to the complex consolidation behavior and molecular diffusion process that occurs during sintering[119].

1.5. Aim of the PhD project

The aim of this PhD project was to design and realize elastomeric piezoresistive artifacts by using SLS 3D technology. In details, it was evaluated how the selected additive technology allows the formation of percolative pathways by starting from TPU powder wrapped with carbonaceous filler as raw materials and exploiting the concept of segregated morphology of carbonaceous fillers. Thanks to the SLS 3D printing technology, it will be possible to evaluate different porous geometries, realized by selected different unit cells, and understand if and how these geometries alongside with porosity and filler typology, affect both the mechanical and electrical properties of the artifacts. A comprehensive study is performed to correlate all identified variables as typology of selected unit cells (Diamond, Gyroid and Schwarz), porosity, filler (1D filler and 2D filler, and the mixture of 1D/2D fillers), to the final properties (thermal, mechanical, electrical, EMI shielding and piezoresistive properties) of systems printed by SLS technology. The objective is to design and identify new multifunctional porous conductive materials, with a sensitivity such as to be able to constitute new generation pressure sensors, easy to build thanks to the use of additive manufacturing, and with high mechanical and electromagnetic performance. The research results presented in the following chapters were published as open access papers respectively in Applied Sciences (2019, 9(5), 864, the second chapter) [120], and in Polymers (2020, 12(8), 1841, the third) [121] (both for MDPI press).

References

- [1] J. W. Cookson, "Theory of the piezo-resistive effect," *Phys. Rev.*, vol. 47, no. 2, p. 194, 1935.
- [2] H.-P. Phan, D. V. Dao, K. Nakamura, S. Dimitrijević, and N.-T. Nguyen, "The piezoresistive effect of SiC for MEMS sensors at high temperatures: a review," *J. Microelectromechanical Syst.*, vol. 24, no. 6, pp. 1663–1677, 2015.
- [3] P. Dineva, D. Gross, R. Müller, and T. Rangelov, "Piezoelectric materials," in *Dynamic fracture of piezoelectric materials*, Springer, 2014, pp. 7–32.
- [4] H. Tomlinson, "II. On the increase in resistance to the passage of an electric current produced on wires by stretching," *Proc. R. Soc. London*, vol. 25, no. 171–178, pp. 451–453, 1877.
- [5] J. J. Carr, "Sensors and Circuits, PTR Prentice-Hall." London, UK, 1993.
- [6] A. S. Fiorillo, C. D. Critello, and S. A. Pullano, "Theory, technology and applications of piezoresistive sensors: A review," *Sensors Actuators A Phys.*, vol. 281, pp. 156–175, 2018.
- [7] V. J. Lumelsky, M. S. Shur, and S. Wagner, "Sensitive skin," *IEEE Sens. J.*, vol. 1, no. 1, pp. 41–51, 2001.
- [8] L. Wang, J. Li, and Y. Han, "A prototype of piezoresistive fringe-electrodes-element based on conductive polymer composite," *IEEE Trans. Electron Devices*, vol. 61, no. 1, pp. 129–135, 2013.
- [9] Y. S. Rim, S. Bae, H. Chen, N. De Marco, and Y. Yang, "Recent progress in materials and devices toward printable and flexible sensors," *Adv. Mater.*, vol. 28, no. 22, pp. 4415–4440, 2016.
- [10] K. Weiss and H. Woern, "Tactile sensor system for an anthropomorphic

robotic hand,” 2004.

- [11] H. Nakamoto, F. Kobayashi, N. Imamura, and H. Shirasawa, “Universal robot hand equipped with tactile and joint torque sensors (development and experiments on stiffness control and object recognition),” in *Proc. of the 10th World Multi-Conference on Systemics, Cybernetics and Informatics*, 2006, vol. 2, pp. 347–352.
- [12] L. Karasek, B. Meissner, S. Asai, and M. Sumita, “Percolation concept: polymer-filler gel formation, electrical conductivity and dynamic electrical properties of carbon-black-filled rubbers,” *Polym. J.*, vol. 28, no. 2, pp. 121–126, 1996.
- [13] R. Taherian, “Development of an equation to model electrical conductivity of polymer-based carbon nanocomposites,” *ECS J. Solid State Sci. Technol.*, vol. 3, no. 6, p. M26, 2014.
- [14] M. H. Al-Saleh and U. Sundararaj, “A review of vapor grown carbon nanofiber/polymer conductive composites,” *Carbon N. Y.*, vol. 47, no. 1, pp. 2–22, 2009.
- [15] J. Gurland, “Multidimensional Gaussian Distributions (Kenneth S. Miller).” Society for Industrial and Applied Mathematics, 1966.
- [16] E. J. Garboczi, K. A. Snyder, J. F. Douglas, and M. F. Thorpe, “Geometrical percolation threshold of overlapping ellipsoids,” *Phys. Rev. E*, vol. 52, no. 1, p. 819, 1995.
- [17] N. Yousefi *et al.*, “Simultaneous in situ reduction, self-alignment and covalent bonding in graphene oxide/epoxy composites,” *Carbon N. Y.*, vol. 59, pp. 406–417, 2013.
- [18] Q. Li *et al.*, “Ultrahigh thermal conductivity of assembled aligned multilayer graphene/epoxy composite,” *Chem. Mater.*, vol. 26, no. 15,

pp. 4459–4465, 2014.

- [19] F. Xiang *et al.*, “Stiff and Transparent Multilayer Thin Films Prepared Through Hydrogen-Bonding Layer-by-Layer Assembly of Graphene and Polymer,” *Adv. Funct. Mater.*, vol. 26, no. 13, pp. 2143–2149, 2016.
- [20] C. Liu, H. Yan, Z. Chen, L. Yuan, and T. Liu, “Enhanced tribological properties of bismaleimides filled with aligned graphene nanosheets coated with Fe₃O₄ nanorods,” *J. Mater. Chem. A*, vol. 3, no. 19, pp. 10559–10565, 2015.
- [21] B. Xu *et al.*, “Thermo-compression-aligned functional graphene showing anisotropic response to in-plane stretching and out-of-plane bending,” *J. Mater. Sci.*, vol. 53, no. 9, pp. 6574–6585, 2018.
- [22] P. Ren, D. Yan, T. Chen, B. Zeng, and Z. Li, “Improved properties of highly oriented graphene/polymer nanocomposites,” *J. Appl. Polym. Sci.*, vol. 121, no. 6, pp. 3167–3174, 2011.
- [23] S. Versavaud, G. Regnier, G. Gouadec, and M. Vincent, “Influence of injection molding on the electrical properties of polyamide 12 filled with multi-walled carbon nanotubes,” *Polymer (Guildf.)*, vol. 55, no. 26, pp. 6811–6818, 2014.
- [24] X. Gan *et al.*, “Simultaneous realization of conductive segregation network microstructure and minimal surface porous macrostructure by SLS 3D printing,” *Mater. Des.*, vol. 178, p. 107874, 2019.
- [25] G. Ausanio *et al.*, “Giant resistivity change induced by strain in a composite of conducting particles in an elastomer matrix,” *Sensors Actuators A Phys.*, vol. 127, no. 1, pp. 56–62, 2006.
- [26] J. Hwang *et al.*, “Poly (3-hexylthiophene) wrapped carbon nanotube/poly (dimethylsiloxane) composites for use in finger-sensing piezoresistive

- pressure sensors,” *Carbon N. Y.*, vol. 49, no. 1, pp. 106–110, 2011.
- [27] Y. Hou, D. Wang, X.-M. Zhang, H. Zhao, J.-W. Zha, and Z.-M. Dang, “Positive piezoresistive behavior of electrically conductive alkyl-functionalized graphene/polydimethylsilicone nanocomposites,” *J. Mater. Chem. C*, vol. 1, no. 3, pp. 515–521, 2013.
- [28] T. Ding, L. Wang, and P. Wang, “Changes in electrical resistance of carbon-black-filled silicone rubber composite during compression,” *J. Polym. Sci. part b Polym. Phys.*, vol. 45, no. 19, pp. 2700–2706, 2007.
- [29] Jkw. Sandler, J. E. Kirk, I. A. Kinloch, M. S. P. Shaffer, and A. H. Windle, “Ultra-low electrical percolation threshold in carbon-nanotube-epoxy composites,” *Polymer (Guildf.)*, vol. 44, no. 19, pp. 5893–5899, 2003.
- [30] J. Fraden, “Handbook of modern sensors: physics, designs, and applications.” American Association of Physics Teachers, 1998.
- [31] Y. Zhang, N. Anderson, S. Bland, S. Nutt, G. Jursich, and S. Joshi, “All-printed strain sensors: Building blocks of the aircraft structural health monitoring system,” *Sensors Actuators A Phys.*, vol. 253, pp. 165–172, 2017.
- [32] M. I. Tiwana, S. J. Redmond, and N. H. Lovell, “A review of tactile sensing technologies with applications in biomedical engineering,” *Sensors Actuators A Phys.*, vol. 179, pp. 17–31, 2012.
- [33] A. Damilano *et al.*, “Commercial tactile sensors for hand exoskeletons: practical considerations for ultra-low cost and very-low complexity read-out,” *IEEE Instrum. Meas. Mag.*, vol. 19, no. 5, pp. 49–56, 2016.
- [34] N. K. Rana, “Application of force sensing resistor (FSR) in design of pressure scanning system for plantar pressure measurement,” in 2009

Second International Conference on Computer and Electrical Engineering, 2009, vol. 2, pp. 678–685.

- [35] S. K. Bahadır, “Identification and modeling of sensing capability of force sensing resistor integrated to E-textile structure,” *IEEE Sens. J.*, vol. 18, no. 23, pp. 9770–9780, 2018.
- [36] X. Jiang, K. Kim, S. Zhang, J. Johnson, and G. Salazar, “High-temperature piezoelectric sensing,” *Sensors*, vol. 14, no. 1, pp. 144–169, 2014.
- [37] T. Okatani, H. Takahashi, K. Noda, T. Takahata, K. Matsumoto, and I. Shimoyama, “A tactile sensor using piezoresistive beams for detection of the coefficient of static friction,” *Sensors*, vol. 16, no. 5, p. 718, 2016.
- [38] K. N. Bhat, “Silicon micromachined pressure sensors,” *J. Indian Inst. Sci.*, vol. 87, no. 1, p. 115, 2012.
- [39] W. Chen and X. Yan, “Progress in achieving high-performance piezoresistive and capacitive flexible pressure sensors: A review,” *J. Mater. Sci. Technol.*, vol. 43, pp. 175–188, 2020.
- [40] M. Esashi, S. Sugiyama, K. Ikeda, Y. Wang, and H. Miyashita, “Vacuum-sealed silicon micromachined pressure sensors,” *Proc. IEEE*, vol. 86, no. 8, pp. 1627–1639, 1998.
- [41] B. Kumar, G. Rajita, and N. Mandal, “A review on capacitive-type sensor for measurement of height of liquid level,” *Meas. Control*, vol. 47, no. 7, pp. 219–224, 2014.
- [42] A. A. Barlian and W. Park, “JRM Jr., AJ Rastegar and BL Pruitt,” *Proc. IEEE*, vol. 97, p. 513, 2009.
- [43] F. Xu *et al.*, “Recent developments for flexible pressure sensors: a review,” *Micromachines*, vol. 9, no. 11, p. 580, 2018.

- [44] W. He *et al.*, “Polypyrrole/silver coaxial nanowire aero-sponges for temperature-independent stress sensing and stress-triggered joule heating,” *ACS Nano*, vol. 9, no. 4, pp. 4244–4251, 2015.
- [45] W. Cai, Y. Huang, D. Wang, C. Liu, and Y. Zhang, “Piezoresistive behavior of graphene nanoplatelets/carbon black/silicone rubber nanocomposite,” *J. Appl. Polym. Sci.*, vol. 131, no. 3, 2014.
- [46] S. M. Sze, *Semiconductor sensors*. John Wiley & Sons, 1994.
- [47] Y. Lu, M. C. Biswas, Z. Guo, J.-W. Jeon, and E. K. Wujcik, “Recent developments in bio-monitoring via advanced polymer nanocomposite-based wearable strain sensors,” *Biosens. Bioelectron.*, vol. 123, pp. 167–177, 2019.
- [48] L. Pan *et al.*, “An ultra-sensitive resistive pressure sensor based on hollow-sphere microstructure induced elasticity in conducting polymer film,” *Nat. Commun.*, vol. 5, no. 1, pp. 1–8, 2014.
- [49] Y. Wu *et al.*, “Channel crack-designed gold@ PU sponge for highly elastic piezoresistive sensor with excellent detectability,” *ACS Appl. Mater. Interfaces*, vol. 9, no. 23, pp. 20098–20105, 2017.
- [50] J. Park *et al.*, “Ultrasensitive piezoresistive pressure sensors based on interlocked micropillar arrays,” *Bionanoscience*, vol. 4, no. 4, pp. 349–355, 2014.
- [51] C. Choong *et al.*, “Highly stretchable resistive pressure sensors using a conductive elastomeric composite on a micropyramid array,” *Adv. Mater.*, vol. 26, no. 21, pp. 3451–3458, 2014.
- [52] W. Zhong *et al.*, “A nanofiber based artificial electronic skin with high pressure sensitivity and 3D conformability,” *Nanoscale*, vol. 8, no. 24, pp. 12105–12112, 2016.

- [53] J. Di *et al.*, “Carbon-nanotube fibers for wearable devices and smart textiles,” *Adv. Mater.*, vol. 28, no. 47, pp. 10529–10538, 2016.
- [54] H. Kim and J.-H. Ahn, “Graphene for flexible and wearable device applications,” *Carbon N. Y.*, vol. 120, pp. 244–257, 2017.
- [55] S. Wu *et al.*, “Novel electrically conductive porous PDMS/carbon nanofiber composites for deformable strain sensors and conductors,” *ACS Appl. Mater. Interfaces*, vol. 9, no. 16, pp. 14207–14215, 2017.
- [56] X. Guo *et al.*, “Highly stretchable strain sensor based on SWCNTs/CB synergistic conductive network for wearable human-activity monitoring and recognition,” *Smart Mater. Struct.*, vol. 26, no. 9, p. 95017, 2017.
- [57] C. Lee, X. Wei, J. W. Kysar, and J. Hone, “Measurement of the elastic properties and intrinsic strength of monolayer graphene,” *Science (80-.)*, vol. 321, no. 5887, pp. 385–388, 2008.
- [58] K. S. Kim *et al.*, “Large-scale pattern growth of graphene films for stretchable transparent electrodes,” *Nature*, vol. 457, no. 7230, pp. 706–710, 2009.
- [59] J.-H. Chen, C. Jang, S. Xiao, M. Ishigami, and M. S. Fuhrer, “Intrinsic and extrinsic performance limits of graphene devices on SiO₂,” *Nat. Nanotechnol.*, vol. 3, no. 4, pp. 206–209, 2008.
- [60] S. Shrestha and S. Ranjit, “Suspended graphene applications in NEMS and MEMS,” in *2016 13th International Conference on Electrical Engineering/Electronics, Computer, Telecommunications and Information Technology (ECTI-CON)*, 2016, pp. 1–4.
- [61] A. A. Barlian, W.-T. Park, J. R. Mallon, A. J. Rastegar, and B. L. Pruitt, “Semiconductor piezoresistance for microsystems,” *Proc. IEEE*, vol. 97, no. 3, pp. 513–552, 2009.

- [62] S.-H. Bae, Y. Lee, B. K. Sharma, H.-J. Lee, J.-H. Kim, and J.-H. Ahn, “Graphene-based transparent strain sensor,” *Carbon N. Y.*, vol. 51, pp. 236–242, 2013.
- [63] F. V. Ferreira *et al.*, *Functionalizing Graphene and carbon nanotubes: a review*. Springer, 2016.
- [64] C.-W. Huang, J.-Y. Chen, C.-H. Chiu, C.-L. Hsin, T.-Y. Tseng, and W.-W. Wu, “Observing the evolution of graphene layers at high current density,” *Nano Res.*, vol. 9, no. 12, pp. 3663–3670, 2016.
- [65] W.-S. Zhao, K. Fu, D.-W. Wang, M. Li, G. Wang, and W.-Y. Yin, “Mini-Review: Modeling and performance analysis of nanocarbon interconnects,” *Appl. Sci.*, vol. 9, no. 11, p. 2174, 2019.
- [66] A. Maiti, A. Svizhenko, and M. P. Anantram, “Electronic transport through carbon nanotubes: Effects of structural deformation and tube chirality,” *Phys. Rev. Lett.*, vol. 88, no. 12, p. 126805, 2002.
- [67] G. Dresselhaus, M. S. Dresselhaus, and R. Saito, *Physical properties of carbon nanotubes*. World scientific, 1998.
- [68] S. Iijima, “Helical microtubules of graphitic carbon,” *Nature*, vol. 354, no. 6348, pp. 56–58, 1991.
- [69] W. Liang, M. Bockrath, D. Bozovic, J. H. Hafner, M. Tinkham, and H. Park, “Fabry-Perot interference in a nanotube electron waveguide,” *Nature*, vol. 411, no. 6838, pp. 665–669, 2001.
- [70] M. Zamkov, A. S. Alnaser, B. Shan, Z. Chang, and P. Richard, “Probing the intrinsic conductivity of multiwalled carbon nanotubes,” *Appl. Phys. Lett.*, vol. 89, no. 9, p. 93111, 2006.
- [71] M. Amjadi, K. Kyung, I. Park, and M. Sitti, “Stretchable, skin-mountable, and wearable strain sensors and their potential applications: a

- review,” *Adv. Funct. Mater.*, vol. 26, no. 11, pp. 1678–1698, 2016.
- [72] S. Luo and T. Liu, “SWCNT/Graphite nanoplatelet hybrid thin films for self-temperature-compensated, highly sensitive, and extensible piezoresistive sensors,” *Adv. Mater.*, vol. 25, no. 39, pp. 5650–5657, 2013.
- [73] L. Liu and D. Zhang, “The sensitive electrical response of reduced graphene oxide–polymer nanocomposites to large deformation,” *Compos. Part A Appl. Sci. Manuf.*, vol. 75, pp. 46–53, 2015.
- [74] Z. Wang *et al.*, “Polyurethane/cotton/carbon nanotubes core-spun yarn as high reliability stretchable strain sensor for human motion detection,” *ACS Appl. Mater. Interfaces*, vol. 8, no. 37, pp. 24837–24843, 2016.
- [75] B. Hao, L. Mu, Q. Ma, S. Yang, and P.-C. Ma, “Stretchable and compressible strain sensor based on carbon nanotube foam/polymer nanocomposites with three-dimensional networks,” *Compos. Sci. Technol.*, vol. 163, pp. 162–170, 2018.
- [76] X. Liu *et al.*, “A highly sensitive graphene woven fabric strain sensor for wearable wireless musical instruments,” *Mater. Horizons*, vol. 4, no. 3, pp. 477–486, 2017.
- [77] J. Lee *et al.*, “Highly sensitive multifilament fiber strain sensors with ultrabroad sensing range for textile electronics,” *ACS Nano*, vol. 12, no. 5, pp. 4259–4268, 2018.
- [78] Q. Wang, M. Jian, C. Wang, and Y. Zhang, “Carbonized silk nanofiber membrane for transparent and sensitive electronic skin,” *Adv. Funct. Mater.*, vol. 27, no. 9, p. 1605657, 2017.
- [79] K. Kordas and O. Pitkänen, “Piezoresistive Carbon Foams in Sensing Applications,” *Front. Mater.*, vol. 6, p. 93, 2019.

- [80] I. Kang, M. J. Schulz, J. H. Kim, V. Shanov, and D. Shi, "A carbon nanotube strain sensor for structural health monitoring," *Smart Mater. Struct.*, vol. 15, no. 3, p. 737, 2006.
- [81] E. P. Gilshteyn, D. Amanbayev, A. S. Anisimov, T. Kallio, and A. G. Nasibulin, "All-nanotube stretchable supercapacitor with low equivalent series resistance," *Sci. Rep.*, vol. 7, no. 1, pp. 1–9, 2017.
- [82] S. Stassi, V. Cauda, G. Canavese, and C. F. Pirri, "Flexible tactile sensing based on piezoresistive composites: A review," *Sensors*, vol. 14, no. 3, pp. 5296–5332, 2014.
- [83] X. Wang *et al.*, "Highly sensitive and stretchable piezoresistive strain sensor based on conductive poly (styrene-butadiene-styrene)/few layer graphene composite fiber," *Compos. Part A Appl. Sci. Manuf.*, vol. 105, pp. 291–299, 2018.
- [84] A. I. Oliva-Avilés, F. Avilés, and V. Sosa, "Electrical and piezoresistive properties of multi-walled carbon nanotube/polymer composite films aligned by an electric field," *Carbon N. Y.*, vol. 49, no. 9, pp. 2989–2997, 2011.
- [85] Y. Ma *et al.*, "A highly flexible and sensitive piezoresistive sensor based on MXene with greatly changed interlayer distances. *Nat. Commun.* 8, 1207 (2017)." .
- [86] L. M. Chiacchiarelli, M. Rallini, M. Monti, D. Puglia, J. M. Kenny, and L. Torre, "The role of irreversible and reversible phenomena in the piezoresistive behavior of graphene epoxy nanocomposites applied to structural health monitoring," *Compos. Sci. Technol.*, vol. 80, pp. 73–79, 2013.
- [87] Y. Wicaksono, S. Teranishi, K. Nishiguchi, and K. Kusakabe, "Tunable induced magnetic moment and in-plane conductance of graphene in

- Ni/graphene/Ni nano-spin-valve-like structure: A first principles study,” *Carbon N. Y.*, vol. 143, pp. 828–836, 2019.
- [88] R. A. Russell, “An imaging force sensor for robotics applications,” *Trans. Inst. Eng. Aust. Mech. Eng.*, vol. 10, no. 3, pp. 223–227, 1985.
- [89] S. P. Patole, S. K. Reddy, A. Schiffer, K. Askar, B. G. Prusty, and S. Kumar, “Piezoresistive and mechanical characteristics of graphene foam nanocomposites,” *ACS Appl. Nano Mater.*, vol. 2, no. 3, pp. 1402–1411, 2019.
- [90] J.-P. Tessonier *et al.*, “Analysis of the structure and chemical properties of some commercial carbon nanostructures,” *Carbon N. Y.*, vol. 47, no. 7, pp. 1779–1798, 2009.
- [91] U. Kalsoom, P. N. Nesterenko, and B. Paull, “Recent developments in 3D printable composite materials,” *RSC Adv.*, vol. 6, no. 65, pp. 60355–60371, 2016.
- [92] W. Guo *et al.*, “Matrix-independent highly conductive composites for electrodes and interconnects in stretchable electronics,” *ACS Appl. Mater. Interfaces*, vol. 11, no. 8, pp. 8567–8575, 2019.
- [93] M. Amjadi, Y. J. Yoon, and I. Park, “Ultra-stretchable and skin-mountable strain sensors using carbon nanotubes–Ecoflex nanocomposites,” *Nanotechnology*, vol. 26, no. 37, p. 375501, 2015.
- [94] X. Huang and C. Zhi, *Polymer Nanocomposites*. Springer, 2016.
- [95] X. Zeng *et al.*, “Characteristics of the electrical percolation in carbon nanotubes/polymer nanocomposites,” *J. Phys. Chem. C*, vol. 115, no. 44, pp. 21685–21690, 2011.
- [96] J. Shi *et al.*, “Graphene reinforced carbon nanotube networks for wearable strain sensors,” *Adv. Funct. Mater.*, vol. 26, no. 13, pp. 2078–

2084, 2016.

- [97] S. C. B. Mannsfeld *et al.*, “Highly sensitive flexible pressure sensors with microstructured rubber dielectric layers,” *Nat. Mater.*, vol. 9, no. 10, pp. 859–864, 2010.
- [98] M.-L. Seol, J.-W. Han, D.-I. Moon, K. J. Yoon, C. S. Hwang, and M. Meyyappan, “All-printed triboelectric nanogenerator,” *Nano Energy*, vol. 44, pp. 82–88, 2018.
- [99] Y. Liu *et al.*, “Development of graphene oxide/polyaniline inks for high performance flexible microsupercapacitors via extrusion printing,” *Adv. Funct. Mater.*, vol. 28, no. 21, p. 1706592, 2018.
- [100] R. Yang *et al.*, “Transparent and flexible force sensor based on microextrusion 3D printing,” *Micro Nano Lett.*, vol. 13, no. 10, pp. 1460–1464, 2018.
- [101] C. Manganiello, D. Naso, F. Cupertino, O. Fiume, and G. Percoco, “Investigating the Potential of Commercial-Grade Carbon Black-Filled TPU for the 3D Printing of Compressive Sensors,” *Micromachines*, vol. 10, no. 1, p. 46, 2019.
- [102] A. Standard, “Standard terminology for additive manufacturing technologies,” *ASTM Int. F2792-12a*, 2012.
- [103] G. N. Levy, R. Schindel, and J.-P. Kruth, “Rapid manufacturing and rapid tooling with layer manufacturing (LM) technologies, state of the art and future perspectives,” *CIRP Ann.*, vol. 52, no. 2, pp. 589–609, 2003.
- [104] D. B. Short, “Use of 3D printing by museums: Educational exhibits, artifact education, and artifact restoration,” *3D Print. Addit. Manuf.*, vol. 2, no. 4, pp. 209–215, 2015.
- [105] H.-B. Lim, “Beyond 3G,” *IEEE POTENTIALS*, vol. 21, no. 4, pp. 18–23,

2002.

- [106] Y. W. D. Tay, B. Panda, S. C. Paul, N. A. Noor Mohamed, M. J. Tan, and K. F. Leong, “3D printing trends in building and construction industry: a review,” *Virtual Phys. Prototyp.*, vol. 12, no. 3, pp. 261–276, 2017.
- [107] U. Jammalamadaka and K. Tappa, “Recent advances in biomaterials for 3D printing and tissue engineering,” *J. Funct. Biomater.*, vol. 9, no. 1, p. 22, 2018.
- [108] T. Vivek, P. Arunkumar, A. S. Deshpande, M. Vinayak, R. M. Kulkarni, and A. Asif, “Development of polymer nano composite patterns using fused deposition modeling for rapid investment casting process,” in *AIP Conference Proceedings*, 2018, vol. 1943, no. 1, p. 20110.
- [109] C. Cai *et al.*, “Comparative study on 3D printing of polyamide 12 by selective laser sintering and multi jet fusion,” *J. Mater. Process. Technol.*, vol. 288, p. 116882, 2020.
- [110] M. Samykano, S. K. Selvamani, K. Kadirgama, W. K. Ngui, G. Kanagaraj, and K. Sudhakar, “Mechanical property of FDM printed ABS: influence of printing parameters,” *Int. J. Adv. Manuf. Technol.*, vol. 102, no. 9–12, pp. 2779–2796, 2019.
- [111] M. J. Reich, A. L. Woern, N. G. Tanikella, and J. M. Pearce, “Mechanical properties and applications of recycled polycarbonate particle material extrusion-based additive manufacturing,” *Materials (Basel)*, vol. 12, no. 10, p. 1642, 2019.
- [112] S. Peng *et al.*, “3D Printing Mechanically Robust and Transparent Polyurethane Elastomers for Stretchable Electronic Sensors,” *ACS Appl. Mater. Interfaces*, vol. 12, no. 5, pp. 6479–6488, 2020.

- [113] I. Anderson, "Mechanical properties of specimens 3D printed with virgin and recycled polylactic acid," *3D Print. Addit. Manuf.*, vol. 4, no. 2, pp. 110–115, 2017.
- [114] B. G. Compton and J. A. Lewis, "3D-printing of lightweight cellular composites," *Adv. Mater.*, vol. 26, no. 34, pp. 5930–5935, 2014.
- [115] H. Gu *et al.*, "An overview of multifunctional epoxy nanocomposites," *J. Mater. Chem. C*, vol. 4, no. 25, pp. 5890–5906, 2016.
- [116] F. Rengier *et al.*, "3D printing based on imaging data: review of medical applications," *Int. J. Comput. Assist. Radiol. Surg.*, vol. 5, no. 4, pp. 335–341, 2010.
- [117] S. Singh, S. Ramakrishna, and F. Berto, "3D Printing of polymer composites: A short review," *Mater. Des. Process. Commun.*, vol. 2, no. 2, p. e97, 2020.
- [118] I. Gibson and D. Shi, "Material properties and fabrication parameters in selective laser sintering process," *Rapid Prototyp. J.*, 1997.
- [119] R. D. Goodridge *et al.*, "Processing of a Polyamide-12/carbon nanofibre composite by laser sintering," *Polym. Test.*, vol. 30, no. 1, pp. 94–100, 2011.
- [120] A. Ronca *et al.*, "Selective laser sintering fabricated thermoplastic polyurethane/graphene cellular structures with tailorable properties and high strain sensitivity," *Appl. Sci.*, vol. 9, no. 5, p. 864, 2019.
- [121] G. Rollo *et al.*, "On the Synergistic Effect of Multi-Walled Carbon Nanotubes and Graphene Nanoplatelets to Enhance the Functional Properties of SLS 3D-Printed Elastomeric Structures," *Polymers (Basel)*, vol. 12, no. 8, p. 1841, 2020.

Chapter 2 | Selective laser sintering fabricated thermoplastic polyurethane/graphene high strain sensitivity

Abstract: Electrically conductive and flexible thermoplastic polyurethane/graphene (TPU/GE) porous structures were successfully fabricated by selective laser sintering (SLS) technique starting from GE-wrapped TPU powders. Several 3D mathematically defined architectures, with porosities from 20 to 80%, were designed by using triply periodic minimal surfaces (TMPS) equations corresponding to Schwarz (S), Diamond (D) and Gyroid (G) unit cells. The resulting three-dimensional porous structures exhibit an effective conductive network due to the segregation of graphene nanoplatelets previously assembled onto the TPU powder surface. GE nanoplatelets improve thermal stability of the TPU matrix, also increasing its glass transition temperature. Moreover, the porous structures realized by S geometry display higher elastic modulus values in comparison to D and G-based structures. Upon cyclic compression tests, all porous structures exhibit a robust negative piezoresistive behaviour, regardless of their porosity and geometry, with outstanding strain sensitivity. Gauge factor (GF) values of 12.4 at 8% strain are achieved for S structures at 40 and 60% porosity, and GF values up to 60 are obtained for deformations extents lower than 5%. Thermal conductivity of the TPU/GE structures significantly decreases with increasing porosity, while the effect of the structure architecture is less relevant. The TPU/GE porous structures herein reported hold great potential as flexible, highly sensitive, and stable strain sensors in wearable or implantable devices, as well as dielectric elastomer actuators.

Keywords: Selective laser sintering (SLS); thermoplastic polyurethane (TPU); graphene (GE); mathematically defined structures; piezoresistivity; strain sensors

2.1. Introduction

Additive manufacturing, also known as 3D printing (3DP), is an innovative manufacturing technology which allows to turn complex 3D models into real objects without special tooling and with extreme facility, cost and time savings alongside with high accuracy in the realization of specific complex items [1][2]. 3DP includes several technologies such as stereolithography (SLA) [3], fused deposition modeling (FDM) [4], and selective laser sintering (SLS) and some less common techniques [5][6][7]. Among them, SLS ensures the highest geometrical freedom and dimensional precision which allows the manufacturing of parts with well-defined prototypes and components applied in different fields including electronics, mechanics and biomedicine [1][8]. Starting from a computer-aided design (CAD) 3D model, SLS builds up objects by sintering and fusing powder material in a layer-by-layer approach, via a computer-controlled laser [9][10]. Generally, thermoplastic polymers are mostly used for the laser sintering process [11]. However, only a few polymers are now commercially available being polyamides (PA-11 and PA-12) the most used, while polystyrene [12], polycarbonate [13], thermoplastic polyurethane (TPU) [14] and their composites are seldom explored or used in specific sectors. Despite the continuous progress in the optimization of SLS technology, many critical issues still remain unsolved, including the possibility to manufacture multifunctional conductive parts able to exhibit both electrical conductivity alongside with lightweight and elastic properties. In this context, it is very interesting to develop new powders made up of conductive nanoparticles dispersed in or coated onto elastomeric particles [15][16]. Piezoresistive structures, realized by using conductive elastomeric polymers, are commonly used for load/pressure sensors and actuators due to their quick response to external stress [17]. In these systems, the mechanical deformation of the structure brings about a change in the conductive pathway by modifying the mean particle distance between the conductive nanoparticles and therefore the material's resistivity [18]. Several fillers that are able to realize a

3D interconnected conductive network such as carbon black (CB) [19], carbon fiber (CF) [20], carbon nanotubes (CNT) [21][22], and graphene (GE) [23][24] have been used for modifying the polymer matrix and realize conductive composites endowed with advanced functional properties including chemical sensing, capacitance, and piezoresistivity. Among them, GE has attracted huge interests because of its excellent conductivity (3000–5000 W/m*K), high carrier mobility ($\approx 10.000 \text{ cm}^2/\text{V*s}$), optical transparency ($\approx 97.7\%$), and high Young's modulus ($\approx 1 \text{ TPa}$) [25][26]. Thus, several recent studies have focused on the electrical and thermal conductivity of GE-based composites by using polydimethylsiloxane (PDMS) [27], polyamide-6 [28], natural rubber [29] as matrix. Among the elastomeric matrixes, thermoplastic polyurethane (TPU) is a versatile polymer, as its morphology is made up of a hard diisocyanate segment, and a soft segment [30][31] consisting of a tailor-designed alkyl, polyether or polyester chain. Due to its peculiar morphology, TPU exhibits unique thermomechanical properties and strong capability of shape recovery upon loading/unloading cycles [32]. Xia *et al.* already demonstrated the feasibility of SLS technique to construct compact 3D electrically conductive materials by processing TPU powder wrapped with CNTs [1]. They substantiate the selection of CNTs, as the best filler to allow the better coalescence of powders during the laser sintering process, in order to maximize the mechanical properties. Moreover, the possibility to using TPU powders wrapped with 2D filler as GE, which hinders to some extent the coalescence of particles during the sintering, and allow to tailor the structural and functional properties of the resulting porous structures in a value-range not yet explored. The control of pore morphology and dimension which depend on the shape of the unit cell, from which is generated the three-dimensional structure, affects their mechanical and electrical response, making them more sensitive to mechanical stress/strain, thus enhancing their stress sensor capability. Herein, it is investigated the effect of pore morphology and distribution on the thermal, mechanical and piezoresistive properties of porous structures fabricated by SLS technique by using a home-made powder

consisting of TPU wrapped with GE platelets (TPU/GE porous structures). 3D mathematically defined architectures have been designed and realized starting from triply periodic minimal surface (TMPS) geometry. More specifically, three different geometries have been used, namely Gyroid [33], Diamond [34] and Schwarz **Error. L'origine riferimento non è stata trovata.**, with an extent of porosity ranging from 20 to 80%. Electrical and thermal conductivity, mechanical strength, filler dispersion and interaction with the polymer matrix of the TPU/GE porous structures are investigated and correlated with their porosity and morphology. The reported results are of interest for the design and fabrication of novel 3D printable strain sensors as well as lightweight thermal conductors.

2.2. Materials and methods

A polyester-type thermoplastic polyurethane (TPU) was used as the matrix phase ($T_g = -14,2$ C and $T_m = 160$ C, LUVOSINT X92A-1 - Germany). Graphene material was provided by Deyang Carbonene Technology Co., Ltd., China, with a lateral size between 5 and 10 μm , thickness of 2-15 nm, and up to 20 layers. Silica nanoparticles, mainly used to promote the flowing of TPU particles, consists of fine powder with particle size less than 10 nm, and it was purchased from Nanjing Tianxing New Material Co., Ltd., China. All of the materials and reagents were used as received.

2.2.1. Preparation of TPU/GE nanocomposites powder

The method of preparing composite powder for SLS is of great importance, as it directly determines the dispersion of nanofiller in the polymer matrix, also affecting the properties of the SLS fabricated porous structures. GE was dispersed in ethanol and subjected to ultrasonication for 12 h, to get a homogenous dispersion. The TPU powders were then added to the GE suspension and mechanically stirred for 4 h. Then the mixture was filtered with a Buchner funnel under reduced pressure. The obtained GE-coated TPU powders were dried in a vacuum oven at 50 °C for 24 h. Subsequently, the TPU/GE

powders were sieved to remove particles with size over 40 μ m. In addition, 0.2 wt% silica was used to further improve the powder flowing ability.

2.2.2. Porous structures design by TPMS

To design 3D porous structures a mathematical approach has been used, starting from triply periodic minimal surfaces (TPMS) equations. TPMS are minimal surfaces periodic in three independent directions, extending infinitely and, in the absence of self-intersections, partitioning the space into two labyrinths. Wolfram Mathematica software was used to generate CAD-files that describe the surfaces of Gyroid (G), Diamond (D) and Schwarz (S) architectures at different porosity. The following trigonometric equations were used with boundary condition $x, y, z = [-3\pi; 3\pi]$:

$$G: \quad \sin(y) + \cos(y) \cdot \sin(z) + \cos(z) \cdot \sin(x) = C \quad (2.1)$$

$$D: \quad \sin(x) \cdot \sin(y) \cdot \sin(z) + \sin(x) \cdot \cos(y) \cdot \cos(z) + \cos(x) \cdot \sin(y) \cdot \cos(z) + \cos(x) \cdot \cos(y) \cdot \sin(z) = C \quad (2.2)$$

$$S: \quad G \cos(x) + \cos(y) + \cos(z) = C \quad (2.3)$$

In these equations, the C parameter is the offset which controls the porosity of the structures. An accurate study has been conducted in order to understand the correlation between percentage of porosity and offset value C (see Figure 2.1). Three different porosity values (40, 60 and 80%) have been set for each geometry in order to study the effect of porosity on thermal and electrical conductivity. Rhinoceros software was used to scale the CAD-files to the required dimensions in order to obtain a 10x10x10 mm³ sized cube. In the following, Gyroid, Diamond and Schwarz-based porous structures are labelled as GX, DX and SX, respectively, where G, D, or S represents the geometry and

X represents the % porosity. As an example, G20 stands for Gyroid-based architecture with 20% porosity.

2.2.3. Nanocomposite porous structure realization by SLS

A HT251P SLS Equipment (Farsoon Hi-tech, China) was used as 3D printer. The SLS procedure is described briefly as follows: graphene wrapped TPU powder was spread out on the sample tray and preheated at 60 °C, N₂ was used in the chamber as purging gas. The laser (5W power and 450μm focused beam diameter) selectively fused the powder based on the CAD model, according to the processing parameters reported in Table 2.1

Table 2.1. Sintering parameters adopted for processing TPU/GE composite powders.

Process parameters	Value
Laser power (W)	60
Laser scan spacing (μm)	100
Laser scan speed (m/s)	7.6
Part bed temperature (°C)	95
Powder feed temperature (°C)	65
Outline laser power (W)	5
Layer thickness (μm)	150

After processing, the porous specimens were allowed to cool down inside the equipment chamber for approximately 1h and then they were removed from printer, and sprayed with compressed air to remove non-sintered powder from the interstices and porosity.

2.2.4. Scanning electron microscopy (SEM)

The porous morphology of the several printed specimens was studied by scanning electron microscopy (SEM) by using a FEI Quanta 200 FEG-SEM

microscope. The samples were fixed on a support and metallized with a gold-palladium alloy to ensure better conductivity and prevent the formation of electrostatic charges.

2.2.5. *Transmission electron microscopy (TEM)*

Transmission electron microscopy (TEM) imaging was performed by using a Tecnai G2 Spirit TWIN electron microscope (FEI) operating at 120 kV on 100 μm TEM cryosections.

2.2.6. *Thermal properties*

Thermal properties of TPU and TPU/GE were measured by differential scanning calorimetry (DSC) and thermogravimetric analysis (TGA). The DSC measurements were performed with a TA Instrument DSC Q2000. Samples of 5 mg were heated up to 250 $^{\circ}\text{C}$ at a heating rate of 10 $^{\circ}\text{C}/\text{min}$, then cooled to -50 $^{\circ}\text{C}$ at 10 $^{\circ}\text{C}/\text{min}$ and reheated to 250 $^{\circ}\text{C}$ at 10 $^{\circ}\text{C}/\text{min}$ under nitrogen atmosphere.

Thermogravimetric analysis was carried out on approximately 8 mg samples by using a PerkinElmer Pyris Diamond TG/DTA. The samples were pre-heated to 90 $^{\circ}\text{C}$ at 10 $^{\circ}\text{C}/\text{min}$ for 10 min, then subject to a ramp up to 800 $^{\circ}\text{C}$ at a heating rate of 5 $^{\circ}\text{C}/\text{min}$ under nitrogen atmosphere.

2.2.7. *Raman spectra analysis*

Raman spectra were obtained using a Horiba Jobin Yvon LabRam ARAMIS model, with a 532 nm laser (green light), hole 300 μm , slit 300 μm , objective x50/0.50, grating 600, time 10 s.

2.2.8. *Mechanical and piezoresistive measurements*

Static compression tests were carried out by using a mechanical testing machine (Instron 5564 dynamometer) and the 10x10x10 mm^3 cubic specimens were compressed at a strain rate of 3 mm/min. Electrical and compression tests were carried out simultaneously to evaluate the piezoresistive properties of the

3D printed structures. Thus, coupled to the mechanical testing machine a multimeter (Agilent 34401A 6½ Digit Multimeter), which was controlled by a homemade LabVIEW program, was used to measure the change of electrical resistance with the applied load and induced deformation. Two electrodes, made of copper conductive tape, were glued on the top and on the bottom of the specimen and connected with the multimeter through copper wires. The mechanical properties were evaluated by submitting the samples to a cyclic compressive strain/unstrain up to 8% of initial value of the length of cubic sample, with a deformation rate of 3 mm/min, at 25 °C. Before measurement, the porous structures were pre-compressed to a strain value of 4%. The electrical resistance of the specimen was monitored simultaneously to compression testing. The strain sensitivity of the samples was expressed as Gauge Factor, $GF = (\Delta R/R_0)/\epsilon$, where $\Delta R/R_0$ is the resistance change rate and ϵ is the compression strain.

2.2.9. Thermal conductivity measurement

Porous cylindrical specimens, characterized by a height of 4 mm and a diameter of 21 mm were realized by SLS with the three proposed geometry (G, D and S) and used for thermal conductivity measurements. The thermal conductivity (λ) was measured by a Hot Disk thermal analyser (TPS2500).

2.3. Results and Discussion

2.3.1. Design and realization of the TPU/GE porous structures

TPU/GE composite powder was used in SLS printing process in order to build three porous structures by using Schwarz, Diamond and Gyroid unit cells. Moreover, an accurate study to understand the correlation between the offset factor (C) present in the equations (1), (2), and (3) and the structures porosity of the structure is reported in Figure 2.1. The porosity linearly decreases by

increasing the offset value, and this enables to design structures in a range of porosity (from 40 to 80%).

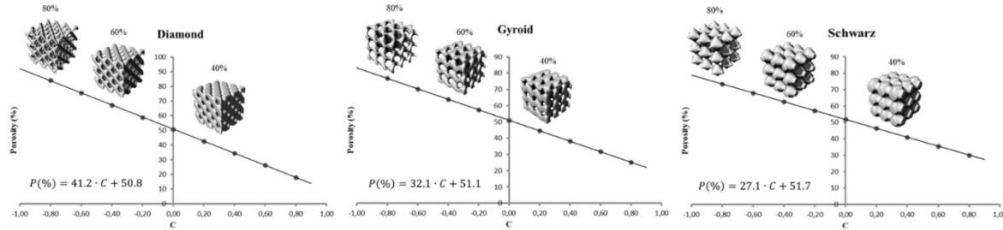


Figure 2.1. Correlation between percentage of porosity and C value for Diamond, Gyroid and Schwarz-based unit cells architectures.

Porous structures, consisting of $3 \times 3 \times 3$ unit cells, were SLS printed by using the TPU/GE composite powder with three different porosity values. Figure 2.2 clearly shows that the three different unit cells give rise to a different distribution of pores within the resulting 3D structure. In particular, the Schwarz unit cells bring about a structure with bigger pores and so the trabeculae between pores (i.e. struts in the foams) are bigger. The structures generated by G and D unit cells present more pores with smaller dimension and consequently the trabeculae have a smaller size.

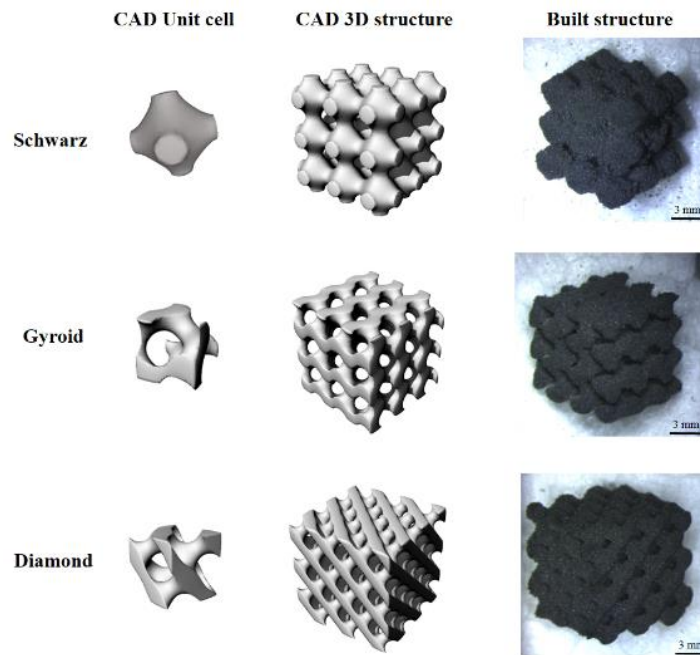


Figure 2.2. Visualization of the three designed porous structures. CAD-designs of the unit cells (left column); CAD-designs of 3x3x3 assembled structures (center column); photos of the TPU/GE SLS fabricated structures (right column).

The designed architectural features are preserved, and porosity is almost unaffected by the fabrication process as shown in Figure 2. These results clearly show the suitability of the TPU/GE powder to print porous structures with narrow pore size distributions and high pore interconnectivity by SLS manufacturing.

2.3.2. Chemical-physical and morphological characterization of the SLS manufactured foams

SLS processing involves the selective melting of the particle surface by using a laser beam. In this process, the TPU particles coalesce with each other, building up the desired 3D structure [1]. Since the TPU melt is highly viscous and no stress is generated during the process, the particle morphology is not significantly changed. Therefore, similarly to the CNTs [1], the GE sheets remain entrapped in between the particle boundaries, thereby forming a percolated conductive network, as sketched in Figure 2.3a. Low magnification SEM images (Figure

2.3b) show that the wall structure of the holes in the porous specimens consists of sintered TPU particles. High magnification images (Figure 2.3c) clearly demonstrate that the surface of the TPU particles is covered by GE platelets. TEM observations provide additional information on the morphology and microstructure of the samples. Figure 2.3d and 2.3e show the GE percolated network due to the filler segregation between the sintered TPU particles, with a thickness ranging from 200 to 500 nm.

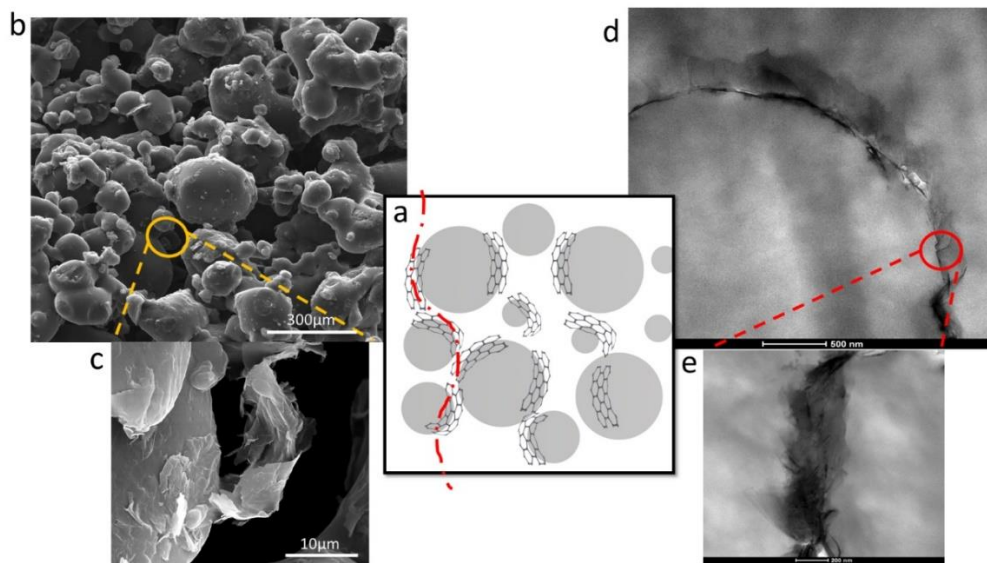


Figure 2.3. (a) Schematics of the microstructure of the fabricated porous TPU/GE composites (GE content 1.0 wt%), highlighting the percolated GE network at the interparticle boundary (red dashed line). SEM images of the (b) wall structure of the composite, and the (c) GE-wrapped TPU particle surface. (d, e) TEM images of the percolated GE network in the SLS-processed composites.

Raman spectroscopy was used to get insight on the effect of SLS processing on the structure of the GE platelets within the sintered porous structures. Raman spectra of TPU, GE powder before processing and GE in the fabricated porous structures are reported in Figure 2.4. The spectrum of pristine TPU shows the typical peaks of polyurethane, including the absorption peak of aromatic rings ($1470\text{-}1440\text{ cm}^{-1}$), the absorption peak at 1665 cm^{-1} corresponding to the C=C stretching, the C=O bending peak of the ester group at 1740 cm^{-1} , and the peak at about 3000 cm^{-1} due to C-H bonds **Error: L'origine riferimento non è stata**

trovata. In the Raman spectrum of graphene, it is possible to observe the G (1580 cm^{-1}) band, which is a primary in-plane vibrational mode of carbon-carbon bonds in graphene sheets, the D (1350 cm^{-1}) band ascribed to disordered carbon in graphene and 2D (2690 cm^{-1}) band, that is a second-order overtone of D band ascribed to AB-stacked graphene **Error. L'origine riferimento non è stata trovata.** Figure 2.4 demonstrates that no dramatic change occurs in the GE spectrum when graphene nanoplatelets are assembled onto the TPU particle surface and then sintered during SLS processing. In any case, it is observed a slight decrease of I_D/I_G ratio which results 0.064 for GE powder and 0.035 for the GE in the composite realized by SLS. This variation may be tentatively ascribed to an effect of the sintering process which likely reduces the extent of defects of GE platelets assembled onto TPU powder particles (the effect of TPU in the measurements of the I_D/I_G ratio is negligible) [39].

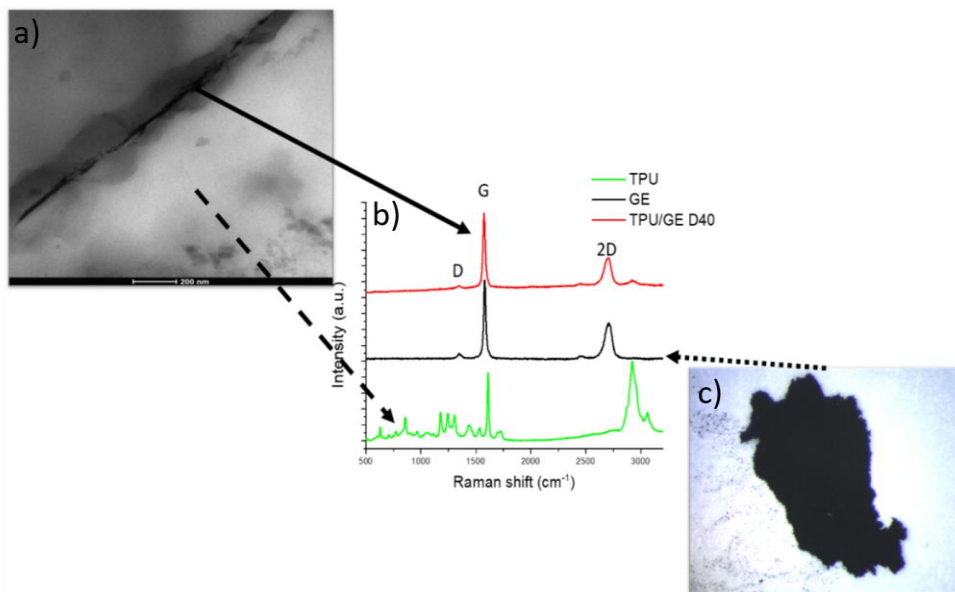


Figure 2.4. a) TEM observation, b) Raman spectra of GE powder (black line), and TPU (green line) and GE (red line) in the TPU/GE G40 composite after SLS processing, and c) GE powder.

2.3.2.1. Thermal properties

Thermal properties of SLS-fabricated TPU-based and TPU/GE porous samples were investigated by DSC and TGA. Figure 5a shows the cooling and heating DSC curves of the reference TPU porous structure. From both curves, a main thermal event is noticed, consisting in a first-order transition showing large thermal hysteresis, as indicated by the peak maximum recorded at 90 and 166 °C upon cooling and heating, respectively. This transition is related to the melt crystallization and fusion of TPU hard segment crystallites **Errore. L'origine riferimento non è stata trovata.** The calculated melting enthalpy value was as low as 5.5 J/g, indicating that only a small fraction of the material was able to crystallize [41]. In the heating thermogram, it is also worth noting the occurrence of the glass transition temperature (T_g) at -18 °C.

Figure 2.5a also reports the DSC thermogram of TPU/GE D40 as representative of the thermal behaviour of the SLS processed TPU/GE composite materials. Crystallization and melting peaks were detected at 65 and 141 °C, respectively, indicating that the addition of GE hindered TPU crystallization, also decreasing the crystalline size of the TPU fraction **Errore. L'origine riferimento non è stata trovata.** **Errore. L'origine riferimento non è stata trovata.** In addition, the value of melting enthalpy was about 5.1 J/g, showing that an even smaller amount of hard segments crystallized in comparison with the plain TPU. Finally, GE also caused a significant increase in T_g , which was detected at -11 °C in the composites. The rise in T_g shows that the presence of the carbonaceous filler was able to mediate the H-bonding interactions between TPU chains, reducing the mobility of the polymer soft segments, as already reported for graphene/TPU composites [43]. Similar results were obtained for all porous systems regardless of geometry and porosity.

GE also affected the thermal stability of the TPU foam. In Figure 2.5b the thermogravimetric curves of TPU and TPU/GE D40 are compared. TPU

degradation occurs with a two-step mechanism. The first process, attributed to the cleavage of urethane bonds of TPU **Errore. L'origine riferimento non è stata trovata.** starts at about 280 °C, with a maximum rate at 309 °C, and accounts for about 30% mass loss. The second weight loss step, related to the decomposition of soft segments of TPU, had a maximum rate at 387 °C, leading to a residual char value of 1.2%. The presence of 1 wt% GE significantly retarded the degradation onset, which occurred at about 300 °C, also shifting the degradation rate maximum at 340 °C. Therefore, the addition of GE brings about an improvement of thermal stability of TPU, as the large-area graphene sheets increase the tortuous path for the volatile products to be released, also resulting in a higher amount of residual char (8,5%) **Errore. L'origine riferimento non è stata trovata..**

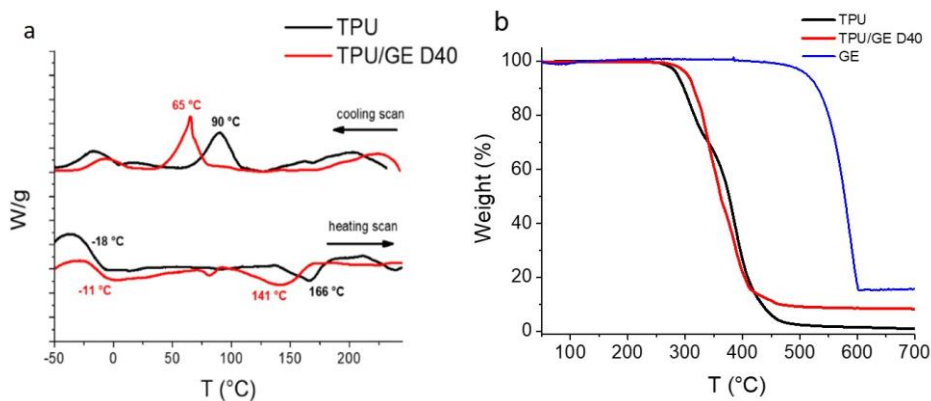


Figure 2.5. (a) DSC, and (b) TGA curves of SLS fabricated TPU, GE, and TPU/GE D40 porous structures.

2.3.3. Mechanical and piezoresistive characterization

The effect of porosity and geometry on the mechanical behavior of the TPU/GE porous structures was investigated by compression tests. Figure 2.6a shows the stress-strain curves for all investigated samples. An initial toe region, caused by a take-up of slack and alignment of the specimen, followed by a linear region can be observed. Elastic modulus was calculated from the linear region of

the curves for all the geometries considered (Figure 2.6b). In particular, the samples were tested at small strain values (<10%), in order to ensure that all samples were in their elastic deformation region. D and G architecture structures show, in the deformation range which has been investigated, a linear increase of stress with increasing strain, while the S geometry structures exhibit a progressive strengthening during compression, which results in higher stress values in comparison to the corresponding D and G structures.

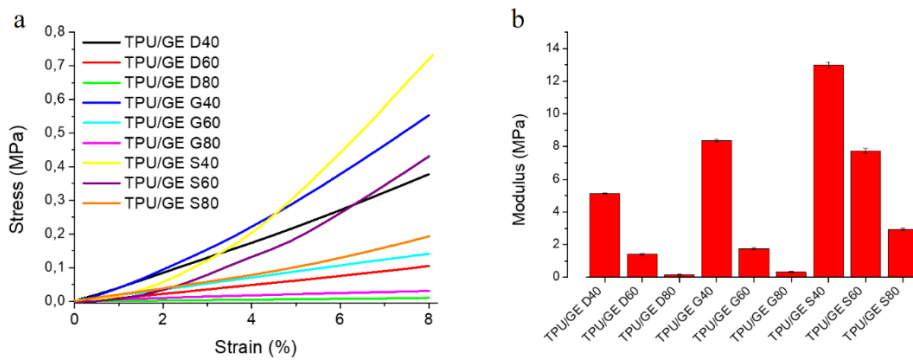


Figure 2.6. (a) Compression stress-strain curves, and (b) compression elastic modulus of the SLS fabricated TPU/GE porous structures.

This outcome is ascribed to the different morphology of pores present in the systems obtained by starting from S unit cells with respect to D and G systems. In fact, the structures with S geometry result to have less pores with bigger dimension [33-35]. This implies that, at a given porosity value, the average thickness of the trabeculae in the S structure is bigger, so the mechanical stress required to get a defined deformation is larger (as compared to other structures with same porosity). The porous structures exhibit a dramatic enhancement of the elastic compression modulus (more than 2 orders of magnitude in the case of D and G structures) when the porosity decreases from 80 to 40%. Moreover, unit cells (i.e. S, D or G) also affected the mechanical performance of the porous structures, being the S structures significantly stiffer than the corresponding G and D-based structures.

All SLS fabricated structures, except for TPU/GE D80, which gave no reliable results, were tested as concerning their electrical conductivity. Indeed, in the presence of graphene, the insulating polymer matrix turned to be conductive, due to the formation of a segregated percolated graphene network at the boundary of the TPU particles. While neat TPU displayed a conductivity value of 10^{-13} S/m, all the porous structures exhibited values ranging from 7×10^{-5} (TPU/GE S80) to 9×10^{-4} S/m (TPU/GE G80). These conductivities are comparable with those reported in literature for graphene/TPU foams fabricated by thermal induced phase separation [41]**Errore. L'origine riferimento non è stata trovata.**, indicating the formation of a stable graphene conductive network in all samples. Furthermore, the conductivity does not depend on porosity nor geometry.

The piezoresistive behaviour of the porous TPU/GE porous structures was studied by submitting the samples to compression cycles with strain up to 8%. Figure 2.7 shows the results characterizing the piezoresistive behaviour of the D, G and S-based structures with 40% porosity. All samples showed a negative piezoresistive behaviour that is the electrical resistance decreases with increasing the strain.

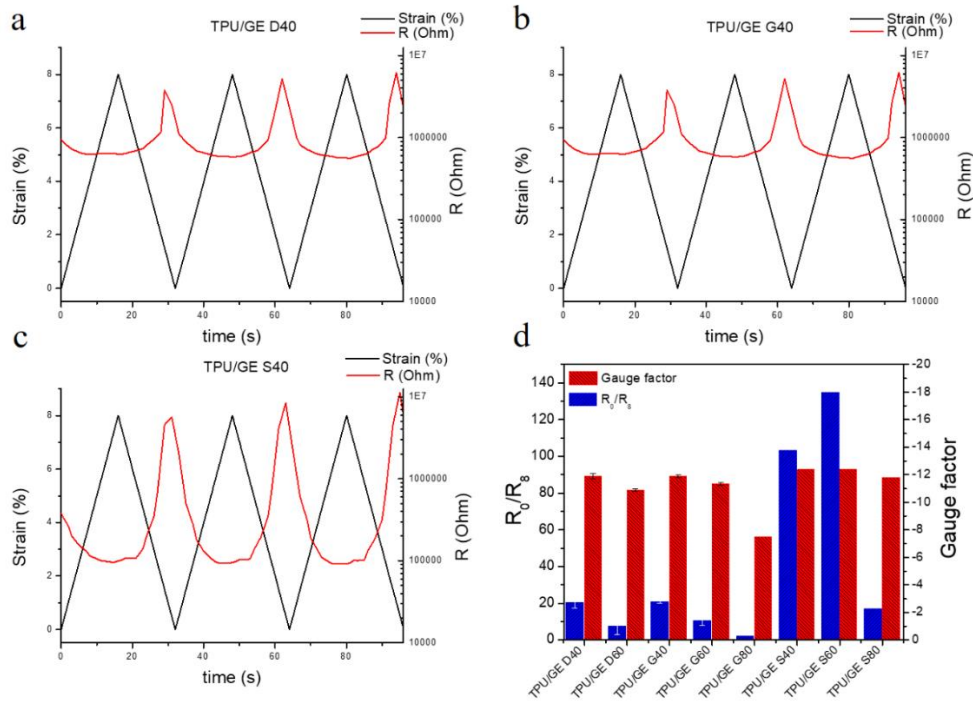


Figure 2.7. Piezoresistive behaviour of (a) TPU/GE D40, (b) TPU/GE G40, and (c) TPU/GE S40 under cyclic compression. (d) Resistance ratio and gauge factor of TPU/GE porous structures at 8% compression strain.

This outcome arises from the compactness of TPU particles and the enhancement of the GE nanoplatelets contacts upon compression, which leads to the formation of more conductive pathways **Errore. L'origine riferimento non è stata trovata.** Furthermore, it is noticed that the drop of resistance at 8% of strain depends on sample porosity and geometry. In particular, for D and G-based geometries, the resistance ratio went from 2, in the case of the D80 structure, to 20 for the less porous TPU/GE D40 and G40 structures (Figure 7a, b). More significantly, the S systems showed even larger resistance variations under compression, as a two-order of magnitude drop was recorded in the case of TPU/GE S40 and TPU/GE S60 (Figure 7c, d). The compression sensitivity of the several porous structures was evaluated by measuring the gauge factor (GF) at 8% strain (Figure 7d). All samples displayed GF absolute values above 6, with TPU/GE S40 and TPU/GE S60 displaying a value of 12.4. This difference is

ascribed to the peculiar shape of the S unit cell which leads to 3D structures with bigger trabeculae which under deformation give rise to the building up of more effective conductive pathways. To the best of our knowledge, such high values have never been reported for graphene-based polymer porous structures when subjected to compressive strain **Errore. L'origine riferimento non è stata trovata.** It has to be pointed out that GF values are even higher for deformation extents lower than 8%, then tend to plateau as the maximum strain value is approached (Figure 2.8). Indeed, most samples displayed GF absolute values ranging from 60 to 20 for deformations extents from 1 to 5%.

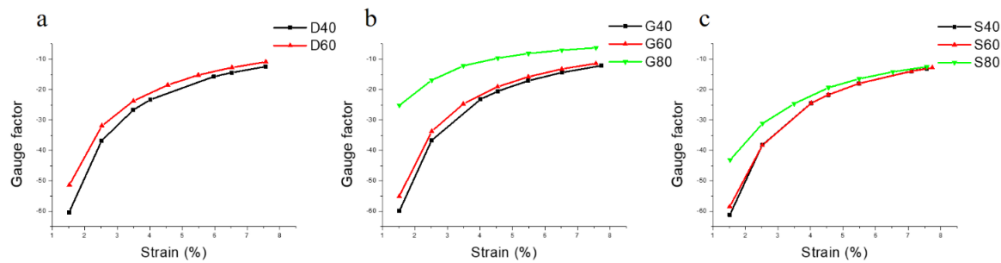


Figure 2.8. Variation of gauge factor as a function of compression strain for the TPU/GE porous structures with: (a) Diamond, (b) Gyroid, and (c) Schwarz unit cells.

It is also worth noting that for all porous structures GF increases by reducing the porosity, at a fixed strain. This confirms that a key role is played by the dimension of the trabeculae. The bigger the size of trabeculae, and consequently the larger the number of wrapped TPU particles which can be compacted, the larger the GF.

The outstanding sensitivity of the SLS fabricated structures demonstrates that they can be used as piezoresistors in the detection of very small deformations (i.e. strain less than 5%). All the SLS fabricated TPU/GE structures were also characterized in terms of electromechanical cycling stability. The samples were submitted to 50 consecutive compressive cycles (at 8% of strain), as reported in Figure 2.9a for TPU/GE S40. In the cyclic compression process, both mechanical

and electrical response of the sample were stable all over the experiment, demonstrating excellent stability and signal reversibility. Figure 2.9b summarizes the results of the electromechanical cycling tests for all porous structures. The resistance values at 8% strain reported as a function of time clearly demonstrate that, regardless of porosity and geometry, after the very first compression cycles all structures exhibited excellent stability and repeatability.

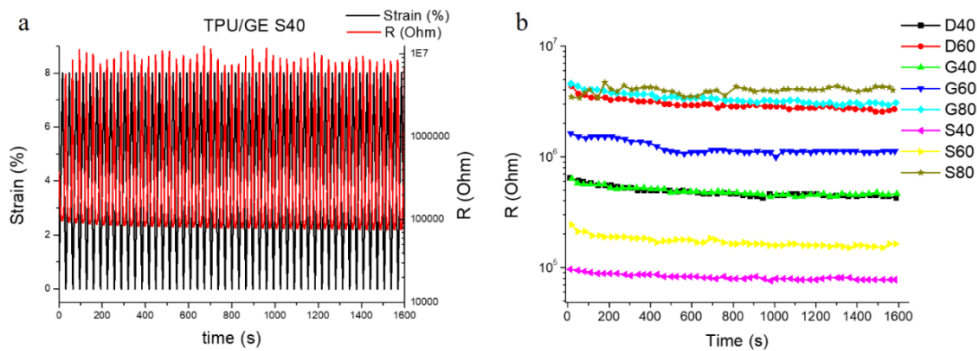


Figure 2.9. (a) Piezoresistive behaviour of TPU/GE S40 over 50-cycle compression test, and (b) resistance values at 8% strain as a function of time for all TPU/GE composite structures.

2.3.4. Thermal conductivity

The thermal conductivity (λ) of TPU/GE porous structures was examined, to gain insight on the effect of porosity and geometry on their thermal behavior. Figure 2.10 shows that λ is strongly affected by the porosity of the structure, making possible to tune the thermal conductivity of the TPU/GE composites by modifying the overall porosity.

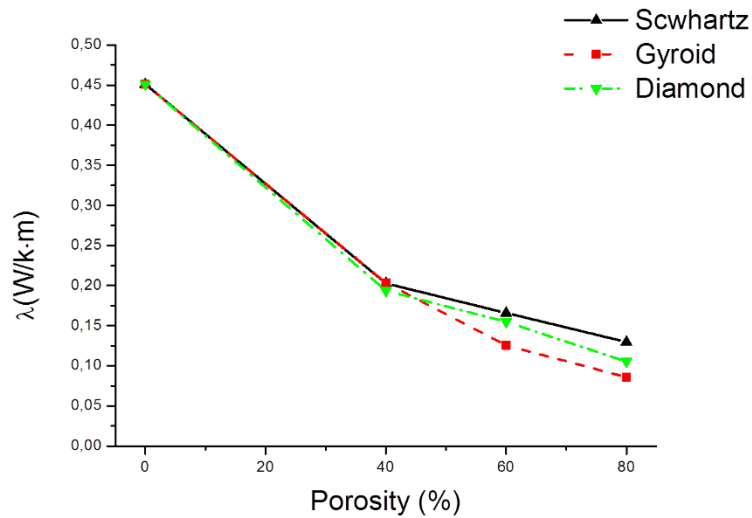


Figure 2.10. Effect of porosity and geometry on the effective thermal conductivity of TPU/GE porous structures.

Obviously, λ decreases as the porosity increases, going from 0.451 W/m·K for the bulk material down to 0.086 W/m·K for the Gyroid structure with 80% porosity. It was ascertained that an increase in porosity is linked to a decrease in the trabeculae size and an increase of pore dimension for a given unit cell **Errore. L'origine riferimento non è stata trovata..** On the other hand, results obtained for the three different architectures (D, G, and S) indicate that the effect of geometry on the thermal conductivity is small if compared with the effect on the electrical properties and piezoresistivity. This confirms that the transfer of heat phonon and electrons are subject to different physical laws. However, the thermal conductivity remained similar for the different geometries until 40% of porosity. Above this value, the Schwarz geometry showed the highest λ values, while the Gyroid displayed the lowest values, both at 60 and 80% porosity. This effect is again ascribed to the different size of trabeculae generated by the D, G, and S unit cell architectures.

2.4. Conclusions

Electrically conductive TPU/GE porous structures were successfully fabricated by SLS processing by using a home-made powder realized by wrapping GE nanoplatelets onto TPU particles. Several 3D mathematically defined architectures with different porosity extents were designed and realized, namely Gyroid, Diamond and Schwarz. Electrical and thermal conductivity, mechanical strength, filler dispersion and interaction with the polymer matrix of the TPU/GE porous systems were investigated and correlated with their porosity and internal architecture.

Morphological characterization clearly indicated that SLS manufacturing is suitable to create porous structures with narrow pore size distributions and high pore interconnectivity. Moreover, upon processing the GE sheets remain entrapped in between the interparticle boundaries, thereby forming a segregated conductive network fully percolating the porous structure. GE hindered crystallization of TPU hard segments, but reduced the mobility of the polymer soft segments, increasing the T_g . Furthermore, GE brought about an improvement of thermal stability of TPU. Compression tests revealed that S geometry provides the porous structure with higher elastic modulus in comparison to the corresponding D and G geometries.

All architectures showed electrical conductivity as well as negative piezoresistive behaviour during cyclic compression tests, characterized by outstanding GF absolute values. In particular, S geometry structures yielded GF values of 12.4 at 8% strain, due to the combination of GE network segregation and higher size of trabeculae connecting the porosity. GF absolute values ranging from 60 to 20 were observed for deformations extents from 1 to 5%, demonstrating that the SLS-processed porous systems can be used in the detection of strains lower than 5%. Upon cyclic piezoresistive sensing tests, all samples exhibited excellent behaviour repeatability, regardless of their porosity and geometry. Thermal conductivity of the TPU/GE structures significantly decreased with increasing porosity, while the effect of the structure architecture was less relevant.

The reported results demonstrate that the TPU/GE powder is a suitable material for the SLS fabrication of porous structures with highly tailored flexibility and electrical conductivity. The powder enables the obtainment of a right balance between mechanical and functional properties of the printed structures, which in turns hold great potential to be used as flexible, highly sensitive, and stable piezoresistive sensors in wearable or implantable devices, and dielectric elastomer actuators.

References

- [1]. Li, Z.; Wang, Z.; Gan, X.; Fu, D.; Fei, G.; Xia, H.; Selective Laser Sintering 3D Printing: A Way to Construct 3D Electrically Conductive Segregated Network in Polymer Matrix. *Macromol. Mater. Eng.* 2017, 1700211.
- [2]. Lee, J.Y.; An, J.; Chua, C.K. Fundamentals and applications of 3D printing for novel materials. *Appl. Mater. Today.* 2017, 7, 120-133.
- [3]. Manapat, J.; Chen, Q.; Ye, P.; Advincula, R. 3D printing of polymer nanocomposites via stereolithography. *Macromolecular Materials and Engineering.* 2017G, 302(9), 1600553.
- [4]. Chen, J.; Mangadlao, J.; Wallat, A.; de Leon, J.; Pokorski, J.K.; Advincula, R. 3D printing biocompatible polyurethane/poly (lactic acid)/graphene oxide nanocomposites: anisotropic properties. *ACS Applied Materials and Interfaces.* 2017, 9(4), 4015-4023.
- [5]. Lam, C.; Mo, X.; Teoh, S.; Hutcmacher, D. Scaffold development using 3D printing with a starch-based polymer. 2002, *Mater Sci Eng C*, 20, 49-56.
- [6]. Palm, W.; Rapid Prototyping Primer, Pennsylvania State University, University Park, Pennsylvania: The Learning Factory, 2002.
- [7]. Petzold, R.; Zeilhofer H.F.; Kalendar, W. Rapid prototyping technology in medicine—basics and applications. *Comput Med Imag Graph.* 1999, 23(5), 277-84.
- [8]. Shuai, C.; Gao, C.; Feng, P.; Peng, S. Graphene-reinforced mechanical properties of calcium silicate scaffolds by laser sintering. *RSC Advances.* 2014, 4(25), 12782-12788.

- [9]. Kruth, J. P.; Mercelis, P.; Van Vaerenbergh, J.; Froyen, L.; Rombouts, M. Binding mechanisms in selective laser sintering and selective laser melting. *Rapid prototyping journal* 2005, 11(1), 26-36.
- [10]. Kumar, S. Selective laser sintering: a qualitative and objective approach. *Jom*. 2003, 55(10), 43-47.
- [11]. Yuan, S.; Shen, F.; Bai, J.; Chua, C. K.; Wei, J.; Zhou, K. 3D soft auxetic lattice structures fabricated by selective laser sintering: TPU powder evaluation and process optimization. *Materials & Design*. 2017, 120, 317-327.
- [12]. Shi, Y.; Wang, Y.; Chen, J.; Huang, S.. Experimental investigation into the selective laser sintering of high impact polystyrene. *Journal of applied polymer science*, 2008, 108(1), 535-540.
- [13]. Ho, H.C.H.; Gibson, I.; Cheung, W.L. Effects of energy density on morphology and properties of selective laser sintered polycarbonate. *Journal of Materials Processing Technology*, 1999, 89, 204-210.
- [14]. Dadbakhsh, S.; Verbelen, L.; Tom, V.; Strobbe, D.; Van Puyvelde, P.; Kruth, J.P. Effect of powder size and shape on the SLS processability and mechanical properties of a TPU elastomer. *Physics Procedia*. 2016, 83, 971-980.
- [15]. Yuan, S.; Zheng, Y.; Chua, CK.; Yan, Q.; Zhou, K.; Electrical and thermal conductivities of MWCNT/polymer composites fabricated by selective laser sintering. *Composites Part A: Applied Science and Manufacturing*. 2018, 105, 203-213.
- [16]. Wang, X.; Jiang, M.; Zhou, Z.; Gou, J.; Hui, D. 3D printing of polymer matrix composites: A review and prospective. *Composites Part B: Engineering*, 2017, 110, 442-458.]

- [17]. Reza, R.; Naguib, H. Porosity and composition dependence on electrical and piezoresistive properties of thermoplastic polyurethane nanocomposites. *Journal of Materials Research*. 2013, 28(17), 2415-2425.
- [18]. Zhang, X.W.; Pan, Y.; Zheng, Q.; Yi, X.S. Time dependence of piezoresistance for the conductor-filled polymer composites. *J Polym Sci Part B: Polym Phys*. 2000, 38(21):2739-49.
- [19]. Wang, L.; Ding, T.; Wang, P. Thin flexible pressure sensor array based on carbon black/silicone rubber nanocomposite. *IEEE Sensors Journal* 2009, 9(9), 1130-1135.
- [20]. Tao, J.; Liu, N.; Ma, W.; Ding, L.; Li, L.; Su, J.; Gao, Y. Solid-state high performance flexible supercapacitors based on polypyrrole-MnO₂-carbon fiber hybrid structure. *Scientific reports* 2013, 3, 2286.
- [21]. Park, S.; Vosguerichian, M.; Bao, Z. A review of fabrication and applications of carbon nanotube film-based flexible electronics. *Nanoscale* 2013, 5(5), 1727-1752.
- [22]. Guan, X.; Zheng, G.; Dai, K.; Liu, C.; Yan, X.; Shen, C., & Guo, Z. Carbon nanotubes-adsorbed electrospun PA66 nanofiber bundles with improved conductivity and robust flexibility. *ACS applied materials & interfaces* 2016, 8(22), 14150-14159.
- [23]. Gupta, P.; Yadav, S.K.; Agrawal, B.; Goyal, R.N. A novel graphene and conductive polymer modified pyrolytic graphite sensor for determination of propranolol in biological fluids. *Sensors and Actuators B: Chemical*, 2014, 204, 791-798.
- [24]. Chen, Z.; Ren, W.; Gao, L.; Liu, B.; Pei, S.; Cheng, H.M. Three-dimensional flexible and conductive interconnected graphene networks grown by chemical vapour deposition. *Nature materials*, 2011, 10(6), 424.

- [25]. Lee, C.; Wei, X.D.; Kysar, J.W.; Hone, J. Measurement of the elastic properties of intrinsic strength of monolayer graphene. *Science* 2008, *321*, 385–388.
- [26]. Tadakaluru, S.; Thongsuwan, W.; Singjai, P. Stretchable and flexible high-strain sensors made using carbon nanotubes and graphite films on natural rubber. *Sensors* 2014, *14*, 868.
- [27]. Wang, Z.; Nelson, J.K.; Hillborg, H.; Zhao, S.; Schadler, L.S. Graphene oxide filled nanocomposite with novel electrical and dielectric properties. *Adv Mater* 2012, *24*, 3134–7.
- [28]. Ding, P.; Su, S.; Song, N.; Tang, S.; Liu, Y.; Shi, L. Highly thermal conductive composites with polyamide-6 covalently-grafted graphene by an in situ polymerization and thermal reduction process. *Carbon* 66 2014, 576-584.
- [29]. Zhan, Y.; Lavorgna, M.; Buonocore, G.; Xia, H. Enhancing electrical conductivity of rubber composites by constructing interconnected network of self-assembled graphene with latex mixing. *J. Mater. Chem.* 2012, *22*, 10464-68.
- [30]. Koerner, H.; Price, G.; Pearce, N.A.; Alexander, M.; Vaia, R.A. Remotely actuated polymer nanocomposites—stress-recovery of carbon-nanotube-filled thermoplastic elastomers. *Nat. Mater.* 2004, *3*, 115.
- [31]. Cho, J.W.; Kim, J.W.; Jung Y.C.; Goo, N.S. Electroactive shape-memory polyurethane composites incorporating carbon nanotubes. *Macromol. Rapid Commun.* 2005, *26*, 412-16.
- [32]. Yuan, S.; Shen, F.; Bai, J.; Chua, C.K.; Wei, J.; Zhou, K. 3D soft auxetic lattice structures fabricated by selective laser sintering: TPU powder evaluation and process optimization. *Materials & Design* 2017, *120*, 317-27.

- [33]. Gandy, P.J.; Klinowski, J. Exact computation of the triply periodic G (Gyroid') minimal surface. *Chem. Phys. Lett.* 2000, 321(5-6), 363-371.
- [34]. Gandy, P. J.; Cvijović, D.; Mackay, A. L.; Klinowski, J. Exact computation of the triply periodic D (diamond') minimal surface. *Chem. Phys. Lett.* 1999, 314(5-6), 543-551.
- [35]. Shin, J.; Kim, S.; Jeong, D.; Lee, H. G.; Lee, D.; Lim, J. Y.; Kim, J. Finite element analysis of Schwarz P surface pore geometries for tissue-engineered scaffolds. *Math. Probl. Eng.* 2012, 2012.
- [36]. Baratha, K. V.; Nourry, A.; Pilard, J. F. Synthesis of NR based Polyurethanes containing phosphorylated polymers as chain extenders. *Eur. Polym. J.*, 2015, 70, 317-330.
- [37]. Castaldo, R.; Lama, G. C.; Aprea, P.; Gentile, G.; Lavorgna, M.; Ambrogio, V.; Cerruti, P. Effect of the oxidation degree on self-assembly, adsorption and barrier properties of nano-graphene. *Micropor. Mesopor. Mat.* 2018, 260, 102-115.
- [38]. Ferrari, A. C.; Meyer, J. C.; Scardaci, V.; Casiraghi, C.; Lazzeri, M.; Mauri, F.; Piscanec, S.; Jiang, D.; Novoselov, K.S.; Roth, S.; Geim, A.K. Raman spectrum of graphene and graphene layers. *Phys. Rev. Lett.* 2006, 97(18), 187401.
- [39]. Aïssa, B.; Memon, N.K.; Ali, A.; Khraisheh, M.K. Recent progress in the growth and applications of graphene as a smart material: A review. *Front. Mat.* 2015, 2, 58.
- [40]. Frick, A.; Rochman, A. Characterization of TPU-elastomers by thermal analysis (DSC). *Polym. Test.* 2004, 23(4), 413-417.
- [41]. Liu, H.; Dong, M.; Huang, W.; Gao, J.; Dai, K.; Guo, J.; Guo, Z. Lightweight conductive graphene/thermoplastic polyurethane foams with

- ultrahigh compressibility for piezoresistive sensing. *J. Mater. Chem. C.* 2017, 5(1), 73-83.
- [42]. Zhu, J.; Wei, S.; Li, Y.; Sun, L.; Haldolaarachchige, N.; Young, D. P.; Southwork, C.; Khsanov, A.; Luo, Z.; Guo, Z. Surfactant-free synthesized magnetic polypropylene nanocomposites: rheological, electrical, magnetic, and thermal properties. *Macromolecules*, 2011, 44(11), 4382-4391.
- [43]. Liu, H.; Li, Y.; Dai, K.; Zheng, G.; Liu, C.; Shen, C.; Yan, X.; Guo, Z. Electrically conductive thermoplastic elastomer nanocomposites at ultralow graphene loading levels for strain sensor applications. *J. Mater. Chem. C.* 2016, 4(1), 157-166.
- [44]. Liu, H., Huang, W., Yang, X., Dai, K., Zheng, G., Liu, C., Guo, Z. Organic vapor sensing behaviors of conductive thermoplastic polyurethane-graphene nanocomposites. *J. Mater. Chem. C.* 2016, 4(20), 4459-4469.
- [45]. Wang, X.; Hu, Y.; Song, L.; Yang, H.; Xing, W.; Lu, H. In situ polymerization of graphene nanosheets and polyurethane with enhanced mechanical and thermal properties. *J. Mater. Chem.* 2011, 21(12), 4222-4227.
- [46]. Hodlur, R.M.; Rabinal, M.K. Self assembled graphene layers on polyurethane foam as a highly pressure sensitive conducting composite. *Compos. Sci. Technol.* 2014, 90, 160-165.
- [47]. Yang, L.; Wang, R.; Song, Q.; Liu, Y.; Zhao, Q.; Shen, Y. One-pot preparation of porous piezoresistive sensor with high strain sensitivity via emulsion-templated polymerization. *Compos. Part A Appl. Sci. Manuf.* 2017, 101, 195-198.
- [48]. Wang, M.; Pan, N. Modeling and prediction of the effective thermal conductivity of random open-cell porous foams. *Int. J. Heat Mass. Transfer.* 2008, 51(5-6), 1325-1331.

Chapter 3 | On the Synergistic Effect of Multi-Walled Carbon Nanotubes and Graphene Nanoplatelets to SLS 3D-Printed Elastomeric Structures

Abstract: Elastomer-based porous structures realized by selective laser sintering (SLS) are emerging as a new class of attractive multifunctional materials. Herein, a thermoplastic polyurethane (TPU) powder for SLS was modified by 1 wt.% multi-walled carbon nanotube (MWCNTs) or a mixture of MWCNTs and graphene (GE) nanoparticles (70/30 wt/wt) in order to investigate on both the synergistic effect provided by the two conductive nanostructured carbonaceous fillers and the correlation between formulation, morphology, and final properties of SLS printed porous structures. In detail, porous structures with a porosity ranging from 20% to 60% were designed using Diamond (D) and Gyroid (G) unit cells. Results showed that the carbonaceous fillers improve the thermal stability of the elastomeric matrix. Furthermore, the TPU/1 wt.% MWCNTs-GE-based porous structures exhibit excellent electrical conductivity and mechanical strength. In particular, all porous structures exhibit a robust negative piezoresistive behavior, as demonstrated from the gauge factor (GF) values that reach values of about -13 at 8% strain. Furthermore, the G20 porous structures (20% of porosity) exhibit microwave absorption coefficients ranging from 0.70 to 0.91 in the 12–18 GHz region and close to 1 at THz frequencies (300 GHz–1 THz). Results show that the simultaneous presence of MWCNTs and GE brings a significant enhancement of specific functional properties of the porous structures, which are proposed as potential actuators with relevant electromagnetic interference (EMI) shielding properties.

Keywords: selective laser sintering; piezoresistivity; thermoplastic polyurethane (TPU), carbonaceous filler; EMI shielding

3.1. Introduction

Piezoresistivity is defined as the electrical resistance variation induced by an external mechanical stimulus [1]. Piezoresistive sensors are traditionally fabricated by metallic or inorganic semiconductor materials, but they are typically rigid, heavy, and brittle, and this limits their utilization in many fields [2]. To address these drawbacks, in recent years, porous polymer materials reinforced with conductive nanostructured fillers have been engineered as piezoresistive sensors. The goal is to obtain electrical conductive polymer composites by forming a three-dimensional interconnected conductive network made of conductive fillers. In this respect, metal nanoparticles [3], intrinsically conductive polymers [4] dispersed in polymer matrix [5], or carbonaceous fillers such as carbon black [6], carbon fibers [7], carbon nanotubes [8], graphite [9], and graphene [9] have been widely used. Flexibility, high porosity, ultra-low density, good energy conversion, and storage properties are the properties achieved by these nanocomposites [10]. Such conductive nanocomposites find a wide range of applications as pressure sensors [11] as well as flexible circuits [12], antistatic materials [13], and electromagnetic interference shielding devices [14].

However, constructing 3D interconnected conductive networks using conventional manufacturing such as in situ polycondensation [15], templating methods [16], melt processing [17], and solution mixing [18] is a challenging task, because the high shearing force present in these conventional processes breaks the conductive network structure. 3D printing is an innovative manufacturing technology that, based on Computer-Aided Design (CAD) data, can directly turn complex 3D models into real objects [19–21]. Selective laser sintering (SLS) is one of the most significant 3D printing techniques, which is applied in many fields, from biomedicine to aerospace [22]. SLS is a powder-based process in which 3D structures are obtained by the layer-by-layer sintering of thermoplastic polymer powder via a computer controlled scanning laser beam

[23]. Differently from other 3D printing techniques, such as fused deposition modelling (FDM), SLS is a shear-free and free-flowing process that, in case the raw polymeric powder is coated with conductive filler, allows the formation of a segregated filler network within the polymer matrix [24].

Thermoplastic polyurethane (TPU) is a soft and flexible elastomer widely used as building material for the SLS process [25]. Recently, TPU composites reinforced with nanoscale fillers drew great attention for their enhanced mechanical, thermal, and electrical properties [26,27]. In fact, combining a TPU matrix with conductive fillers and SLS manufacturing is a simple and effective approach to prepare nanocomposite materials with optimized thermal, anticorrosive, and electromagnetic shielding properties [11,28–30]. Xia et al., recently developed a novel approach to construct a 3D electrically conductive segregated network in TPU/CNTs composite polymer matrix by SLS [24]. Later, they reported the simultaneous realization of conductive segregation network microstructure and minimal surface porous macrostructure by SLS 3D printing of single-walled carbon nanotubes (SWCNTs)-wrapped TPU composite powder. [31] The Schwarz (S-) structure was found to be capable of producing the best piezoresistive properties of the SWCNTs/TPU composite sensor with a gauge factor (GF) much higher than that for Gyroid and Diamond structures.

In a previous research, some of the authors have manufactured TPU/1 wt.% graphene (GE) porous systems, and demonstrated the correlation between geometrical features and electrical properties of the 3D-printed porous structures. All porous structures exhibited a robust negative piezoresistive behavior, with outstanding strain sensitivity. However, the obtained results showed that GE particles obstruct the polymer powder coalescence, thereby resulting in a porous structure that exhibits an imperfect percolative network and poor mechanical properties [27]. The analysis of the literature confirms that elastomer-based porous structures realized by SLS technology with powders modified with carbonaceous fillers have been exhaustively investigated as innovative materials for piezoresistive sensors. However, in this context, a fully understanding of the

formulations–properties correlations which establish when 2D and 1D carbonaceous filler mixtures are used to modify the elastomeric-based SLS particles are still missing.

Alongside with outstanding piezoresistive behavior, the elastomer-based conductive porous structures exhibit interesting properties to be used in the field of Electromagnetic Interference Shielding. In fact, the porosity and electrical conductivity are the most important material parameters responsible for the electro-magnetic (EM) response of materials [32]. Thus, in case of high conductivity and zero porosity, like, e.g., conventional metals of valuable thickness (thicker than skin depth), electro-magnetic interference shielding efficiency (EMI SE) is high and ascribed mainly to the reflection from the topmost metal surface. For thinner than skin depth films with metallic conductivity (e.g., graphene and other carbon nm-films [33–35], high absorption close to 100% is possible in case of placing it to $\lambda/4$ dielectric plate or back reflector separated from the conductive film by a fine insulating slab (so-called Salisbury screen) [34,36].

In case of porous monoliths, even for a highly conductive backbone, in contrast to bulk metals, it is possible to reach resonant perfect electromagnetic absorption. For that, the void/cell size should be compatible with the wavelength [37].

However, for many applications, it is not necessary resonant, even perfect, absorption. Many applications, especially in the field of EMI shields, require high but not perfect broadband absorption. The simplest way is to use slightly conductive media of proper thickness in order to suppress the reflection due to constructive interference effects. However, such a solution demands a thick and heavy EMI shielding layer (e.g., epoxy filled with multi-walled carbon nanotube (MWCNT) above the percolation threshold must be not less than 10 mm thick and have a targeting frequency of 10 GHz [38,39]), and it again supports resonant absorption.

The advantage of Diamond (D) and Gyroid (G) lattices fabricated by SLS 3D printing from conductive polymer composites is the option to tune their geometrical features (porosity, void size) to target a particular frequency range. Moreover, the conductivity of the lattices skeleton has to be enough to ensure Joule heating (true absorption of electromagnetic waves), and to secure multiple reflection from the void/cell walls enhancing resultant absorption.

In this research, different types of carbonaceous fillers able to improve the electrical properties of the porous structures realized by SLS were investigated. In detail, two kinds of fillers were used to coat the TPU powders: multi-walled carbon nanotubes (MWCNTs) and a combination of MWCNTs and GE (70/30 wt/wt). MWCNTs are a low-cost filler, if compared to single-walled carbon nanotubes (SWCNTs), and SLS 3D printing induces their segregation, improving the conductive percolation network. Moreover, it has been demonstrated that the combined use of MWCNTs and GE allows the realization of nanocomposites with better electrical properties in terms of conductivity and gauge factor if compared to MWCNTs and GE alone. Nanocomposite TPU powders have been processed by SLS to obtain mathematically defined structures with different shapes and porosities. The effect of the filler, porosity, and geometry on the electrical and mechanical properties of the structures was evaluated, and a comparison with our previously reported research was conducted. Moreover, electromagnetic shielding characterization was performed on the porous structures that showed the best electrical properties.

3.2. Materials and Methods

3.2.1. Preparation of Nanocomposites Powder

The method of SLS-compatible composite powder preparation directly determines the dispersion of nanofillers in the polymer matrix, and this affects the structural and functional properties of the SLS-printed structures. MWCNTs (NANOCYL 7000, Nanocyl, Sambreville, Belgium) and Graphene (The Sixth

Element Materials, Changzhou, China) with a MWCNTs/GE ratio of 70/30 wt/wt. were first pre-dispersed by a wet ball milling process as previously described [31]. The ball mill jars were fixed on the planetary mill and then milled continuously for 1 h at a speed of 300 rpm due to the action of iron balls in the milling jars. Anhydrous ethanol was then added to the dark dispersion and the solution was sonicated (40 W for 1 h) to obtain a stable MWCNTs-GE dispersion. The TPU powders (Mophene3D T90A, Nanjing, China) were then added to the MWCNTs-GE suspension, in such an amount to obtain a final filler content of 1 wt.%, and subjected to mechanical stirring for 2 h. The resulting mixture was filtered with a Buchner funnel under reduced pressure and dried in a vacuum oven at 70 °C for 24 h. Afterwards, the TPU/MWCNTs-GE powders were sieved to remove particles with a size over 150 µm, and silica powder was added to further improve the powder flowability. For a comparative experiment, the control sample TPU/GE composite powder (Mophene3D CT90A, Nanjing, China) was used as received.

3.2.2. Porous Structures Design and Manufacturing by SLS Technology

To design 3D porous structures, a mathematical approach was used starting from triply periodic minimal surfaces equations (TPMS). TPMS are minimal surfaces periodic in three independent directions, extending infinitely and, in the absence of self-intersections, partitioning the space into two labyrinths. The Wolfram Mathematica software was used to generate the 3D structure based on Gyroid (G) and Diamond (D) equations with different porosity. The following trigonometric equations, i.e., Equation (3.1) for G and Equation (3.2) for D structures, were used with boundary condition $x, y, z = [-3\pi; 3\pi]$:

$$\cos(x) \cdot \sin(y) + \cos(y) \cdot \sin(z) + \cos(z) \cdot \sin(x) = C, \quad (3.1)$$

$$\begin{aligned} \sin(x) \cdot \sin(y) \cdot \sin(z) + \sin(x) \cdot \cos(y) \cdot \cos(z) + \cos(x) \cdot \sin(y) \cdot \\ \cos(z) + \cos(x) \cdot \cos(y) \cdot \sin(z) = C, \end{aligned} \quad (3.2)$$

where C is the offset parameter and controls the porosity of the structures. Porous structures with three different porosities (20%, 40%, and 60%) were designed to study the correlation between porosity and electrical properties. Hereinafter, Gyroid and Diamond porous structures will be labelled as G_x and D_x , respectively, where G and D represent the geometry and x represents the porosity in %. As an example, G_{20} stands for Gyroid architectures with 20% porosity. The CAD model of the specimen was generated using the Rhinoceros CAD software (Robert McNeel & Associates, Washington, U.S.A.), and exported in the STL format for uploading into the SLS machine. The SLS process was performed on a lab-scale SLS equipment (Sharebot-SnowWhite, Lecco, Italy). The optimized sintering process parameters for TPU/MWCNTs and TPU/(MWCNTs-GE) are shown in Table 3.1. To process the nanocomposite powder, the laser was set at 40% of the maximum energy.

Table 3.1. Sintering parameters adopted to process the nanocomposite powders (thermoplastic polyurethane (TPU)/multi-walled carbon nanotubes (MWCNTs) and TPU/(MWCNTs-graphene (GE)))

Process Parameters	Value
Laser power (W)	14
Laser scan spacing (◉m)	200
Laser scan speed (pps)	40,000
Part bed temperature (◉C)	85
Outline laser power (W)	5.6
Layer thickness (◉m)	100

The manufactured structures were allowed to cool down inside the machine process chamber for approximately 1 h and then they were removed from the part bed. Excess of powder surrounding the structure and non-sintered powder from the interstices were removed by compressed air.

Examples of D and G architectures with 60% porosity, starting from the CAD unit cell, the 3D structure and, finally, a picture of the 3D-printed samples are shown in Figure 3.1.

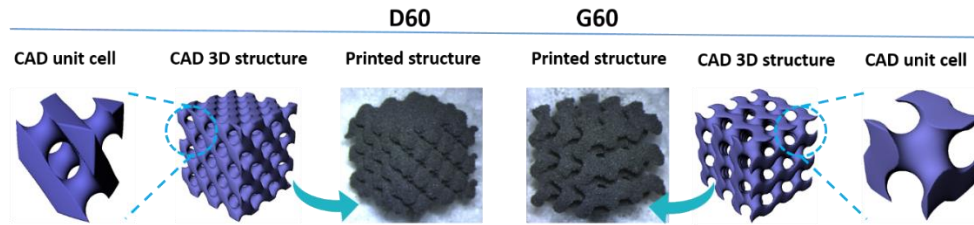


Figure 3.1. Computer-Aided Design (CAD) unit cell, CAD 3D structure, and printed for D60 and G60 systems.

3.2.3. Electron Microscopy

Scanning electron microscopy (SEM) observations were performed by a Fei Quanta 200 SEM (Hillsboro, OR, USA) to study the morphology of the porous structures. The samples were fixed on a support and metallized with a gold-palladium alloy to ensure better conductivity and prevent the formation of electrostatic charges. Transmission electron microscopy (TEM) imaging was performed using a Tecnai G2 Spirit TWIN electron microscope (FEI, Hillsboro, OR, USA) operating at 120 kV on thin sections obtained from the bulk samples using a Leica EM UC7 ultracryomicrotome (Leica Microsystems Srl, Milano, Italy) at $-100\text{ }^{\circ}\text{C}$, cut rate between 1 and 8 mm/s, and nominal feed 140 nm.

3.2.4. Thermal Characterization

Thermal properties of SLS-printed samples were measured by thermogravimetric analysis (TGA) using a PerkinElmer Pyris Diamond TG/DTA. Approximately 8 mg of sample were first heated to $90\text{ }^{\circ}\text{C}$ at $10\text{ }^{\circ}\text{C}/\text{min}$, kept in isothermal conditions for 10 min, and then heated to $800\text{ }^{\circ}\text{C}$ at a heating rate of $5\text{ }^{\circ}\text{C}/\text{min}$ under nitrogen atmosphere.

3.2.5. Piezoresistive Measurements

The experimental setup for the evaluation of the mechanical and piezoresistive properties of the 3D-printed porous structures consisted in a mechanical tester (Instron 5564 dynamometer, Torino, Italy) and a multimeter (Agilent 34401A 6½ Digit Multimeter, Santa Clara, U.S.A.) controlled by a homemade LabVIEW program. The multimeter was set up with the 2-probe measurement method, able to continuously monitor the change in the electrical resistance of the specimen submitted to loading and unloading cycles. The top and bottom surfaces of the cubic specimens ($10 \times 10 \times 10 \text{ mm}^3$) were covered with copper conductive tape as electrode. In detail, the electrical resistance changes were evaluated by submitting the samples at room temperature ($25 \text{ }^\circ\text{C}$) to cyclic loading/unloading, with 8% deformation and 3 mm/min actuation rate.

3.2.6. Electromagnetic Shielding

3.2.6.1. Low-Frequency Range

The low-frequency conductivity of G20 and G60 structures made of TPU/MWCNT and TPU/(MWCNT-GE) powders was investigated in a 100 kHz-1 MHz range in order to ensure the existence of percolation in composites. Measurements were conducted by a HP4284A LCR-meter (Zurich Instruments, Cambridge, U.S.A.). Specimens of approximate $\sim 5 \times 5 \times 3 \text{ mm}^3$ dimensions were placed between two parallel electrodes and measured as quasi-bulk samples. The LCR-meter measures the values of capacity and loss tangent, which allows calculating the conductivity.

3.2.6.2. Microwave Range

The electromagnetic response of structures G20 and G60 (cubic samples) containing MWCNTs and MWCNTs-GE was investigated in Ku-band (12–18 GHz) using a Micran R4M (Micran, Tomsk, Russia) vector analyzer and rectangular waveguide transmission line with cross-sectional dimensions of $16 \times$

8 mm². Plain-parallel samples of 10.6 mm thickness were placed into the waveguide and their complex S_{21} -parameters (being square root of sample transmission) were measured. The complex permittivity value was calculated from the experimental data by standard methods [40].

3.2.6.3. THz Range

The electromagnetic response in the terahertz frequencies was measured by the time-domain spectrometer “T-Spec” by EKSPLA (Vilnius, Lithuania). The measurement procedure has been described in detail elsewhere [41]. Two millimeters thick plane-parallel slices of porous structure ($7 \times 5 \text{ cm}^2$) were placed between emitter and detector normally to the incident EM wave. The THz detector output is proportional to the instant electrical field strength of the THz pulse during the ultrashort pumping pulse. The Fourier transform of the waveform of electrical field of THz radiation gives the frequency dependence of complex transmission and reflection coefficients. The measurements were done in both transmission and reflection modes. The absorption coefficient, A , was calculated as $A = 1 - T - R$, where T and R are the transmission and reflection coefficients, respectively.

3.3. Results and Discussion

3.3.1. Morphological Characterization of the Porous Structures

SEM and TEM analysis of the porous structures (Figure 3.2) demonstrated that MWCNTs and GE sheets were segregated between the TPU particle boundaries, forming a percolated conductive network. Figure 3.2a,d reports the SEM images of TPU/MWCNTs D60 and G60 porous structures at low magnification. It is possible to see the differences in pore structures and thickness of internal trabeculae of D and G geometries as obtained by the SLS process. In particular, it is quite evident that the trabeculae of the G geometry are bigger than the trabeculae of the D geometry (about 30% bigger, as also discussed later in the

paper). Indeed, the sintering of the TPU nanocomposite particles results in the formation of a continuous filler path spanning within the polymer matrix [24]. More specifically, SEM images (Figure 3.2b,e) clearly demonstrate that the surface of the TPU particles are covered with MWCNTs and GE filler particles. TEM pictures (Figure 3.2c,f) illustrate the formation of the percolated network due to the filler confinement between the sintered TPU particles, with a thread thickness ranging from 200 to 500 nm. It is worth noting that in the sample TPU/(MWCNTs-GE) G40, it is possible to observe that both fillers (MWCNTs and GE) were trapped between the polymer particles, forming a stable percolative network with a low filler concentration (i.e., 1 wt.%).

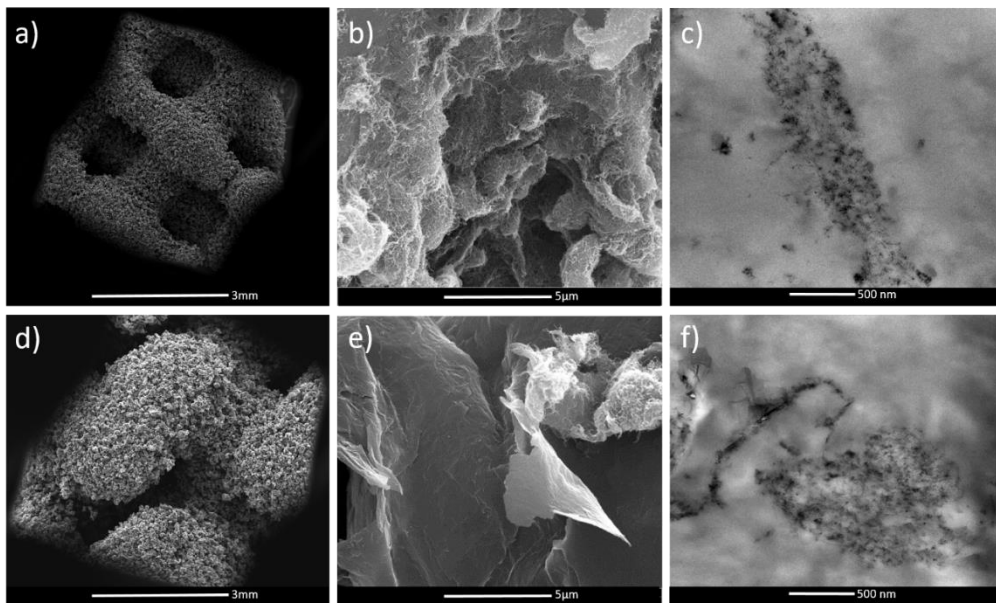


Figure 3.2. SEM of TPU/MWCNTs D60 and G60 samples at 50× magnification (a,d), SEM (b) and TEM (c) images of TPU/MWCNTs G60, and SEM (e) and TEM (f) images of TPU/(MWCNTs-GE) G60 porous structures.

3.3.2. Thermal Properties

Thermal characterization of TPU-based samples was performed by TGA analysis. The thermogravimetric curves of TPU-based samples are compared in

Figure 3.3. TPU degradation occurs in two steps as already described in our previous research [27]. Briefly, the first degradation that starts at about 280 °C is attributed to the cleavage of urethane bonds of TPU [42] and shows a maximum rate at 309 °C, accounting for about 30% mass loss. The second weight loss, with a maximum rate at 387 °C, is related to the decomposition of soft segments of TPU leading to a residual char value of 1.2%. The presence of the MWCNTs filler affects both the degradation onset, which occurred at about 300 °C, and the degradation rate maximum, which shifted to 340 °C. For the mixed system TPU/(MWCNTs GE), a dramatically different degradation curve was recorded with respect to the pristine TPU.

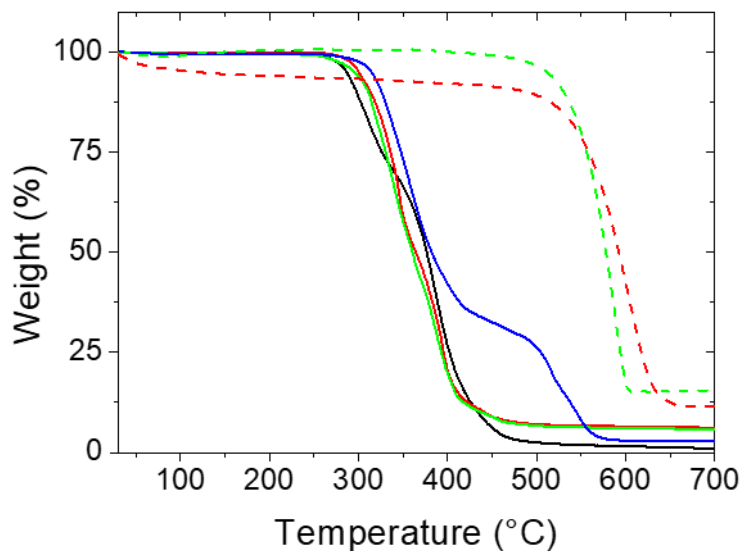


Figure 3.3. Thermogravimetric analysis (TGA) of TPU (black), TPU/MWCNTs (red), TPU/(MWCNTs-GE) (blue), MWCNTs powder (red dashed), and GE powder (green dashed).

The first degradation step started at around 310 °C, followed by a second degradation step at 488 °C. Therefore, the addition of fillers brings about an improvement of thermal stability of TPU, in particular, there is a synergistic effect of the CNTs and GE in the system with mixed fillers [43].

3.3.3. Mechanical and Piezoresistive Characterization

Compression tests were performed to study the effects of porosity and geometry on the mechanical behavior of the 3D porous structures. The samples were tested at small strain values ($<10\%$) in order to consider the behavior in the linear elastic region. The values of elastic modulus are reported in Figure 3.4.

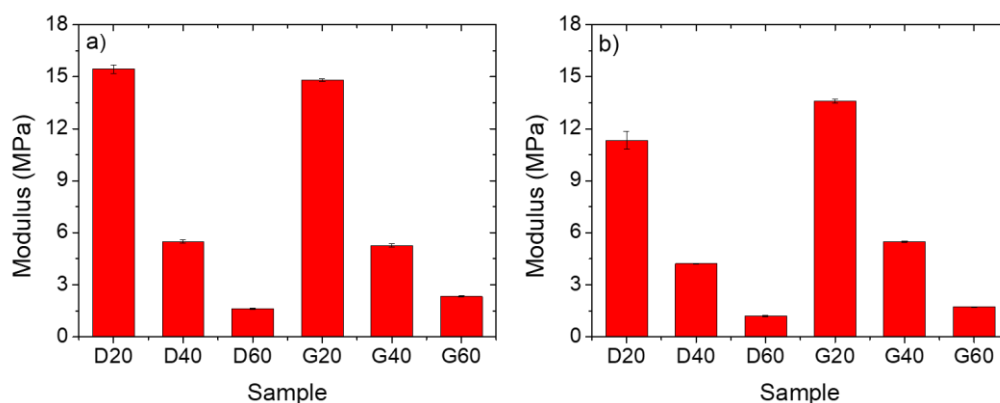


Figure 3.4. Compression elastic modulus of the selective laser sintering (SLS)-fabricated TPU/MWCNTs (a), and TPU/(MWCNTs-GE) (b) porous structures.

The average thickness of the trabeculae for TPU/MWCNTs and TPU/(MWCNTs-GE) systems with comparable geometry is similar, and this explains the comparable results above all for the systems with G unit cell geometry. As expected, raising the percentage of porosity causes the elastic modulus to strongly decrease, going, for the systems containing MWCNTs, from 15 MPa of the D20 to the 1.5 MPa of the D60. This is easily understandable by thinking that structures with higher porosity are characterized by thinner internal trabeculae, and this in turn strongly affects the mechanical response [31]. Moreover, it can be assessed that the type of filler seems to influence the mechanical response of the samples. In fact, the MWCNTs-based systems show better mechanical properties if compared to the MWCNTs/GE-based ones. This can be ascribed to the presence of GE nanosheets on the TPU particle surface that prevent the coalescence of the particle during the sintering process, thereby

reducing the mechanical properties of the porous structure. This was confirmed also by comparing the mechanical properties of the proposed systems with the TPU/GE systems that we reported in a previous paper, where for the D60 system the elastic modulus value was 1.4 MPa [27].

The piezoresistive behavior of the 3D-printed porous structures was studied by submitting the samples to strain-controlled compression cycles with a maximum strain of 8%. Alongside with the mechanical response, the electrical resistance (R) of the structures was measured as a function of the compressive strain. The samples were submitted to 50 compressive cycles and the results of the TPU/MWCNTs systems with 60% of porosity are reported in Figure 3.5. By comparing the data shown in Figure 3.5a,b, it is possible to assess the effect of the geometry for the systems with the same formulation. The R values are similar, but the variation of the electrical resistance, ΔR , as consequence of the mechanical compression, is larger for the sample with G geometry. In the cyclic compression process, the mechanical response of the sample was very stable, whereas the electrical response presented some slight instability (which could also be ascribed to the electrical contact between the sample and the electrode) all over the experiment. However, the results confirmed the signal reversibility, with a direct correlation between the strain and the electrical resistance, that decreased by increasing the compression strain.

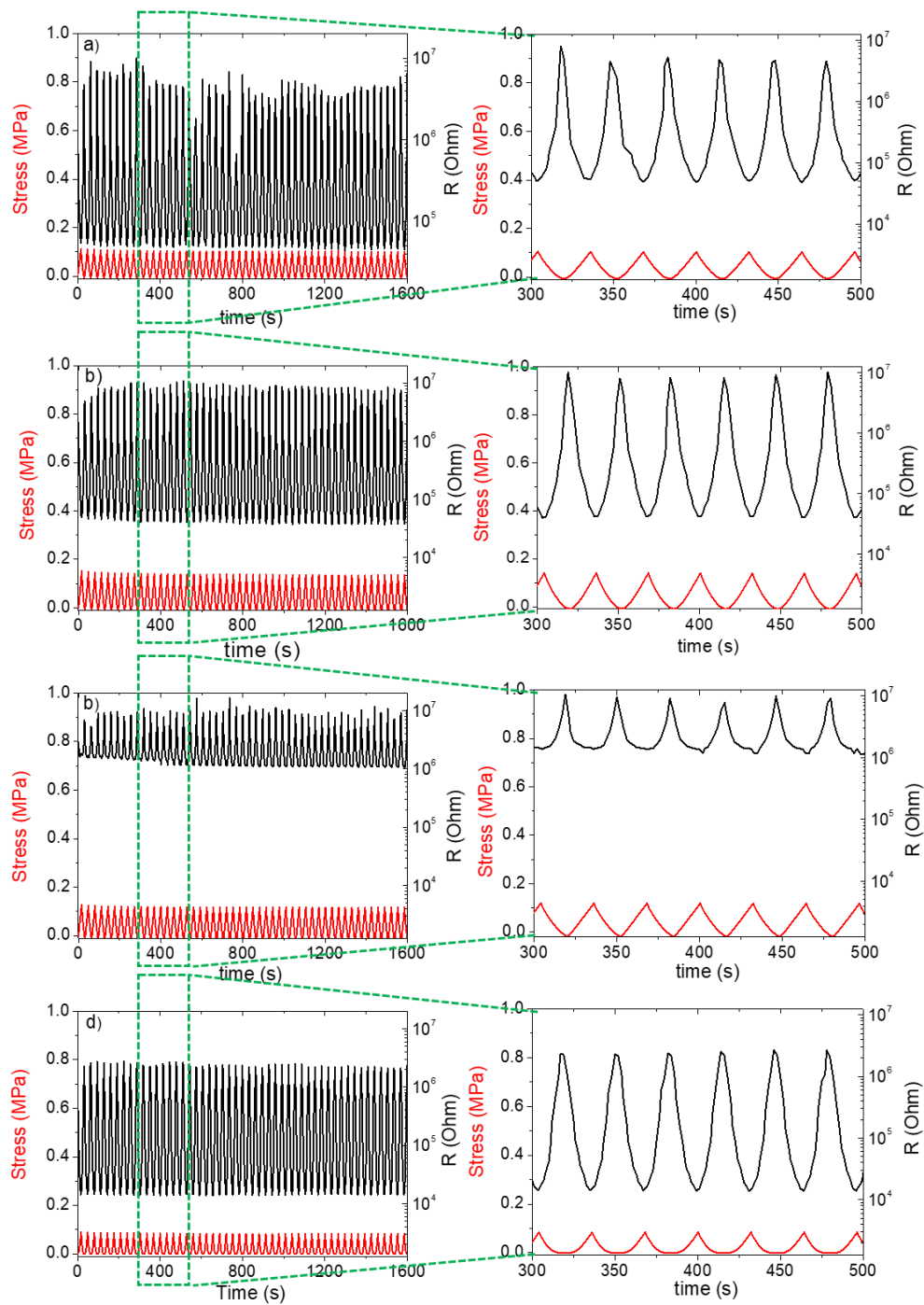


Figure 3.5. Piezoresistive behavior in terms of variation of compression stress and electrical resistance for the systems of (a) TPU/MWCNTs with D geometry, (b) TPU/MWCNTs, (c) TPU/GE, and (d) TPU/(MWCNTs-GE) with G geometry. All systems have 60% porosity and are submitted to compression loading/unloading cycles of up to 8% strain.

A direct comparison between the effects of different fillers on the piezoresistive behavior of printed samples with the same geometry and porosity is useful to give evidence of a possible synergistic effect. For sake of comparison, in this context, it has been considered important to present also the results related to the systems realized with GE nanoplatelets that were the object of a previous paper [27]. Electrical resistance of the TPU/GE system, after compression at 8% strain (Figure 3.5c), was higher than that of the MWCNTs system (Figure 3.5b). This behavior is in agreement with the literature data and the lower conductivity of GE-based composites as compared with the MWCNTs composites [44,45].

Moreover, it was possible to observe a synergistic effect of the fillers in the TPU/(MWCNTs-GE) system (Figure 3.5d). In fact, the resistance values for the TPU/(MWCNTs-GE) system at 0% and 8% strain were lower than those of the TPU/MWCNTs composite. This can be ascribed to the formation of more conductive pathways [46]. Furthermore, as it was expected, the resistance at 8% strain depends on sample porosity and geometry (see Figure 3.6) resulting larger for the systems with higher porosity (more details are provided later). Finally, the electrical resistance does not change during loading/unloading cycles as consequence of the satisfying robustness and stability of the porous structures.

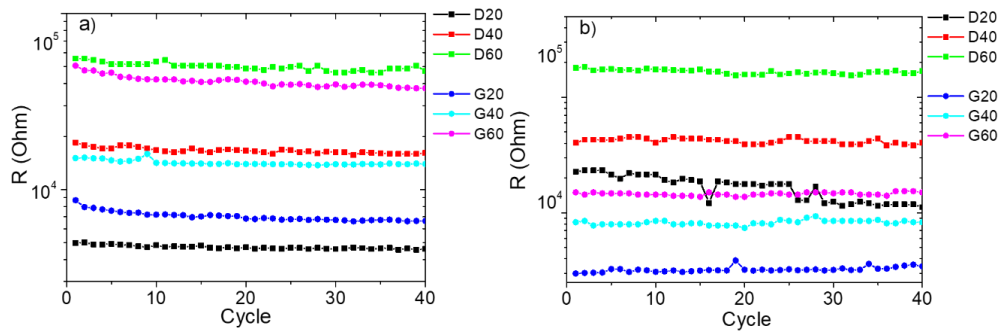


Figure 3.6. Resistance values at 8% strain for TPU/MWCNTs (a) and TPU/(MWCNTs-GE) (b) porous structures during the compression loading/unloading cycles.

It is worth noting that for the TPU/(MWCNTs-GE) composite, the systems with Gyroid structures showed significantly lower electrical resistance when subjected to compressive strain. This can be ascribed to the different internal structures of D60 and G60 samples. As shown in Figure 3.7, the cross-section area of G60 present thicker trabeculae if compared with D60 geometries (as also confirmed by SEM images reported in Figure 3.2. In fact, the average thickness of the G60 structure trabeculae is 1.360 ± 0.001 mm, which is 30% higher compared with the thickness of the D60 structure (equal to 1.040 ± 0.001 mm). This means that in the G60 structure, during compression loadings, the fillers create more effective percolating networks by forming more MWCNTs and GE nanoplatelets contacts.

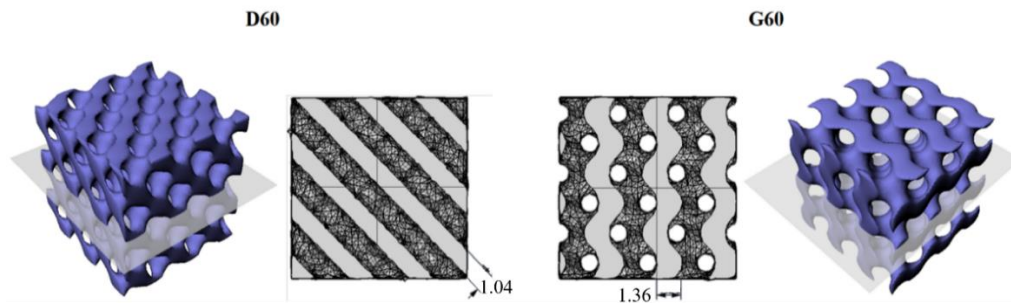


Figure 3.7. Cross-section areas and thickness of trabeculae for D60 and G60 structures.

To compare our results with those found in literature, it is worth noting that the average $\Delta R/R_0$ value measured for our systems is equal to 99.4% with a compression strain of 8%. Kang et al., measured a $\Delta R/R_0$ equal to 0.8% for a pressure of 5 MPa for systems consisting of single-wall-carbon nanotube/Polyimide, which is one order of magnitude higher compared with the compression stress applied in this research (i.e., about 0.2 MPa as shown in Figures 5 and 6) [47]. Similarly, a value of $\Delta R/R_0 \approx 15\%$, that is still lower as compared to the one shown by the systems investigated in this paper, at similar deformation ($\epsilon \approx 8\text{--}10\%$) was reported by Ku-Herrera et al. for poly (vinyl ester)

filled with 0.3 wt.% of multi-wall carbon nanotubes (PVE-MWCNT) [48]. Bao et al., found that PDMS-SWCNT materials could have a resolution of minimum detectable stress in compression of 50 KPa and report a $\Delta R/R_0$ value of 8% for a strain of 50% [49]. Similar results are reported for a system of poly(isoprene)-reduced graphene oxide PI-RGO [50]. The comparisons with the above-mentioned systems allows us to conclude that the approach exploited in this paper, which combines nanocomposite powder and SLS printing technology, reveals that nanocomposite sensors are extremely sensitive to deformation, with a reproducible and stable piezoelectric behavior.

In order to gain a deeper understanding of the effect of geometry, SLS printing technology, printing resolution, and formulations on the electrical resistance of the considered systems, the resistivity of materials was calculated by taking into account the porosity and the measured resistance values at 0% strain. The calculations were performed by relating the measured electrical resistance only to the bulk materials, and considering the porosity as the empty fraction volume of the total volume of samples submitted to the electrical characterization, following the model developed by Montes et al. [51]. They analyzed the problem of the electrical conduction in powdered systems and proposed an equation for computing the effective electrical resistivity of sintered aggregates (Equation (3.3)).

$$\rho = R \cdot \left(\frac{S}{l}\right) \cdot \sqrt{(1 - \theta)^3} \quad (3.3)$$

where ρ is the resistivity of the porous system, R is the calculated resistance of the porous system, S is the contact surface between electrode and sample (in this case correspond with the surface of the sample), l is the distance between the electrodes (in this case correspond with the side of the sample), and θ is the porosity values.

Figure 3.8 shows the resistivity values for the TPU/MWCNTs and TPU/(MWCNTs-GE) systems, calculated accordingly with Equation (3.3).

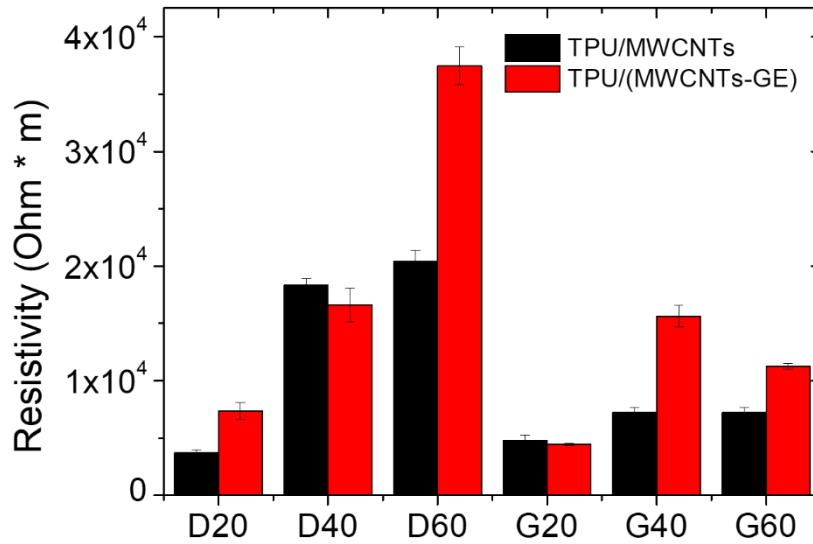


Figure 3.8. Electrical resistivity calculated by accounting for both the porosity of the systems and the electrical resistance (at 0% of strain).

The values of resistivity, which should be constant being the resistivity an intrinsic property of the materials, confirm that both the SLS printing process and geometry have a significant effect on the electrical resistance of the proposed systems. In fact, for the G samples, the resistivity is somewhat constant and does not depend on the porosity, in the range of approximations, due to the adoption of a very simple model to account for the porosity of samples. On the other side, for the systems with D geometry, the resistivity increases significantly with the porosity, confirming that the SLS printing process affects the formation of the conductive network that becomes worse and worse by increasing the porosity. This can be ascribed to the dimension of the trabeculae, which result smaller for the geometry D and give rise to a percolation network with less effective contact points between the MWCNTs and GE nanoparticles. Thus, the comparison of the electrical resistance values of systems with G geometry is robust and the variation

can be related to the porosity, whereas for the D systems, it is worth considering that the geometry and SLS printing resolution affect the electrical resistance along with the porosity.

The compression sensitivity of several porous structures was evaluated by measuring the gauge factor (GF), defined as the ratio between the relative change of the electrical resistance of the composites and their initial resistance, divided by the applied strain. All samples displayed high absolute values of GF, and, in the range of errors, no significant differences can be noticed between TPU/MWCNTs and TPU/(MWCNTs-GE) nanocomposite structures. It has to be pointed out that GF values are higher for a strain below 8%, confirming the valuable feature of the composite structures to detect small deformations. In particular, the G20 TPU/MWCNT structure showed an almost double GF value at 1% deformation, suggesting its possible use in very sensitive strain sensing devices. For all samples, GF tended to a plateau as the maximum strain value was approached, as shown in Figure 3.9. The presence of the plateau at high compression deformation is to be ascribed to the densification of the conductive pathways, which do not further change with the compression.

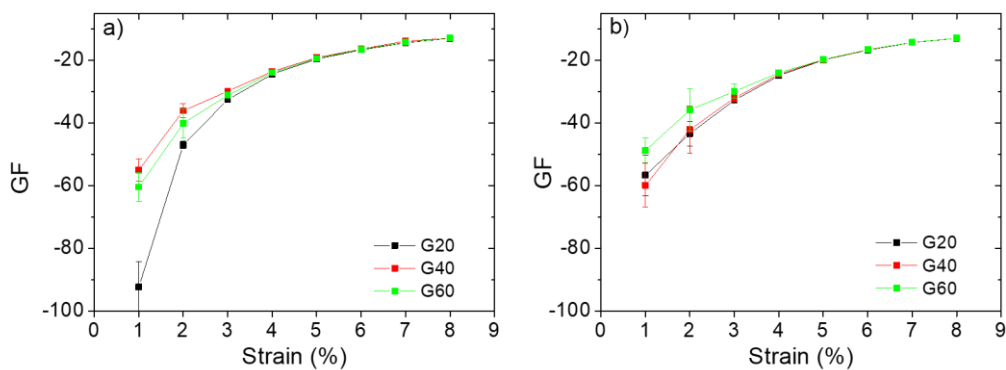


Figure 3.9. Variation of the gauge factor as a function of compression strain for TPU/MWCNTs (a) and TPU/(MWCNTs-GE) structures (b) with Gyroid unit cells.

3.3.4. EM Characterization

The broadband conductivity of investigated samples is shown in Figure 3.10. All percolated materials possess a similar frequency dependence of conductivity, consisting of two regions: the DC-like frequency-independent region is observable at lower frequencies, while at higher frequencies, the $\sigma \sim \omega^{-\alpha}$ dependence exists. For both TPU/MWCNT and TPU/(MWCNT-GE) structures, the presence of the DC-like conductivity at low frequencies is an evidence of percolation.

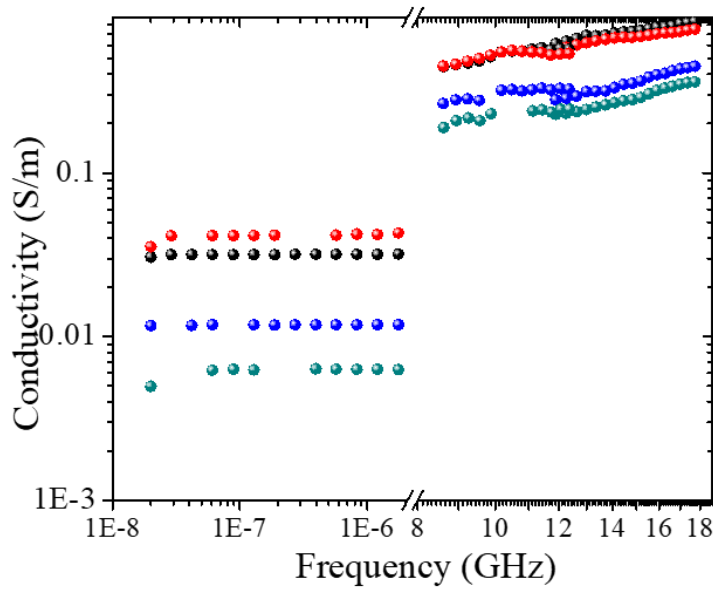


Figure 3.10. Broadband conductivity of porous structures: DC-like (0.02 kHz–1 kHz) and dielectric (12–18 GHz) conductivity behavior for TPU/MWCNTs G20 (black), TPU/MWCNTs G60 (blue), TPU/(MWCNTs-GE) G20 (red), and TPU/(MWCNTs-GE) G60 (green).

It is also possible to mention that in the DC-like range, for the systems with high porosity, the conductivity of TPU/MWCNT samples is higher than that of the systems based on TPU/MWCNT-GE, whereas only for the systems with low porosity, it seems that the GE nanoplatelets have a positive effect allowing an increment of the conductivity. The discrepancy found by comparing these results with those reported in Figure 5, may be ascribed to the fact that for broadband

conductivity measurements were used with smaller samples ($\sim 5 \times 5 \times 3 \text{ mm}^3$) as compared to those used for piezoresistive characterization. That, above all for samples with high porosity (60%), may affect the reproducibility of the results.

The electromagnetic shielding performance of the SLS-printed porous structures was evaluated for the G20 and G60 made of TPU/MWCNTs and TPU/(MWCNTs-GE) systems. The frequency dependence of real and imaginary parts of dielectric permittivity is presented in Figure 3.11.

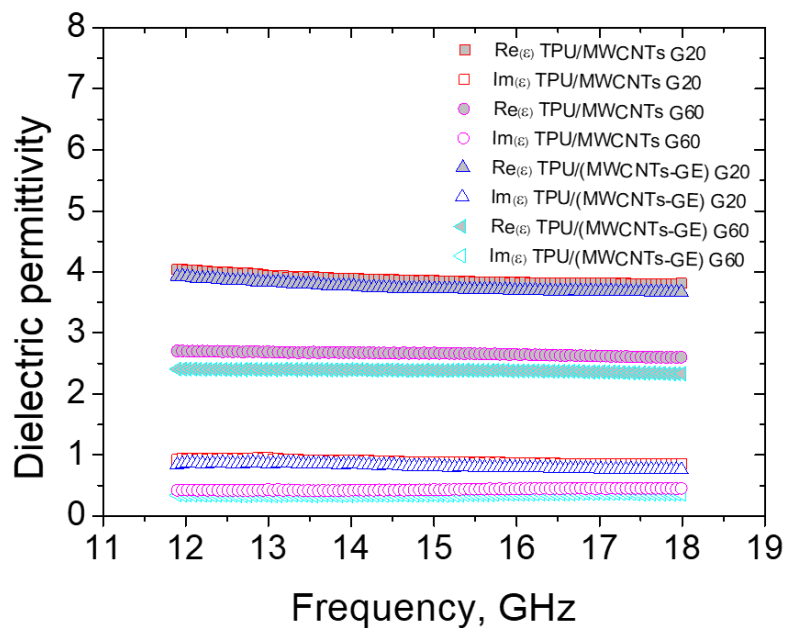


Figure 3.11. The dielectric permittivity of TPU/(MWCNTs-GE) G20 and G60 samples.

The dielectric permittivity of all samples remains almost constant within 12–18 GHz. A minor decrease of both components of dielectric permittivity (ϵ) is observed for the denser sample G20. The higher values of permittivity of sample G20 vs. G60 (dense vs. lighter) are in good correspondence with the effective medium Maxwell Garnett model for composite containing conductive particles [52].

The observed values of dielectric permittivity are suitable for the effective absorption of electromagnetic waves in both free space and the waveguide combined with the mirror (back reflector) [53]. According to Figure 3.12a, the microwave absorption coefficient within the Ku-band (12–18 GHz) is in the range of 0.51–0.99 and 0.70–0.91 for 10.6 mm thick samples of G60 and G20 series, respectively, with the peak absorption being close to 100% at 15–16 GHz.

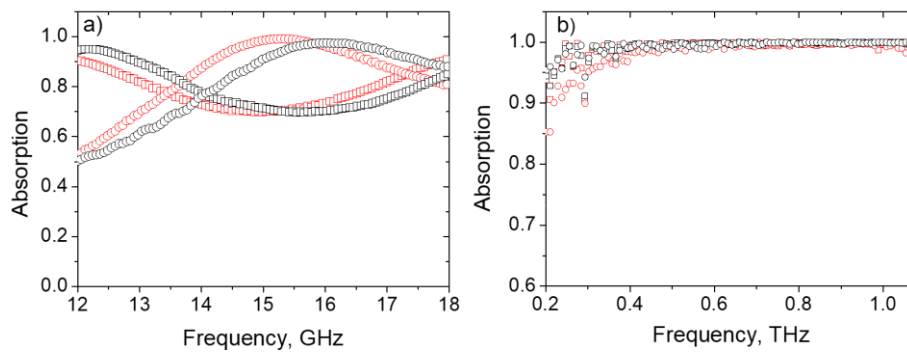


Figure 3.12. (a) Absorption coefficient of 10.6 mm thick samples with back reflector in the waveguide. (b) Absorption coefficient of 2 mm thick samples in the free space for TPU/MWCNTs G20 (red square), TPU/MWCNTs G60 (red ring), TPU/(MWCNTs-GE) G20 (black square), and TPU/(MWCNTs-GE) G60 (black ring).

The absorption coefficients of all investigated samples were calculated in the frequency range 0.2–1 THz (see Figure 3.12b) from the data collected for transmission and reflection by THz time-domain spectroscopy.

All samples (G20 and G60 series) are very lossy in the THz range and demonstrate outstanding absorption ability: the absorption coefficient of 2 mm thick samples is close to 100% starting from 300 GHz.

All investigated samples show not only extensive EMI SE, but also very high efficiency as EM waves absorbers in broad frequency range spanning from tens GHz to 1 THz. The reason is that SLS-printed samples made of TPU/MWCNTs and TPU/(MWCNTs-GE) comprise three levels of “porosity”. The inherent pores with the size coming from the lattice parameters is of 0.1 mm order (corresponding to the THz wavelength). Multiple reflection from the sides of

these pores followed by Ohmic losses of the structure skeleton are the reasons of high absorption ability of G20–G60 in the THz range.

The second level is the porosity of the systems, easily visible in the SEM images (Figure 3.2). It corresponds to 50–100 nm pores originated by defects in the sintering of wrapped TPU particles, and because of their small size are “invisible” for both investigated microwave and THz radiation, just making the overall structure slightly lighter.

To summarize, due to nested “Russian doll” porosity structure, it is possible to approach very high absorption in different frequency ranges with one sample. Moreover, this is the way of tailoring EMI SE (absorption) addressing many frequency slots, i.e., just changing the pore size by 3D printing, porosity of the structure skeleton, and geometrical features/carbonaceous filler properties of the segregated network.

3.4. Conclusions

Porous conductive 3D structures were successfully fabricated by SLS using TPU powder wrapped with MWCNTs and a mixture of MWCNTs and GE nanofillers. The samples had a porosity ranging from 20% to 60% and were realized with the Gyroid and Diamond unit cell. Mechanical, electrical, and electromagnetic properties were investigated and correlated with porosity and internal architecture of printed samples.

SEM and TEM characterization clearly indicated that SLS manufacturing is suitable to create a high pore interconnectivity. Moreover, upon processing, the nanofillers remain segregated between the particle boundaries, forming a conductive network that facilitates the electrical percolation. The presence of GE improves the thermal stability of TPU. Compression tests and electrical conductivity measurements revealed a correlation between geometrical features and elastic modulus as well as a gauge factor. In particular, G structures showed higher elastic modulus in comparison to the D architectures.

Moreover, MWCNTs-based structures displayed satisfying electrical properties, and a synergistic conductivity enhancement was observed for the TPU/(MWCNTs-GE)-based G architectures. This was ascribed to the structure of samples with G geometry, which present bigger trabeculae and thus a better percolating network as compared to the systems with D geometry. All structures showed robust piezoresistivity, with a gauge factor value of -13 at 8% strain for all systems, which remarkably varied from -70 to -20 over strain extents ranging from 1% to 5%, which is the strain range in which the composite can be used as a sensor.

Finally, a high level of EMI SE, caused by absorption of electromagnetic waves in Ku-band (12–18 GHz), was observed for G-type samples having different porosity. The waves from 300 GHz to 1 THz could not pass through 2 mm thick G20 (60) lattice due to perfect absorption. EM response peculiarities have been associated with the multi-level porosity of the samples (starting from their cellular SLS-printed structure and due to the MWCNT/GE segregated percolative network).

Highlights: The results demonstrate that mixing MWCNTs and GE minimizes the coalescence issue, which was observed in literature for GE systems.

The right balance between mechanical and functional properties of the printed structures make these systems suitable as stable piezoresistive sensors.

The systems have relevant EMI shielding properties.

References

- [1] Yan, Y.; Sencadas, V.; Zhang, J.; Zu, G.; Wei, D.; Jiang, Z. Processing, characterisation and electromechanical behaviour of elastomeric multiwall carbon nanotubes-poly (glycerol sebacate) nanocomposites for piezoresistive sensors applications. *Compos. Sci. Technol.* 2017, doi:10.1016/j.compscitech.2017.02.007.
- [2] Yaseer Omar, M.; Xiang, C.; Gupta, N.; Strbik, O.M.; Cho, K. Syntactic foam core metal matrix sandwich composite: Compressive properties and strain rate effects. *Mat. Sci. Eng. A* 2015, doi:10.1016/j.msea.2015.07.033.
- [3] Mahendia, S.; Tomar, A.K.; Kumar, S. Electrical conductivity and dielectric spectroscopic studies of PVA-Ag nanocomposite films. *J. Alloys Compd.* 2010, doi:10.1016/j.jallcom.2010.08.075.
- [4] Hansen, T.S.; West, K.; Hassager, O.; Larsen, N.B. Highly stretchable and conductive polymer material made from poly(3,4-ethylenedioxythiophene) and polyurethane elastomers. *Adv. Funct. Mat.* 2007, doi:10.1002/adfm.200601243.
- [5] Liu, H.; Dong, M.; Huang, W.; Gao, J.; Dai, K.; Guo, J.; Zheng, G.; Liu, C.; Shen, C.; Guo, Z. Lightweight conductive graphene/thermoplastic polyurethane foams with ultrahigh compressibility for piezoresistive sensing. *J. Mat. Chem. C* 2017, 5, 73–83.
- [6] Wang, L.; Ding, T.; Wang, P. Thin flexible pressure sensor array based on carbon black/silicone rubber nanocomposite. *IEEE Sens. J.* 2009, 9, 1130–1135.

- [7] Tao, J.; Liu, N.; Ma, W.; Ding, L.; Li, L.; Su, J.; Gao, Y. Solid-state high performance flexible supercapacitors based on polypyrrole-MnO₂-carbon fiber hybrid structure. *Sci. Rep.* 2013, 3, 2286–2293.
- [8] Guan, X.; Zheng, G.; Dai, K.; Liu, C.; Yan, X.; Shen, C.; Guo, Z. Carbon nanotubes-adsorbed electrospun PA66 nanofiber bundles with improved conductivity and robust flexibility. *ACS Appl. Mat. Interfaces* 2016, 8, 14150–14159.
- [9] Gupta, P.; Yadav, S.K.; Agrawal, B.; Goyal, R.N. A novel graphene and conductive polymer modified pyrolytic graphite sensor for determination of propranolol in biological fluids. *Sens. Actuators B Chem.* 2014, 204, 791–798.
- [10] Bai, J.; Zhou, A.; Huang, Z.; Wu, J.; Bai, H.; Li, L. Ultra-light and elastic graphene foams with a hierarchical structure and a high oil absorption capacity. *J. Mat. Chem. A* 2015, 3, 22687–22694.
- [11] Liu, H.; Gao, J.; Huang, W.; Dai, K.; Zheng, G.; Liu, C.; Shen, C.; Yan, X.; Guo, J.; Guo, Z. Electrically conductive strain sensing polyurethane nanocomposites with synergistic carbon nanotubes and graphene bifillers. *Nanoscale* 2016, 8, 12977–12989.
- [12] Zhang, D.; Chi, B.; Li, B.; Gao, Z.; Du, Y.; Guo, J.; Wei, J. Fabrication of highly conductive graphene flexible circuits by 3D printing. *Synth. Met.* 2016, 217, 79–86.
- [13] Wang, H.; Xie, G.; Fang, M.; Ying, Z.; Tong, Y.; Zeng, Y. Electrical and mechanical properties of antistatic PVC films containing multi-layer graphene. *Compos. Part. B Eng.* 2015, 79, 444–450.

- [14] Chen, Z.; Xu, C.; Ma, C.; Ren, W.; Cheng, H. Lightweight and flexible graphene foam composites for high-performance electromagnetic interference shielding. *Adv. Mat.* 2013, 25, 1296–1300.
- [15] Tang, D.; Ma, G.; Zhang, L.; Chen, G. Graphene-epoxy composite electrode fabricated by in situ polycondensation for enhanced amperometric detection in capillary electrophoresis. *J. Chromatogr. A* 2013, 1316, 127–134.
- [16] Zhan, Y.; Lavorgna, M.; Buonocore, G.; Xia, H. Enhancing electrical conductivity of rubber composites by constructing interconnected network of self-assembled graphene with latex mixing. *J. Mat. Chem.* 2012, 22, 10464–10468.
- [17] Bose, S.; Bhattacharyya, A.R.; Kulkarni, A.R.; Pötschke, P. Electrical, rheological and morphological studies in co-continuous blends of polyamide 6 and acrylonitrile–butadiene–styrene with multiwall carbon nanotubes prepared by melt blending. *Compos. Sci. Technol.* 2009, 69, 365–372.
- [18] Araby, S.; Meng, Q.; Zhang, L.; Kang, H.; Majewski, P.; Tang, Y.; Ma, J. Electrically and thermally conductive elastomer/graphene nanocomposites by solution mixing. *Polymer* 2014, 55, 201–210.
- [19] Manapat, J.Z.; Chen, Q.; Ye, P.; Advincula, R.C. 3D printing of polymer nanocomposites via stereolithography. *Macromol. Mat. Eng.* 2017, 302, 1600553.
- [20] Chen, Q.; Mangadlao, J.D.; Wallat, J.; De Leon, A.; Pokorski, J.K.; Advincula, R.C. 3D printing biocompatible polyurethane/poly (lactic acid)/graphene oxide nanocomposites: Anisotropic properties. *ACS Appl. Mat. Interfaces* 2017, 9, 4015–4023.

- [21] Lee, J.-Y.; An, J.; Chua, C.K. Fundamentals and applications of 3D printing for novel materials. *Appl. Mat. Today* 2017, 7, 120–133.
- [22] Paggi, R.A.; Beal, V.E.; Salmoria, G. V Process optimization for PA12/MWCNT nanocomposite manufacturing by selective laser sintering. *Int. J. Adv. Manuf. Technol.* 2013, 66, 1977–1985.
- [23] Shuai, C.; Gao, C.; Feng, P.; Peng, S. Graphene-reinforced mechanical properties of calcium silicate scaffolds by laser sintering. *RSC Adv.* 2014, 4, 12782–12788.
- [24] Li, Z.; Wang, Z.; Gan, X.; Fu, D.; Fei, G.; Xia, H. Selective laser sintering 3D printing: A way to construct 3d electrically conductive segregated network in polymer matrix. *Macromol. Mat. Eng.* 2017, 302, 1700211.
- [25] Yuan, S.; Shen, F.; Bai, J.; Chua, C.K.; Wei, J.; Zhou, K. 3D soft auxetic lattice structures fabricated by selective laser sintering: TPU powder evaluation and process optimization. *Mat. Des.* 2017, 120, 317–327.
- [26] Robertson, J.M.; Torbati, A.H.; Rodriguez, E.D.; Mao, Y.; Baker, R.M.; Qi, H.J.; Mather, P.T. Mechanically programmed shape change in laminated elastomeric composites. *Soft Matter* 2015, 11, 5754–5764.
- [27] Ronca, A.; Rollo, G.; Cerruti, P.; Fei, G.; Gan, X.; Buonocore, G.G.; Lavorgna, M.; Xia, H.; Silvestre, C.; Ambrosio, L. Selective laser sintering fabricated thermoplastic polyurethane/graphene cellular structures with tailorable properties and high strain sensitivity. *Appl. Sci.* 2019, 9, doi:10.3390/app9050864.
- [28] Liu, H.; Li, Y.; Dai, K.; Zheng, G.; Liu, C.; Shen, C.; Yan, X.; Guo, J.; Guo, Z. Electrically conductive thermoplastic elastomer nanocomposites at

- ultralow graphene loading levels for strain sensor applications. *J. Mat. Chem. C* 2016, 4, 157–166.
- [29] Geetha, S.; Satheesh Kumar, K.K.; Rao, C.R.K.; Vijayan, M.; Trivedi, D.C. EMI shielding: Methods and materials—A review. *J. Appl. Polym. Sci.* 2009, 112, 2073–2086.
- [30] Pang, H.; Xu, L.; Yan, D.-X.; Li, Z.-M. Conductive polymer composites with segregated structures. *Prog. Polym. Sci.* 2014, 39, 1908–1933.
- [31] Gan, X.; Wang, J.; Wang, Z.; Zheng, Z.; Lavorgna, M.; Ronca, A.; Fei, G.; Xia, H. Simultaneous realization of conductive segregation network microstructure and minimal surface porous macrostructure by SLS 3D printing. *Mat. Des.* 2019, 178, doi:10.1016/j.matdes.2019.107874.
- [32] Zhan, Y.; Oliviero, M.; Wang, J.; Sorrentino, A.; Buonocore, G.G.; Sorrentino, L.; Lavorgna, M.; Xia, H.; Iannace, S. Enhancing the EMI shielding of natural rubber-based supercritical CO₂ foams by exploiting their porous morphology and CNT segregated networks. *Nanoscale* 2019, 11, 1011–1020.
- [33] Tasolamprou, A.C.; Koulouklidis, A.D.; Daskalaki, C.; Mavidis, C.P.; Kenanakis, G.; Deligeorgis, G.; Viskadourakis, Z.; Kuzhir, P.; Tzortzakis, S.; Kafesaki, M. Experimental demonstration of ultrafast THz modulation in a graphene-based thin film absorber through negative photoinduced conductivity. *ACS Photonics* 2019, 6, 720–727.
- [34] Paddubskaya, A.; Demidenko, M.; Batrakov, K.; Valušis, G.; Kaplas, T.; Svirko, Y.; Kuzhir, P. Tunable perfect THz absorber based on a stretchable ultrathin carbon-polymer bilayer. *Materials* 2019, 12, 143.

- [35] Kuzhir, P.P.; Paddubskaya, A.G.; Volynets, N.I.; Batrakov, K.G.; Kaplas, T.; Lamberti, P.; Kotsilkova, R.; Lambin, P. Main principles of passive devices based on graphene and carbon films in microwave—THz frequency range. *J. Nanophotonics* 2017, 11, 32504.
- [36] Batrakov, K.; Kuzhir, P.; Maksimenko, S.; Volynets, N.; Voronovich, S.; Paddubskaya, A.; Valusis, G.; Kaplas, T.; Svirko, Y.; Lambin, P. Enhanced microwave-to-terahertz absorption in graphene. *Appl. Phys. Lett.* 2016, doi:10.1063/1.4944531.
- [37] Letellier, M.; Macutkevicius, J.; Kuzhir, P.; Banys, J.; Fierro, V.; Celzard, A. Electromagnetic properties of model vitreous carbon foams. *Carbon* N. Y. 2017, 122, 217–227.
- [38] Kotsilkova, R.; Ivanov, E.; Bychanok, D.; Paddubskaya, A.; Demidenko, M.; Macutkevicius, J.; Maksimenko, S.; Kuzhir, P. Effects of sonochemical modification of carbon nanotubes on electrical and electromagnetic shielding properties of epoxy composites. *Compos. Sci. Technol.* 2015, 106, 85–92.
- [39] Kuzhir, P.; Paddubskaya, A.; Bychanok, D.; Nemilentsau, A.; Shuba, M.; Plusch, A.; Maksimenko, S.; Bellucci, S.; Coderoni, L.; Micciulla, F. Microwave probing of nanocarbon based epoxy resin composite films: Toward electromagnetic shielding. *Thin Solid Films* 2011, 519, 4114–4118.
- [40] ASTM. D5568-95 Standard Test Method for Measuring Relative Complex Permittivity and Relative Magnetic Permeability of Solid Materials at Microwave Frequencies; ASTM International: West Conshohocken, PA, USA.

- [41] Paddubskaya, A.; Valynets, N.; Kuzhir, P.; Batrakov, K.; Maksimenko, S.; Kotsilkova, R.; Velichkova, H.; Petrova, I.; Biró, I.; Kertész, K. Electromagnetic and thermal properties of three-dimensional printed multilayered nano-carbon/poly (lactic) acid structures. *J. Appl. Phys.* 2016, 119, 135102.
- [42] Liu, H.; Huang, W.; Yang, X.; Dai, K.; Zheng, G.; Liu, C.; Shen, C.; Yan, X.; Guo, J.; Guo, Z. Organic vapor sensing behaviors of conductive thermoplastic polyurethane–graphene nanocomposites. *J. Mat. Chem. C* 2016, 4, 4459–4469.
- [43] Wang, X.; Hu, Y.; Song, L.; Yang, H.; Xing, W.; Lu, H. In situ polymerization of graphene nanosheets and polyurethane with enhanced mechanical and thermal properties. *J. Mat. Chem.* 2011, 21, 4222–4227.
- [44] Xie, S.H.; Liu, Y.Y.; Li, J.Y. Comparison of the effective conductivity between composites reinforced by graphene nanosheets and carbon nanotubes. *Appl. Phys. Lett.* 2008, 92, 243121.
- [45] Du, J.; Zhao, L.; Zeng, Y.; Zhang, L.; Li, F.; Liu, P.; Liu, C. Comparison of electrical properties between multi-walled carbon nanotube and graphene nanosheet/high density polyethylene composites with a segregated network structure. *Carbon N. Y.* 2011, 49, 1094–1100.
- [46] Hodlur, R.M.; Rabinal, M.K. Self assembled graphene layers on polyurethane foam as a highly pressure sensitive conducting composite. *Compos. Sci. Technol.* 2014, 90, 160–165.
- [47] Kang, J.H.; Park, C.; Scholl, J.A.; Brazin, A.H.; Holloway, N.M.; High, J.W.; Lowther, S.E.; Harrison, J.S. Piezoresistive characteristics of single wall carbon nanotube/polyimide nanocomposites. *J. Polym. Sci. Part B Polym. Phys.* 2009, 47, 994–1003.

- [48] Ku-Herrera, J.J.; Avilés, F. Cyclic tension and compression piezoresistivity of carbon nanotube/vinyl ester composites in the elastic and plastic regimes. *Carbon N. Y.* 2012, 50, 2592–2598.
- [49] Lipomi, D.J.; Vosgueritchian, M.; Tee, B.C.K.; Hellstrom, S.L.; Lee, J.A.; Fox, C.H.; Bao, Z. Skin-like pressure and strain sensors based on transparent elastic films of carbon nanotubes. *Nat. Nanotechnol.* 2011, 6, 788–792.
- [50] Kumar, S.K.; Castro, M.; Saiter, A.; Delbreilh, L.; Feller, J.F.; Thomas, S.; Grohens, Y. Development of poly (isobutylene-co-isoprene)/reduced graphene oxide nanocomposites for barrier, dielectric and sensing applications. *Mat. Lett.* 2013, 96, 109–112.
- [51] Montes, J.M.; Cuevas, F.G.; Cintas, J.; Ternero, F.; Caballero, E.S. Electrical resistivity of powdered porous compacts. In *Electrical and Electronic Properties of Materials*; IntechOpen: London, UK, 2018.
- [52] Bychanok, D.; Angelova, P.; Paddubskaya, A.; Meisak, D.; Shashkova, L.; Demidenko, M.; Plyushch, A.; Ivanov, E.; Krastev, R.; Kotsilkova, R. Terahertz absorption in graphite nanoplatelets/polylactic acid composites. *J. Phys. D. Appl. Phys.* 2018, 51, 145307.
- [53] Bychanok, D.; Gorokhov, G.; Meisak, D.; Kuzhir, P.; Maksimenko, S.A.; Wang, Y.; Han, Z.; Gao, X.; Yue, H. Design of carbon nanotube-based broadband radar absorber for ka-band frequency range. *Prog. Electromagn. Res.* 2017, 53, 9–16.

Conclusions and future perspectives

Electrically conductive porous structures were successfully fabricated by SLS using TPU powder wrapped with GE, MWCNTs and a mixture of MWCNTs and GE nanofillers, in order to realize a tailored segregated distribution of the filler in the printed volume. The architectures were designed by using single unit cells such as Gyroid, Diamond and Schwarz, and a porosity ranging from 20 to 80%. Mechanical properties, electromagnetic shielding, electrical and thermal conductivity were exhaustively measured for all systems, and the results were discussed correlating unit cells of porous structures, porosity, filler typology and contents.

In summary, SLS manufacturing is suitable to create a high pore interconnectivity as clearly indicated by SEM and TEM morphological characterization, which confirmed the presence of a double porosity, in the micron-scale length (presence of pores of hundreds microns) and sub-micron scale length (presence of pores between the sintered TPU particles). Moreover, upon sintering the GE nanoparticle and MWCNTs remain entrapped in between the interparticle boundaries, thereby forming the expected segregated conductive network which percolates the porous structure. The results show that GE reduced the mobility of the polymer soft segments, increasing the T_g and hindered crystallization of TPU hard segments with a consequent improvement of thermal stability of TPU composites. On the other side, for the composite with MWCNTs it is not possible to detect any significant effect on the thermal properties. The mixed system TPU/(MWCNTs GE) shows a two-step degradation curve, different from that of pristine TPU. These results confirm that the 2D filler is more effective in protecting the polymer from gases diffusion during high temperature treatments, contributing to improve the stability of the resulting composite materials.

The mechanical characterization revealed that as for TPU/GE systems is concerned, the S geometry provides the porous structure with higher elastic

modulus. In general, for all the systems, G structures showed higher elastic modulus in comparison to the D architectures.

As for the electrical properties, the TPU/(MWCNTs-GE)-based G architectures showed a synergistic conductivity enhancement. The reason can be found in the structure of samples with G geometry, which present bigger trabeculae and thus a better percolating network as compared to the systems with D geometry.

G and D structures showed robust piezoresistivity, with a gauge factor value which remarkably varied from -70 to -20 over strain extents ranging from 1% to 5%, which is the strain range in which the composites can be used as a sensor. S geometry structures for TPU/GE system yielded GF values of -12.4 at 8% strain, due to the combination of GE network segregation and higher size of trabeculae connecting the porosity.

Upon cyclic piezoresistive sensing tests, all samples exhibited excellent stability, regardless of their porosity and geometry. Electro-magnetic shielding response have been associated with the multi-level porosity of the samples. In particular, EMI SE, caused by absorption of electromagnetic waves in Ku-band (12–18 GHz), was observed for G-type samples having different porosity. The waves from 300 GHz to 1 THz could not pass through 2 mm thick G20 (60) lattice due to perfect absorption.

In conclusion, the reported results demonstrate that TPU/MWCNTs-GE powder is a suitable material for the SLS fabrication of porous structures with highly tailored flexibility and electrical conductivity, which can be effectively used for the production of pressure sensors. Their applicability was demonstrated by placing our best piezoresistive materials (the TPU / MWCNTs-GE system) on a person's forearm (Figure 4.1) to monitor the muscle activation following hand movements. Initially the hand was open (Figure 4.1a), the piezoresistive composite was not compressed and the zero point signal can be seen in Figure 4.1c (indicated by red arrow).

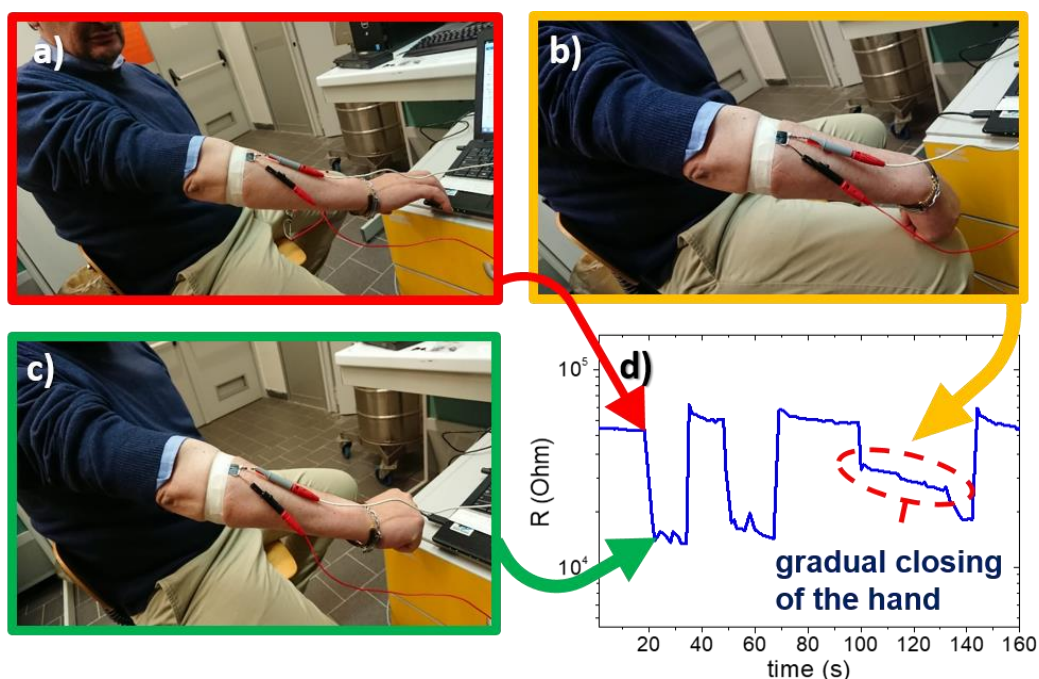


Figure 4.1. Experimental moments: a) open hand, b) gradual closing hand, c) close hand, d) graphical response of electrical measurement.

Gradually the hand was closed (Figure 4.1b), and the signal of the electrical resistance decreased slowly, as indicated by the yellow arrow. Finally, when the hand was firmly closed (Figure 4.1c), the electrical signal remained stable around the values corresponding to the maximum compression for the experimental system (Figure 4.1d, green arrow indication). This simple example experiment aims to demonstrate that the porous structures are sensitive to small variations in compression and can be used with the appropriate optimizations in applications such as biomedicine, prosthetics, biomechanics, etc.

Based on these results, a very interesting perspective of this work is to explore the potentials of other 2D materials, among the 2D graphene related materials such as the MXenes. At the same time, it would be very interesting to consider metal nanowires, such as silver nanowires, which represent an effective substitute of carbon nanotubes in the development of several multifunctional materials. Finally it would be intriguing to explore the potentials of hybrid

systems realized by mixing over a wide range of compositions, both innovative 2D and 2D fillers, in the preparation of raw elastomeric powders for SLS additive technology. It is guessed that these materials coupled with innovative technology can allow the design and preparation of new multifunctional systems, able to exhibit both structural and functional (electrical, thermal, piezoresistive, electromagnetic shielding) properties, fulfilling the more and more increasing demand of materials with outstanding properties.

Papers, conference contributions, participations to formation and dissemination events, and research periods abroad

Papers

Rollo, G., Ronca, A., Cerruti, P., Gan, X. P., Fei, G., Xia, H., ... & Ambrosio, L. (2020). On the Synergistic Effect of Multi-Walled Carbon Nanotubes and Graphene Nanoplatelets to Enhance the Functional Properties of SLS 3D-Printed Elastomeric Structures. *Polymers*, 12(8), 1841.

Ronca, A., Rollo, G., Cerruti, P., Fei, G., Gan, X., Buonocore, G. G., ... & Ambrosio, L. (2019). Selective laser sintering fabricated thermoplastic polyurethane/graphene cellular structures with tailorable properties and high strain sensitivity. *Applied Sciences*, 9(5), 864.

Piscitelli, F., Rollo, G., Scherillo, F., Lavorgna, M. (2019). Innovative Graphene-PDMS sensors for aerospace applications, *Advanced Materials Letters*, 10(8), 533.

Oral communications

Ronca, A., Rollo, G., Cerruti, P., Fei, G., Gan, X., Buonocore, G. G., Lavorgna, M., Xia, H., Silvestre, C. and Ambrosio, L. High strain sensitivity systems of thermoplastic polyurethane/graphene fabricated with selective laser sintering, 3-5 October 2019, Graphene 3D Project, Capri, Italy.

Ronca, A., Rollo, G., Cerruti, P., Fei, G., Gan, X., Buonocore, G. G., Xia, H., Silvestre, C. Ambrosio, L. and Lavorgna, M. Selective Laser Sintering Fabricated Thermoplastic Polyurethane/Graphene Cellular Structures with Tailorable Properties and High Strain Sensitivity, 28-30 August 2019, CIS2019, Salerno, Italy.

Poster communications

Rollo, G., Ronca, A., Cerruti, P., Ambrosio, L., and Marino Lavorgna, Effect of carbon nanotubes and graphene nanoplatelets on properties of elastomer-based 3D printed porous structures, 14-16 December 2020, Workshop IPCB, Naples, Italy.

Ronca, A., Rollo, G., Cerruti, P., Fei, G., Gan, X., Buonocore, G. G., Lavorgna, M., Xia, H., Silvestre, C. and Ambrosio, L. Selective laser sintering fabricated thermoplastic polyurethane graphene cellular structures for pressure sensor applications, 14-17 October 2019, PolyChar27, Naples, Italy

Piscitelli, F., Lavorgna, M., Rollo, G., Scherillo, F., Volponi, R., Ameduri, S., Concilio, A., Ciminello, M., Sprayable Piezoresistive Sensors for Aerospace Applications, Graphene Week 2018, 10-14 September 2018, San Sebastian, Spain.

Formation and dissemination Events

Lavorgna, M., Buonocore, G. G., Di Mario, R., Gentile, G., Rollo, G., Ronca, A., Salzano de Luna, M., Santillo, C., Verdolotti, L., Xia, H., and Ambrosio, L. Advanced polymer nanocomposites by tailoring the graphene and its derivatives' spatial morphology, 16 December 2019, 50th Anniversary of IPCB, Naples, Italy.

Winner of the event "Progetto Bandiera: La Fabbrica del Futuro", Prelude-Modular multi sensor system for the identification of complex end of life products in circular economy factories, 26-30 November 2018, Rome, Italy.

Research stay abroad

Visiting scientist at Mackenzie Presbyterian University, From 16 June to 18 August 2019, São Paulo, Brazil.

Acknowledgements: This research was supported by Marie Skłodowska-Curie Actions (MSCA) Research and Innovation Staff Exchange (RISE) H2020-MSCA-RISE-2016, Project Acronym: Graphene 3D—Grant Number: 734164. Thanks are due to Dr. Alfredo Ronca for the preparation of porous structures, CAD files and printing of the structures. Thanks to Prof. Hesheng Xia and his group of Sichuan University for the preparation of TPU powders wrapped with the several carbonaceous fillers, Prof. Polina Khuzir and her group for EMI SE characterizations, Dr. Clara Silvestre the opportunity to participate in the project Graphene 3D as young researcher, and finally to Prof. Ricardo Andrade for the hospitality at the Makenzie University during the project secondment in São Paulo, Brazil.